2011

Electronic Transport Properties of Ruthenium and Ruthenium Dioxide Thin Films

Michael M. Steeves

Recommended Citation

Steeves, Michael M., "Electronic Transport Properties of Ruthenium and Ruthenium Dioxide Thin Films" (2011). *Electronic Theses and Dissertations*. 262.
http://digitalcommons.library.umaine.edu/etd/262

ELECTRONIC TRANSPORT PROPERTIES OF RUTHENIUM AND RUTHENIUM DIOXIDE THIN FILMS

By

Michael M. Steeves

B.S. University of Maine, 1971

M.S. Massachusetts Institute of Technology, 1973

A THESIS

Submitted in Partial Fulfillment of the
Requirements for the Degree of
Doctor of Philosophy
(in Physics)

The Graduate School
The University of Maine
May, 2011

Advisory Committee:

Robert J. Lad, Professor of Physics, Advisor

Susan R. McKay, Professor of Physics

William J. DeSisto, Associate Professor of Chemical Engineering

David J. Frankel, Senior Research Scientist, LASST

George P. Bernhardt, Research Scientist, LASST

DISSERTATION

ACCEPTANCE STATEMENT

On behalf of the Graduate Committee for Michael M. Steeves, I affirm that this manuscript is the final accepted dissertation. Signatures of all committee members are on file with the Graduate School at the University of Maine, 5755 Stodder Hall, Orono, Maine 04469.

Dr. Robert J. Lad, Professor of Physics, Department of Physics and Astronomy (date)

LIBRARY RIGHTS STATEMENT

In presenting this thesis in partial fulfillment of the requirements for an advanced degree at The University of Maine, I agree that the Library shall make it freely available for inspection. I further agree that permission for "fair use" copying of this thesis for scholarly purposes may be granted by the Librarian. It is understood that any copying or publication of this thesis for financial gain shall not be allowed without my written permission.

Signature:

Date:

ELECTRONIC TRANSPORT PROPERTIES OF RUTHENIUM AND RUTHENIUM DIOXIDE THIN FILMS

By Michael M. Steeves

Thesis Advisor: Dr. Robert J. Lad

An Abstract of the Thesis Presented
in Partial Fulfillment of the Requirements for the
Degree of Doctor of Philosophy
(in Physics)
May 2011

Resistivities (ρ) and Hall coefficients (R_H) of polycrystalline Ru and RuO_2 thin films were measured from 293 to 600 K in vacuum, O_2, and CO. Differing nanostructures and textures were sputtered at normal, confocal, and glancing incidences to 20 - 300 nm thickness. For Ru in planar or nanorod morphologies, defects have negligible effect on R_H, which is similar to R_H in bulk metal. Models of effective thickness are derived for the nanorod morphology. For Ru and RuO_2 films, decreases in ρ on first heating are caused by defect annealing; subsequent heating shows metallic behavior. Changes from n-type to p-type conduction in RuO_2 are correlated to grain structures and film strains. For certain RuO_2 films, oxygen loss in high vacuum is demonstrated and a R_H phase diagram is constructed to reflect the switch in dominant carriers from electrons to holes. Exposure of some RuO_2 films to pure CO is shown to cause an irreversible increase in ρ. Resistivity hysteresis loops after multiple heat cycles with switching from O_2 to CO are posited to be consistent with catalysis on Ru rather than RuO_2 surfaces. It is shown that switching the gas environment from O_2 to CO can change dominant carriers. The physical instability, breakup, and reduction of RuO_2 films to Ru metal upon CO exposure is demonstrated.

DEDICATION

To my father, Merle Vincent Steeves, 1920 - 2009.

He was a good man.

ACKNOWLEDGMENTS

First of all, I would like to thank my thesis advisor Professor Robert J. Lad for his guidance, patience, and kindness during our weekly one-on-one meetings. I learned a lot and felt relaxed enough to ask questions and make mistakes. I would also like to thank all of my committee members for their help, advice, and insights. Next, I would like to thank Professor Victor E. Henrich of Yale University for being willing to undertake the arduous task of external reader. I also want to thank Dr. Derya Deniz for the pleasure of collaborating with him on transport measurements of nanorod films during his post doctoral research at LASST. Dr. Jason Gu from Carnegie Mellon University also deserves mention for his collaboration in thin-film transport measurements. For technical assistance and guidance in the lab, I would like to thank Dr. George Bernhardt, Dr. David Frankel, Mr. Michael Call, Mr. Eric Martin, and Dr. Scott Moulzolf, who filled the role of human encyclopedias and founts of wisdom. I would also like to thank Mr. Peter Buchanan for teaching me clean room techniques and collaborating on the growth of my first thin films. As fellow students who helped in the lab, I would like to thank Luke Doucette, John Krassikoff, Darren Southworth, Tyler Dunn, Daesha More, Xuefei Zhang, and Mark Byrne. Finally, I would like to thank Mrs. Patty Paul and Mrs. Susan Ashley for their considerable help with the finer points of lab administrative protocol.

TABLE OF CONTENTS

CHAPTER

LIST OF TABLES

LIST OF FIGURES

LIST OF SYMBOLS

Note: some symbols (for example, those with subscript permutations) are not defined because their meaning is clear from similar definitions and from the context in which they are written. SI units are given.

ROMAN

Symbol	**(Units)**	**Definition**
a	(m)	unit cell spacing
a, b, c	(m)	crystal axes
B_z	(T)	magnetic field component in the z-direction
d	(m)	average distance between grain boundaries
D_d	(m^2/s)	diffusion coefficient for dislocation pipeline
D_{gb}	(m^2/s)	diffusion coefficient for grain boundary
D_s	(m^2/s)	diffusion coefficient for free surface
e	(C)	electron charge
E	(J)	energy
$\boldsymbol{E}$	(V/m)	electric field vector
$E_{bulk}^{expanded}$	(J)	energy per atom of expanded rutile structure without oxygen
E_{bulk}^{pure}	(J)	energy per atom of pure bulk metal crystal
E_H	(V/m)	Hall electric field
$\boldsymbol{E}_L$	(V/m)	Lorentz electric field vector
$E_{\boldsymbol{x}}$	(V/m)	electric field component in the x-direction
E_y	(V/m)	electric field component in the y-direction
f	(---)	geometry factor (function of Q in the van der Pauw method)
$\boldsymbol{f}$	(N)	Lorentz force vector on single charge carrier

f_A, f_B	(---)	geometry factors for resistivity measurement correction in ASTM F76 - 86
f_{gb}	(---)	grain boundary factor
f_{fs}	(---)	free surface factor
f_r	(---)	roughness factor
$\boldsymbol{F}$	(N/m^3)	Lorentz force density vector
G(θ_R/T)	(---)	Gruneisen-Bloch function
G_{deform}	(J)	Gibbs free energy of deformation
ΔG_f^o	(J)	Gibbs free energy of formation
h	(m)	grain height; thickness of single-crystal film
I	(A)	electric current
I_A	(A)	electric current in slab A
I_B	(A)	electric current in slab B
I_x	(A)	electric current in the x-direction
$\boldsymbol{J}$	(A/m^2)	electric current density vector
J_x	(A/m^2)	electric current density in the x-direction
l_o	(m)	electron mean free path
l_1	(m)	nanorod thickness
l_2	(m)	nanorod spacing
L	(m)	slab length
L_A	(m)	slab A length in y-direction
L_B	(m)	slab B length in y-direction
m	(kg)	effective mass of charge carrier
m	(---)	number of atoms in unit cell
m_h	(kg)	effective mass of hole

m_e	(kg)	effective mass of electron
n	(m^{-3})	charge concentration
n	(---)	bonding exponent
n_e	(m^{-3})	charge concentration in electron band
n_h	(m^{-3})	charge concentration in hole band
n_{RK}	(---)	Rossnagel-Kuan factor
N	(m^2/K s)	Nernst coefficient
p	(w/m^3)	power density
p	(Pa)	dissociation pressure
p	(---)	specular scattering coefficient
P	(K m^3/J)	Ettingshausen coefficient
p_{CO}	(---)	specular scattering coefficient for carbon monoxide
p_{CO_2}	(---)	specular scattering coefficient for carbon dioxide
p_{O_2}	(---)	specular scattering coefficient for oxygen
p_{O_2}	(Pa)	oxygen pressure
q	(C)	generic electric charge
Q, Q_A, Q_B	(---)	quality factor; resistance or voltage ratio per ASTM F76 - 86
r	(m)	root-mean-square roughness of surface
R	(J/mol K)	ideal gas constant
R	(m)	distance between atoms
R	(---)	surface reflection coefficient
$R_{AB,CD}$	(Ω)	electrical resistance (see eqn. 2.44)
R_{CO}	(---)	surface reflection coefficient for carbon monoxide
R_{CO_2}	(---)	surface reflection coefficient for carbon dioxide
R_h	(m)	position of zero pair-potential energy

R_H	(m^3/C)	Hall coefficient
R_{Ha}	(m^3/C)	adiabatic Hall coefficient
R_{HA}	(m^3/C)	Hall coefficient of slab A
R_{HB}	(m^3/C)	Hall coefficient of slab B
R_{HC}	(m^3/C)	Hall coefficient of slab C
R_{HC}, R_{HD}	(m^3/C)	Hall coefficients per ASTM F76 - 86
R_{Hi}	(m^3/C)	isothermal Hall coefficient
R_{O_2}	(---)	surface reflection coefficient for oxygen
R_{total}	(Ω)	total resistance of nanorod film
$R_{12,34}$	(Ω)	resistance defined as $(V_{12,34}/I)$
S	(V/K)	thermoelectric power
t	(m)	slab thickness
T	(K)	temperature
T_m	(K)	melting temperature
t_A	(m)	thickness of slab A
t_B	(m)	thickness of slab B
t_{1n}	(m)	effective thickness of nanorod film
t_1	(m)	thickness of nanorod (from substrate to tip)
t_2	(m)	thickness of nanorod base layer
U	(J)	effective pair-potential energy
U_{bond}	(J)	bonding pair-potential energy
U_{rep}	(J)	repulsive pair-potential energy
ΔU	(J)	energy difference between competing structures
$\boldsymbol{v}$	(m/s)	charge velocity
V	(V)	electrical potential (voltage)

V	(J)	pair-potential energy
V_{BLf}	(V)	final baseline voltage measured after current is turned off
V_{BLi}	(V)	initial baseline voltage measured before current is turned on
V_c	(V)	corrected voltage signal (after baseline subtraction)
V_{tol}	(V)	voltage drift tolerance (amount of drift in a specified interval)
V_y	(V)	potential (voltage) in the y-direction
$V_{12,34}$	(V)	potential difference defined in ASTM F76 - 86: $V_3 - V_4$ when current enters pin 1 and exits pin 2
w	(m)	slab width
w_A	(m)	width of slab A in direction of current flow
w_B	(m)	width of slab B in direction of current flow
Z_{rep}	(---)	effective coordination number for repulsive term
Z_{bond}	(---)	effective coordination number for bonding term

GREEK

α	(---)	scattering parameter
θ_R	(K)	resistivity characteristic temperature
θ_{Ra}	(K)	resistivity characteristic temperature a-direction
θ_{Rc}	(K)	resistivity characteristic temperature c-direction
κ	(---)	ratio of grain boundary height to electron mean free path
κ_{GB}	(Ω m K)	Gruneisen-Bloch constant related to electron-phonon interaction
λ	(---)	hardness of potential
μ	(m^2/V s)	charge mobility
μ_e, μ_h	(m^2/V s)	electron mobility, hole mobility
ξ	(J)	electron chemical potential

ρ	(Ω m)	electrical resistivity
$\bar{\rho}$	(Ω m)	average electrical resistivity
ρ_a	(Ω m)	resistivity perpendicular to c-axis of Ru single crystal
ρ_c	(Ω m)	resistivity parallel to c-axis of Ru single crystal
ρ_A	(Ω m)	resistivity defined in ASTM F 76 - 86
ρ_B	(Ω m)	resistivity defined in ASTM F 76 - 86
ρ_o	(Ω m)	temperature-independent electrical resistivity
ρ_i	(Ω m)	temperature-dependent electrical resistivity
ρ_r	(Ω m)	resistivity of randomly-oriented polycrystalline material
ρ_{xy}	(Ω m)	electrical resistivity component related to E_x and J_y
ρ_{yx}	(Ω m)	electrical resistivity component related to E_y and J_x
$\rho_{\parallel}$	(Ω m)	electrical resistivity parallel to crystal c-axis
$\rho_{\perp}$	(Ω m)	electrical resistivity perpendicular to crystal c-axis
σ	(Ω^{-1} m^{-1})	electrical conductivity
σ_e, σ_h	(Ω^{-1} m^{-1})	electrical conductivity of electron band, hole band
τ	(s)	relaxation time (mean free time between collisions)
ϕ	(deg)	Hall angle; also polar angle
ϕ_e , ϕ_h	(deg)	angle between current density and E-field in two-band model: electron, hole
ψ	(deg)	azimuthal angle
$\boldsymbol{\omega}$	(rad/s)	electron-cyclotron frequency vector
ω_c	(rad/s)	electron-cyclotron frequency

Chapter 1

INTRODUCTION

A curious feature of transition metal oxides is their wide range of conductivity, spanning roughly fifteen to twenty orders of magnitude when superconductors are not counted. For example, RuO_2 is a metal while rutile TiO_2 is an insulator, yet both have nearly identical structures. The work presented here is an experimental examination of a rare transition metal and its technologically useful dioxide, focusing on some of their interesting characteristics. For example, dominant charge carriers in Ru are holes while those in RuO_2 are electrons. How does the change from holes to electrons come about as oxygen is added to or lost from the lattice? Can RuO_2 films be manipulated by deposition processes to give a zero temperature-coefficient-of-resistance over a wide range of temperatures as claimed by some authors? This behavior, if true, would seem to violate a fundamental characteristic of metals above cryogenic temperatures, which is that resistivity must rise with temperature. Prior to this work, no Hall coefficient measurements in air or vacuum of thin films of Ru existed and only one such measurement set has been published for an RuO_2 thin film. No transport measurements have been made on either metal during the catalysis of CO, and the measurements reported here are unique and thus contribute to further understanding of the catalysis process. It is worth remembering that high-temperature superconductivity was discovered because of curiosity about the transport properties of transition-metal oxides. In the field of transition-metal oxides, discovery by experimentation seems to lead the way. Some background information is offered below as an introduction to the study.

1.1. Ruthenium

Ruthenium is element number 44 in the periodic table, located directly below iron and above osmium in Group VIII, but its properties resemble those of osmium more closely than iron.[1] There are four stable phases, and in addition to its lower temperature α phase, it exists in three higher temperature forms with the phase transitions: $\alpha^{1030\text{-}1040°C} \rightarrow \beta^{1200°C} \rightarrow \gamma^{ca.\ 1500°C} \rightarrow \delta$.[1] Ruthenium has a high melting temperature of 2334 °C, is resistant to chemical attack over a wide range of temperatures, and is used industrially as a catalyst and also as a hardener in metal alloys.[2]

Ruthenium is a transition metal with valence electrons occupying more than one shell ($4d^7$, $5s^1$).[3] A remarkable characteristic is that ten oxidation states are known to exist: +1 to +8 and also a 0 and -2 state.[1] Below 1000°C, ruthenium exhibits a hexagonal close packed structure (hcp), where adjacent planes of atoms follow an A-B-A stacking sequence.[4] Ruthenium is magnetoresistive and is a p-type compensated metal.[5] This means that the concentration of holes equals that of electrons and conduction involves both holes and electrons with higher mobility holes giving rise to the observed p-type behavior.[5,6] Table 1.1 lists certain physical properties of ruthenium measured on polycrystalline and single-crystal bulk samples that are relevant to this work.

TABLE 1.1. Physical properties of ruthenium.

Property	**Value**	**Reference**
Atomic number	44	
Atomic weight	101.07 g/mole	ICDD-0663[13]
Electron structure	2-8-18-15-1 or (Kr)$4d^7 5s^1$	
Crystal structure	hcp for α phase (≤ 1030 °C)	
Space group	$P6_3/mmc$ (194)	ICDD-0663[13]
Lattice constants, 20 °C		
a	2.7058 Å	ICDD-0663[13]
c	4.2819 Å	
c/a	1.5824	
Mass density, 20 °C	12.4 g/cm^3	ICDD-0663[13]
Melting temperature	2334 °C	Bever[2]
Resistivity, 0 °C	7.4 μΩ cm (single crystal, a-direction)	Volkenshteyn[11]
	5.4 μΩ cm (single crystal, c-direction)	
	6.67 μΩ cm (polycrystalline)	Justi[14]
	6.72 μΩ cm (polycrystalline)	Tainsh[15]
Resistivity, 23 °C	7.4 μΩ cm (polycrystalline)	Meaden[7]
Hall coefficient (polycrystalline)	+22 x 10^{-5} cm^3/C (20 °C, 2 to 2.9 A, 4.47 T)	Justi[14]
	+18 x 10^{-5} cm^3/C (22 °C, 0.45 to 2.3 T)	Volkenshteyn[11]

Ruthenium has approximately five times the resistivity of silver at room temperature and is therefore a very good conductor of electric current and heat.[7] The low resistivity is illustrated in Figure 1.1, which compares the resistivities of 67 metals in the periodic table at 295 K as a function of rank from smallest to largest, disregarding atomic number. The position of ruthenium is number 18 in the exponential ranking and is shown sandwiched between cadmium and indium.

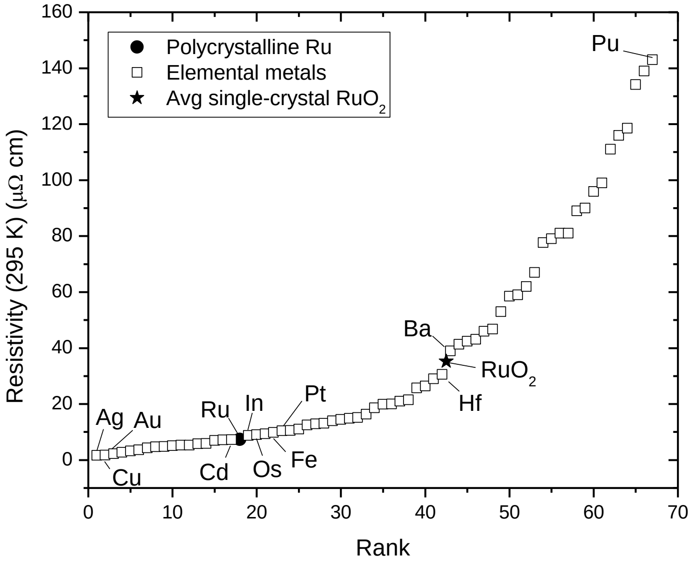

FIGURE 1.1. Resistivity of elemental metals at 295 K as a function of rank from smallest to largest (not by atomic number). Ruthenium is ranked 18th of the 67 metals plotted. An average single-crystal resistivity of ruthenium dioxide is shown for comparison. Residual resistivities have been subtracted from the elemental metals.[7]

The Hall coefficient is a more complex transport property and, in general, is known to be a function of temperature (e.g., Dy, OsO_2, $RuAl_2$, Sr_2RuO_4),[6, 8-10] magnetic field (e.g., Ru, Al, In),[6, 11] and phase (e.g., Cd: liquid n-type, solid p-type).[6] An experimental change in the magnitude and sign of the Hall coefficient gives information related to the curvature of the electron and hole Fermi surfaces (e.g., $CaRuO_3$, $SrRuO_3$).[12] Table 1.2 lists Hall coefficients in bulk and thin-film forms for several readily available transition metals for which sufficient data exist; these are compared to ruthenium. Neglecting sign, the Hall coefficient of metals generally ranges from about 2 to 22 x 10^{-5} cm^3/C, although it can be higher as seen in Figure 1.2, which is a plot of the Hall coefficient versus resistivity of 49 metals in the periodic table.

TABLE 1.2. Hall coefficients of 5 transition metals in bulk and thin-film form (293 K).

Element	**Crystal**	**RH$_{bulk}$ (10^{-5} cm^3/C)**	**RH$_{film}$ (10^{-5} cm^3/C)**	**References**
Copper	fcc[a]	-5.2	-5.5	Hurd[6c], Chopra[16d]
Silver	fcc	-8.5	-8.6	Hurd[6c], Chopra[16d]
Gold	fcc	-7.1	-8.1	Hurd[6]
Platinum	fcc	-2.3	-1.5 (50 Å)	Hurd[6]
Ruthenium	hcp[b]	+22	No data available	Justi[14]
		+18		Volkenshteyn[11]

[a] Face centered cubic
[b] Hexagonal close packed
[c] Bulk material
[d] Film

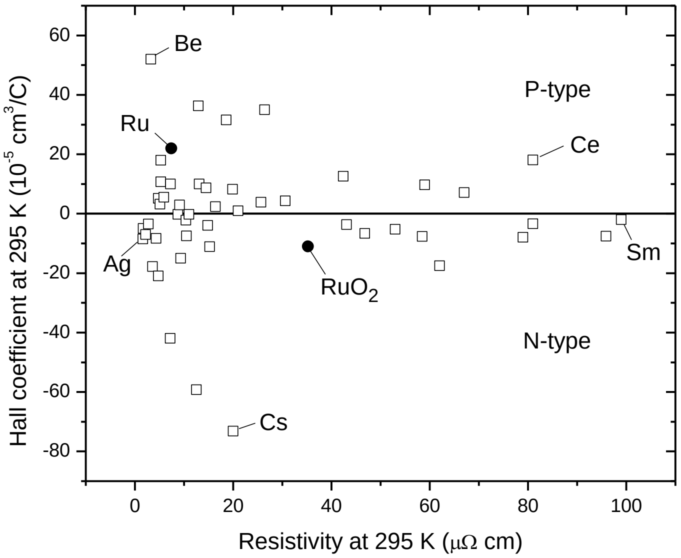

FIGURE 1.2. Hall coefficient versus resistivity of 49 metals in the periodic table (26 n-type and 23 p-type).[6] RuO_2 is included for comparison.

1.2. Transition Metal Oxides

The physical and chemical properties of the transition metals and their compounds are largely related to their d-shell electrons.[17] With respect to transition metal oxides, there is an enormous variability in electronic properties ranging from insulators (NiO) to semiconductors (TiO_{2-x}) to metals (RuO_2) to superconductors ($YBa_2Cu_3O_7$). That is, the metal-oxygen bonding may range anywhere from ionic to metallic, and transition metal oxides therefore may be classified according to their electronic properties. In the case of metallic conduction, examples of oxides that fall into the category of simple metals are RuO_2, ReO_3, and Na_xWO_3.[17, 18] In general, transition metal oxides have rather narrow electronic bands on the order of 1 to 2 eV.[19]

1.3. Ruthenium Oxides

Six oxides of ruthenium are mentioned in the literature.[1] The first (RuO) is rarely considered except to say that it may exist as a gas in some circumstances and that its existence in the solid state is doubtful. The second (RuO_2) has the rutile structure under normal pressures, is the most thermodynamically stable, and has significant technological interest. RuO_2 takes on a cubic phase with a modified-fluorite structure at pressures above 12 GPa, which can be metastably retained when the pressure is lowered to one atmosphere.[20] The third (RuO_3) is known to exist as a vapor at 1200 °C and may play a role in the stability of RuO_2 surfaces.[21] The fourth (RuO_4) is a highly volatile yellow crystal that melts at 25.4 °C, boils at 40 °C, and is toxic. The fifth (Ru_2O_3) has the corundum structure, has never been isolated in the solid state, and has been observed only as a hydrate ($Ru_2O_3 \bullet xH_2O$).[22] The sixth (Ru_2O_5) is hardly mentioned in the literature.

1.4. Ruthenium Dioxide

The technologically interesting oxide of ruthenium, the semi-transparent, deep blue ruthenium dioxide (RuO_2), is a 4d oxide that exhibits “metallic” metal-oxygen bonding. Recalling that electrical conductivity is directly proportional to the density of states at the Fermi surface, RuO_2 is classified as a metal since its Fermi level lies in the middle of a conduction-band density-of-states curve that is comprised primarily of Ru-4d orbitals as shown in Figure 1.3.[18]

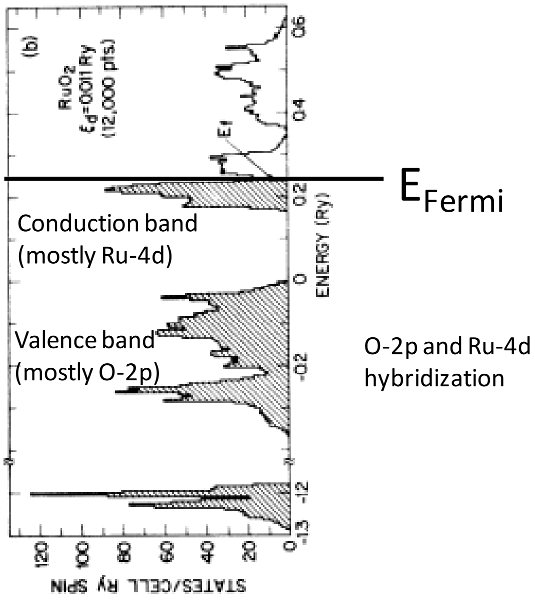

FIGURE 1.3. Density-of-states plot of RuO_2 that shows the Fermi energy level in the middle of the conduction band, which is the definition of a metal according to energy-band theory. (Reproduction of Figure 7, reference 18)

In its single crystal state, RuO_2 has a higher electrical conductivity than about one-third of the pure metals in the periodic table (see Figure 1.1), although polycrystalline specimens generally show a lower conductivity.[7, 23] The resistivities of RuO_2 in the [100] and [001] directions at 300 K are 36.1 and 35.7 μΩ cm respectively, and the average single-crystal resistivity is reported to be 35.2 ± 0.5 μΩ cm.[23] The increase in resistivity with increasing temperature of single-crystal RuO_2 clearly shows its metallic behavior as seen in Figure 1.4.[23, 24]

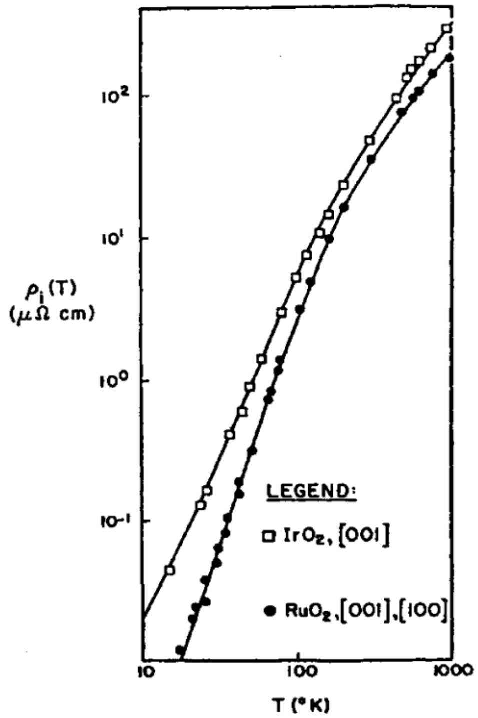

FIGURE 1.4. Resistivity versus temperature of IrO_2 and RuO_2 single crystals. Metallic behavior is indicated. (Reproduction of Figure 2, reference 23)

The energy-versus-wave vector dispersion bands at the Fermi level for RuO_2 indicate two-carrier conduction. Hall measurements show electrons as the dominant carriers, thereby making RuO_2 an n-type metal in contrast to Ru, which is a p-type metal.[18, 25, 26] To be specific, single-crystal RuO_2 has an average room-temperature Hall coefficient of -11×10^{-5} cm^3/C.[23]

Ruthenium dioxide possesses a rutile structure (Structurbericht C4, space group $P4_2/mnm$), which consists of a tetragonal lattice with two RuO_2 molecules per unit cell and octahedral coordination with each ruthenium atom surrounded by six oxygen nearest neighbors as shown in Figure 1.5.[27] The unit cell lattice parameters are a = 4.492 Å and c = 3.107 Å.[28] It is also the most thermodynamically stable oxide of ruthenium, although studies of single-crystal (110) and (100) surfaces suggest highly non-stoichiometric surfaces.[21] The possible non-stoichiometry of surfaces may contribute to oxygen loss under certain conditions, and it will be shown in Chapters 6 and 7 that the stability of many polycrystalline thin films is related to the choice of environmental atmosphere and temperature. Some physical properties of RuO_2 are summarized in Table 1.3.

In terms of technology, ruthenium dioxide finds uses as diffusion barriers, electrodes, thick-film resistors, thin-film resistors and catalysts. An extensive summary of applications of RuO_2, emphasizing catalysis but including more exotic uses such as extreme ultraviolet lithography, is given in a paper by Assmann et al.[30]

TABLE 1.3. Physical properties of ruthenium dioxide.

Property	**Value**	**Reference**
Crystal structure	tetragonal (rutile)	ICDD 2008[28]
Space group	$P4_2/mnm$	Birkholz[27]
Lattice constants at 20 °C		
a	4.492 Å	ICDD 2008[28]
c	3.107 Å	
c/a	0.692	
Mass density at 20 °C	7.2 g/cm^3	ICDD 2008[28]
Dissociation temperature	1540 °C (1 atm oxygen)	Bell[29]
Electrical resistivity at 27 °C	36.1 μΩ cm [100] (single crystal) 35.7 μΩ cm [001] (single crystal) 35.2 μΩ cm (avg)	Ryden[23]
Hall coefficient at 27 °C	-11×10^{-5} (avg)	Ryden[23]

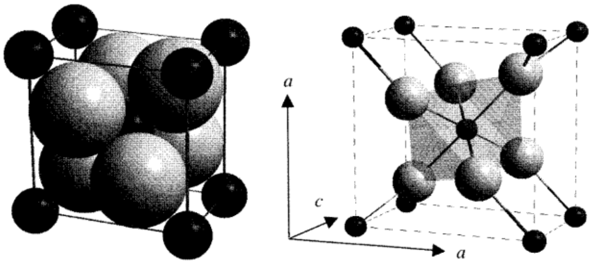

FIGURE 1.5. Two crystallographic representations of the rutile structure, which has a tetragonal unit-cell lattice. (Reproduction of Figure s5.1, reference 27)

1.5. Chapter Organization

The research objective of this work has been the investigation of the electronic transport properties of polycrystalline thin films of ruthenium and ruthenium dioxide as a function of temperature and atmosphere. In terms of chapter organization for the thesis, Chapter 2 outlines some theoretical aspects of transport theory as it relates to electrical resistivity and the Hall coefficient. Chapter 3 defines the experimental arrangement from which measurements were obtained. Chapter 4 compares the transport properties of planar and nanorod-structured ruthenium thin films to each other and to measurements from bulk samples. Chapter 5 presents a parametric study that relates the deposition process, structure, and transport properties of RuO_2 planar thin films and shows that changes in film deposition conditions can alter the nanostructure and mode of conduction from electron-to-hole dominance. Chapter 6 considers the unexpected instability found in some of the RuO_2 thin films when annealed in high vacuum at temperatures slightly above room temperature. Chapter 7 investigates how transport properties are altered by the process of carbon monoxide reactivity and catalysis on surfaces of RuO_2 and Ru.

Chapter 8 summarizes the results and makes recommendations for future work. Finally, two appendices include additional material related to specific sample parameters and transport measurement calibration.

---

[1] J. C. Bailar, H. J. Emeleus, R. Nyholm and A. F. Trotman-Dickenson, *Comprehensive Inorganic Chemistry* (Pergamon, Oxford, 1973).

[2] M. B. Bever, ed., *Encyclopedia of Materials Science and Engineering*, (Pergamon, Oxford, 1986).

[3] R.W. Cahn, P. Haasen and E. J. Kramer, eds., *Materials Science and Technology*, (Wiley, New York, 2005).

[4] N. W. Ashcroft and N. D. Mermin, *Solid State Physics*, (Brooks/Cole, 1976).

[5] N. E. Alekseevskii, K.-H. Bertel, A. V. Dubrovin, V. I. Nizhankovskii and L. Urai, JETP Lett. 18, 5, 163 (1973).

[6] C. M. Hurd, *The Hall Effect in Metals and Alloys* (Plenum, New York, 1972).

[7] G. T. Meaden, *Electrical Resistance of Metals* (Plenum, New York, 1965).

[8] Y. Hayakawa, S. Kohiki, M. Arai, H. Yoshikawa, S. Fukushima, K. Wagatsuma, M. Oku and F. Shoji, Phys. Rev. B 59, 11125 (1999).

[9] D. Mandrus, V. Keppens, B. C. Sales and J. L. Sarrao, Phys. Rev. B 58, 3712 (1998).

[10] A. P. Mackenzie, N. E. Hussey, A. J. Diver, S. R. Julian, Y. Maeno, S. Nishizaki and T. Fujita, Phys. Rev. B 54, 7425 (1996).

[11] N. V. Volkenshteyn, V. A. Novoselov, V. Y. Startsev and Y. P. Romanov, Fiz. Metal. Metalloved. 33, 6, 1233 (1972).

[12] S. C. Gausepohl, M. Lee, R. A. Rao and C. B. Eom, Phys. Rev. B, 54, 8996 (1996).

[13] International Centre for Diffraction Data, pdf file 00-006-0663, (2007).

[14] E. Justi, Z. Naturforsch. 4A, 472 (1949).

[15] R. J. Tainsh and G. K. White, Can. J. Phys. 42, 208 (1964).

[16] K. L. Chopra and S. K. Bahl, J. Appl. Phys. 38, 3607 (1967).

[17] P. A. Cox, *Transition Metal Oxides*, (Clarendon, Oxford, 1992).

[18] L. F. Mattheiss, Phys. Rev. B 13, 2433 (1976).

[19] C. N. R. Rao and B. Raveau, *Transition Metal Oxides* (VCH, New York, 1995).

[20] J. M. Leger, P. Djemia, F. Ganot, J. Haines, A. S. Pereira and J. A. H. da Jornada, Appl. Phys. Lett. 79, 2169 (2001).

[21] V. E. Henrich and P. A. Cox, *The Surface Science of Metal Oxides*, (Cambridge, 1994).

[22] M. E. Grillo, Phys. Rev. B 70, 184115 (2004).

[23] W. D. Ryden, A. W. Lawson and C. C. Sartain, Phys. Rev. B 1, 1494 (1970).

[24] J. J. Lin, S. M. Huang, Y. H. Lin, T. C. Lee, H. Liu, X. X. Zhang, R. S. Chen and Y. S. Huang, J. Phys.: Condens. Matter 16, 8035 (2004).

[25] K. M. Glassford and J. R. Chelikowsky, Phys. Rev. B 47, 1732 (1993).

[26] K. M. Glassford and J. R. Chelikowsky, Phys. Rev. B 49, 7107 (1994).

[27] M. Birkholz, *Thin Film Analysis by X-Ray Scattering* (Wiley-VCH, Weinheim, 2006).

[28] International Centre for Diffraction Data, pdf file 04-003-2008, (2008).

[29] W.E. Bell and M. Tagami, J. Phys. Chem. 67, No. 11, 2432 (1963).

[30] J. Assmann, V. Narkhede, N.A. Breuer, M. Muhler, A.P. Seitsonen, M. Knapp, D. Crihan, A. Farkas, G. Mellau, H. Over, J. Phys.: Condens. Matter 20, 184017.

Chapter 2

ELECTRONIC TRANSPORT PROPERTIES

It is almost an understatement to say that charge transport in solids is a complex subject. For example, when considering electric or thermal currents in a magnetic field, one study states that "560 effects are theoretically possible in a transverse magnetic field only!"[1] In recognition of this complexity, the following discussion of the properties of resistivity and Hall effect will be restricted to what applies directly to the experiments considered here. For anyone wishing to delve deeper into the subject, three excellent texts by Jan,[1] Meaden,[2] and Hurd[3] are a good place to start.

2.1. Ohm's Law

Consider a homogeneous electrical conductor at a uniform constant temperature that is not in an external magnetic field. It is assumed that the conductor has an electron chemical potential that is a function of temperature alone (e.g., a metal). If an external current source imposes a current density on the conductor as was done in this study, then the phenomenological response is an electric field in the conductor multiplied by a temperature-dependent material parameter called the resistivity, which is assumed to be independent of both the current density and the electric field.[2] This familiar statement of Ohm's law reads

$$\boldsymbol{E} = \rho \boldsymbol{J} \tag{2.1}$$

where the electric field $\boldsymbol{E}$ and current density $\boldsymbol{J}$ are vectors and, in general, the resistivity ρ is a second-rank tensor because $\boldsymbol{E}$ and $\boldsymbol{J}$ are in different directions due to material anisotropy. Ohm's law is here written in this form, rather than as $\boldsymbol{J} = \sigma \boldsymbol{E}$ (σ is conductivity), because the experimental arrangement uses a current source rather than a voltage source as the forcing function, making ***J*** the independent variable. In component form (2.1) is

$$\begin{pmatrix} E_x \\ E_y \\ E_z \end{pmatrix} = \begin{pmatrix} \rho_{xx} & \rho_{xy} & \rho_{xz} \\ \rho_{yx} & \rho_{yy} & \rho_{yz} \\ \rho_{zx} & \rho_{zy} & \rho_{zz} \end{pmatrix} \begin{pmatrix} J_x \\ J_y \\ J_z \end{pmatrix}. \tag{2.2}$$

From energy considerations, a reciprocity relation holds where $\rho_{ij} = \rho_{ji}$.[4, 5] But in crystals with planes of symmetry perpendicular to each of the crystallographic axes, such as tetragonal RuO_2 or hexagonal-close-packed Ru, the components ρ_{ij} are zero for $i \neq j$ (in the absence of an external magnetic field).[4] Perhaps one way to see this is to write the expression for power density, *p*, which is the dot product of the vectors **E** and **J**, and then substitute for the components of **E** in terms of resistivities.

$$p = \boldsymbol{E} \cdot \boldsymbol{J} = E_x J_x + E_y J_y + E_z J_z \tag{2.3}$$

$$p = \rho_{xx} J_x^2 + 2\rho_{xy} J_x J_y + \rho_{yy} J_y^2 + 2\rho_{xz} J_x J_z + 2\rho_{yz} J_y J_z + \rho_{zz} J_z^2 \tag{2.4}$$

If the direction of the y axis is arbitrarily reversed, for example, the sign of J_y would change, which would mean that (2.4) would take the form

$$p = \rho_{xx} J_x^2 - 2\rho_{xy} J_x J_y + \rho_{yy} J_y^2 + 2\rho_{xz} J_x J_z - 2\rho_{yz} J_y J_z + \rho_{zz} J_z^2 \tag{2.5}$$

which is a lower power density. However, arbitrarily reversing the direction of the axis has not changed the perpendicular planes of symmetry, and without a physical change in the lattice the power density cannot change. Therefore, components of resistivity that are off the main diagonal must be zero. The presence of an external magnetic field can, however, modify the resistivity tensor so that components that are off the main diagonal can become non-zero (e.g., Hall effect) and, furthermore, components can become a function of field (magnetoresistance).

As shown by Jan,[1] the presence of a non-uniform temperature and a spatially dependent chemical potential will significantly complicate Ohm's law.

$$\boldsymbol{E} = \rho \boldsymbol{J} - \boldsymbol{S}\boldsymbol{\nabla}\mathrm{T} - \frac{1}{\mathrm{e}}\boldsymbol{\nabla}\xi \tag{2.6}$$

The second-rank tensor **S** is the thermoelectric power (Seebeck coefficient), T is temperature, e is the magnitude of the charge on the electron (+1.6 x 10^{-19} C), and ξ is the chemical potential of the electrons.[1] In the experiments considered here, all resistivity measurements were done with no external field and with near isothermal conditions, as will be explained in Chapter 3. This approach simplifies ρ (no field dependence) and eliminates $\boldsymbol{\nabla}\mathrm{T}$. The final term on the right hand side of (2.6) depends on composition, stoichiometry, and structure.

When dealing with metals of a uniform composition such as Ru or RuO_2, the electron chemical potential term in (2.6) vanishes because it has no spatial gradient. However, it should be noted that the assumption of a uniform composition does not apply to two-phase mixtures of Ru and RuO_2, as were sometimes encountered in this study, and to be strictly correct, it might be necessary to add the $(1/\mathrm{e})\boldsymbol{\nabla}\xi$ term to the right-hand side of (2.1) for those cases. That is, differences in electron concentrations in the two materials would give rise to a gradient in chemical potential at the grain boundaries. Strictly speaking, this gradient must be evaluated across boundaries from one material to the next, since the gradient is zero within a given crystallite of uniform composition. Note that in this study, no attempt has been made to correct measured resistivities for any effects of electron chemical potential due to grain boundaries between different material phases; these effects are assumed to be small and have been neglected. If the distribution of crystallites in a two-phase system is uniform, then presumably a sum of the gradients of chemical potential at grain boundaries should either be small or add to zero.

The tensor of high-symmetry anisotropic single crystals in the absence of a magnetic field may be written in terms of three resistivities as stated above.[2] Let the a- and b-axes of a single crystal correspond to the x and y directions and the c-axis correspond to the z direction. Furthermore, let the current density vector be defined with respect to the c-axis as shown in Figure 2.1, which is taken as the principal crystal axis with a resistivity of $\rho_{\parallel}$. The other two resistivities are defined as $\rho_{\perp 1}$ and $\rho_{\perp 2}$.

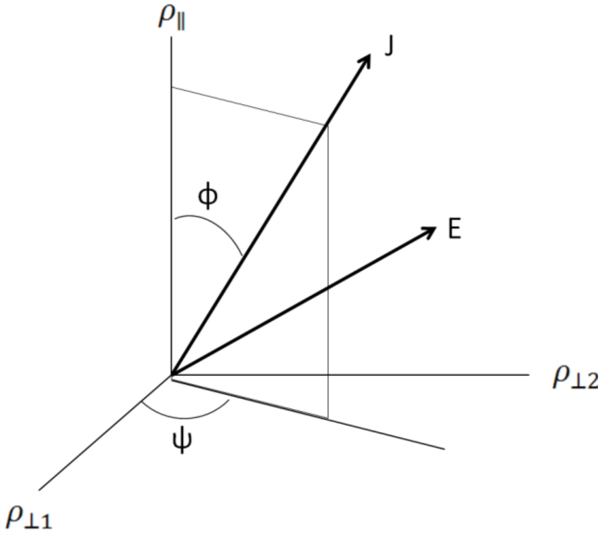

FIGURE 2.1. Current density **J** as an input and electric field **E** as a response in an anisotropic crystal. (Modification of Fig. 1, reference 2)

Writing the components of **J** in terms of angles, Ohm's law follows as

$$\begin{pmatrix} E_x \\ E_y \\ E_z \end{pmatrix} = \begin{pmatrix} \rho_{\perp 1} & 0 & 0 \\ 0 & \rho_{\perp 2} & 0 \\ 0 & 0 & \rho_{\parallel} \end{pmatrix} \begin{pmatrix} J \sin\phi \cos\psi \\ J \sin\phi \sin\psi \\ J \cos\phi \end{pmatrix}. \tag{2.7}$$

A scalar resistivity as a function of the angles φ and ψ follows from

$$\rho(\phi,\psi) = \frac{\boldsymbol{E}\cdot\boldsymbol{J}}{\boldsymbol{J}\cdot\boldsymbol{J}} = \rho_{\perp 1}\sin^2\phi cos^2\psi + \rho_{\perp 2}\sin^2\phi sin^2\psi + \rho_{\parallel}\cos^2\phi. \tag{2.8}$$

Given a single crystal and a current density oriented at known angles with respect to the crystal, it is therefore theoretically possible to determine the three components of resistivity through a series of measurements.[2]

The resistivity tensor of some anisotropic metals such as hexagonal-close-packed Ru may be simplified somewhat by noting that the resistivity components perpendicular to the c-axis of an hcp single crystal are equal.[2] It is then possible to write Ohm's law in terms of perpendicular, $\rho_{\perp}$, and parallel, $\rho_{\parallel}$, resistivities as

$$\rho(\phi,\psi) = \rho_{\perp}\sin^2\phi + \rho_{\parallel}\cos^2\phi = \rho_{\perp} + (\rho_{\parallel} - \rho_{\perp})\cos^2\phi \tag{2.9}$$

When this expression is integrated over the entire solid angle, an average value of resistivity[2] follows as

$$\bar{\rho} = \frac{2\rho_{\perp}}{3} + \frac{\rho_{\parallel}}{3}. \tag{2.10}$$

This shows how the resistivity of a Ru polycrystalline sample is weighted by the components that are perpendicular and parallel to the principal axis (c-axis) of the crystal.[6, 2]

For a rutile tetragonal RuO_2 crystal, the parallel and perpendicular resistivities are found by experiment to be approximately equal. Ryden et al.[7] show that 300 K resistivities of RuO_2 in the [100] and [001] directions are 36.1 and 35.7 μΩ cm respectively, which is about a 1 percent difference. In fact, RuO_2 is nearly isotropic with respect to resistivity, with the biggest difference due to changes in crystal orientation being about 10 percent.[7]

Now refer to the slab model of a homogeneous, isotropic conductor shown in Figure 2.2. Assume an x-directed current density, which may be written as the excitation current divided by the cross-sectional area (I/wt), and a corresponding x-directed electric field, which may be written as (V/L), where V is the potential difference along the slab length L. The average resistivity is

$$\rho = \frac{E}{J} = \frac{\left(\frac{V}{L}\right)}{\left(\frac{I}{wt}\right)} = \left(\frac{wt}{L}\right)\left(\frac{V}{I}\right). \tag{2.11}$$

Since Ohm's law is a linear function with an odd parity, a reversal of current direction will correspond to a reversal of the potential gradient. Therefore, for a homogeneous, isotropic slab it would be expected that $V(+I) = -V(-I)$. Measurements such as those described in ASTM F76-86 make use of this property and specify resistivity as an average written in the form[8]

$$\rho = \left(\frac{wt}{L}\right)\left(\frac{V(+I) - V(-I)}{2I}\right). \tag{2.12}$$

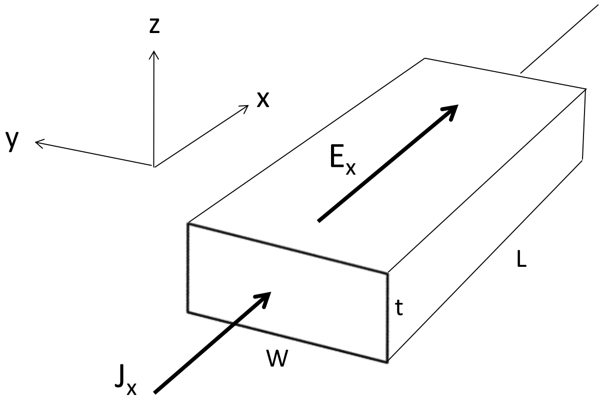

FIGURE 2.2. Slab model of a homogeneous, isotropic conductor.

2.2. Matthiessen’s Rule

The resistivity of metals may be written as a sum of two terms, which is called Matthiessen’s rule: a temperature-independent contribution ρ_o and a temperature-dependent contribution ρ_i, called the ideal resistivity.[2] The ρ_o term is associated with lattice defects such as impurities, point defects, and strain; the ρ_i term is associated with phonon scattering of electrons by the lattice at finite temperatures. For metals, the phonon scattering term increases linearly with increasing temperature and the impurity term is independent of temperature.

$$\rho(T) = \rho_o + \rho_i(T) \tag{2.13}$$

Since the carrier concentrations in metals are independent of temperature, it is, of course, the decreasing carrier mobilities with increasing temperatures that make ρ_i a function of temperature.

2.3. Hall Coefficient

All measurements of the Hall effect were made in the low-field condition where the product of the electron-cyclotron frequency ω_c and the mean free time between collisions τ, typically about 10^{-14} seconds, is much less than one ($\omega_c\tau \ll 1$).[3] What the low-field condition means in a practical sense is that the applied magnetic fields are below about 0.5 T, temperatures are at or above room temperature, and typically the samples have high defect contents. The high-field condition, where $\omega_c\tau \gg 1,$ is practically achieved at cryogenic temperatures in fields above about 5 T using very pure samples. In the high-field condition, electrons are able to complete one or more cyclotron orbits before being scattered and Hall coefficients are determined by the topology of the Fermi surface of the metal.[3] Note that in consideration of the Hall effect, signs can be problematic. In what is given below, the Lorentz force on charge carriers is taken to define a y-directed electric field. The steady-state response to this field when current is not allowed to flow in the y-direction is another equal and opposite electric field called the Hall field.[9 - 11]

Consider a homogeneous, isotropic, and isothermal conductor (Figure 2.3) subjected to an x-directed current density $\boldsymbol{J} = J_x\hat{\boldsymbol{x}}$ and a z-directed (transverse) magnetic field $\boldsymbol{B} = B_z\hat{\boldsymbol{z}}$ (where $\hat{\boldsymbol{x}}$ and $\hat{\boldsymbol{z}}$ are unit vectors in the positive x- and z-directions). The Lorentz force density on charge carriers is given by the vector cross product of $\boldsymbol{J}$ and $\boldsymbol{B}$. This force density equals the charge concentration, n, multiplied by the Lorentz force on a single carrier **f**. In equation form,

$$\boldsymbol{F} = n\boldsymbol{f} = \boldsymbol{J}\; x\; \boldsymbol{B} \tag{2.14}$$

The cross product becomes $J_xB_z(-\hat{\boldsymbol{y}})$, where $\hat{\boldsymbol{y}}$ is defined as a unit vector in the y-direction. Hence, the force on a single charge carrier may be replaced by the product of the charge q and a pseudo-electric field $\boldsymbol{E}_L$. That is, the y-directed Lorentz electric field takes the form

$$\boldsymbol{E}_L = \frac{1}{nq}\boldsymbol{J}\; x\; \boldsymbol{B} = \frac{J_xB_z}{nq}(-\hat{\boldsymbol{y}}). \tag{2.15}$$

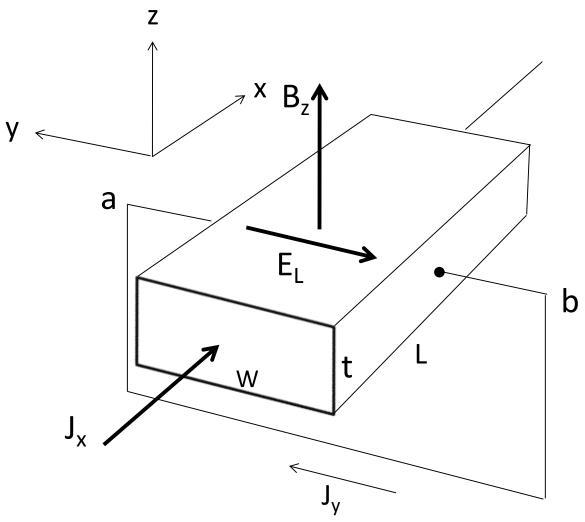

FIGURE 2.3. Slab model of an isothermal, homogeneous conductor showing an electric field E_L due to the Lorentz force and wires labeled a and b that allow a current flow in the y-direction.

With reference to Figure 2.3, if wires a and b are connected to make a closed circuit, a y-directed current density will flow in the slab because of the Lorentz force. If, on the other hand, wires a and b are left open as in Figure 2.4, then charges of different polarity will accumulate on opposite faces of the slab (faces perpendicular to the y-axis). These charges give rise to an additional electric field called the Hall field that is equal and opposite to the Lorentz electric field under steady-state conditions. That is, the x-directed transport current is no longer deflected by the magnetic field under steady-state conditions. The equal and opposite Hall electric field takes the form

$$\boldsymbol{E}_y = -\boldsymbol{E}_L = -\frac{1}{nq}\boldsymbol{J}\ x\ \boldsymbol{B} = \frac{J_x B_z}{nq}\hat{y} \tag{2.16}$$

If there are single carriers that are electrons, then q is replaced by -e and (2.16) becomes

$$\boldsymbol{E}_y = E_y\hat{y} = -\frac{J_x B_z}{ne}\hat{\boldsymbol{y}} \quad (electrons) \tag{2.17}$$

where the charge on the electron e is taken as +1.6 x 10^{-19} Coulombs. If there are single carriers that are holes, then q is replaced by +e and (2.16) becomes

$$\boldsymbol{E}_y = E_y\hat{y} = \frac{J_x B_z}{ne}\hat{\boldsymbol{y}} \quad (holes). \tag{2.18}$$

These equations show how the Hall effect can classify a material as either n- or p-type (negative or positive) based on the polarity of a voltage measurement in the y-direction.

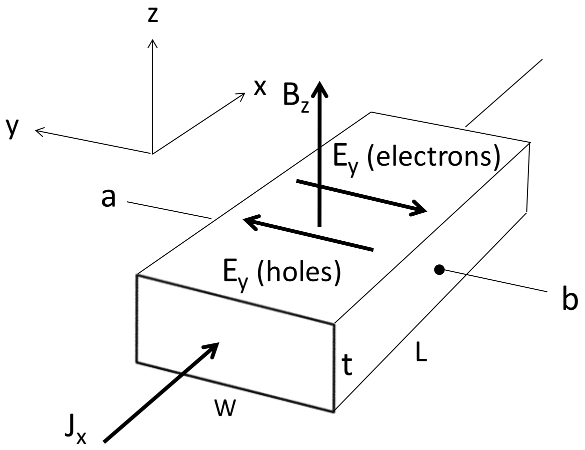

FIGURE 2.4. Slab conductor with wires a and b open, which allows charges of opposite polarity to accumulate on the a and b faces of the slab. These charges give rise to a Hall electric field E_y that points in a direction that depends on whether conduction occurs by electrons or by holes.

From equation (2.17), a basic Hall coefficient may be defined for electrons as

$$R_H = \frac{E_y}{J_x B_z} = \frac{\rho_{yx}}{B_z} = -\frac{1}{ne} \quad (electrons). \tag{2.19}$$

Similarly, from equation (2.18), a basic Hall coefficient may be defined for holes as

$$R_H = \frac{E_y}{J_x B_z} = \frac{\rho_{yx}}{B_z} = +\frac{1}{ne} \quad (holes). \tag{2.20}$$

The sign of R_H is determined experimentally by the sign of the potential difference $V_b - V_a$ (see Figure 2.4).

Note that the basic form of the Hall coefficient given in (2.19) and (2.20) is not applicable to ruthenium because it is a compensated metal where the number of electrons equals the number of holes.[3] Furthermore, the basic form probably does not apply to ruthenium dioxide either, because it is likely that the electron and hole concentrations in ruthenium dioxide are also equal (or nearly equal). The more complicated expression for the Hall coefficient of a compensated metal will be given below in the section on the two-band model.

In order to develop the resistivity tensor in a transverse magnetic field $\boldsymbol{B}$, one can assume a homogeneous and isotropic material and allow current to flow in all three (x,y,z) directions in the slab in response to an electric field $\boldsymbol{E}$. In the relaxation-time approximation, the total force on a charge q equals the sum of the forces due to the electric field, the Lorentz force, and a damping term that is directly proportional to the average velocity of the charge and inversely proportional to a scattering relaxation time τ.[1 - 3, 9 - 11] The force reads

$$m\frac{d\boldsymbol{v}}{dt} = q(\boldsymbol{E} + \boldsymbol{v}\; x\; \boldsymbol{B}) - \frac{m\boldsymbol{v}}{\tau} \tag{2.23}$$

where m is the effective mass of an electron. Under steady-state conditions the average momentum is unchanging so that the left-hand side of (2.23) is zero. Multiplying both sides by $nq\tau/m$ yields

$$0 = \frac{nq^2\tau}{m}(\boldsymbol{E} + \boldsymbol{v}\; x\; \boldsymbol{B}) - nq\boldsymbol{v}. \tag{2.24}$$

This yields an equation for the electric field that can be written in terms of the current density $\boldsymbol{J}$,

$$\boldsymbol{E} = \rho \boldsymbol{J} - \boldsymbol{v}\, x\, \boldsymbol{B} \tag{2.25}$$

where the resistivity ρ equals $m/nq^2\tau$, neglecting any magnetoresistance effects. Furthermore, the $\boldsymbol{v}\, x\, \boldsymbol{B}$ term may be written as $\rho(q\tau/m)\,\boldsymbol{J}\, x\, \boldsymbol{B}$ yielding

$$\boldsymbol{E} = \rho \boldsymbol{J} - \rho\left(\frac{q\tau}{m}\right)\boldsymbol{J}\, x\, \boldsymbol{B}. \tag{2.26}$$

At this point it is possible to write the tensor form of the transport equation depending on whether electrons or holes are the primary charge carriers. That is, for electrons q is replaced by -e. Setting the term $(e/m)\boldsymbol{B}$ equal to **ω**, the cyclotron frequency in vector form, yields

$$\boldsymbol{E} = \rho \boldsymbol{J} + \rho\tau\, \boldsymbol{J}\, x\, \boldsymbol{\omega} \quad (electrons). \tag{2.27}$$

For holes, q is replaced by +e, which yields

$$\boldsymbol{E} = \rho \boldsymbol{J} - \rho\tau\, \boldsymbol{J}\, x\, \boldsymbol{\omega} \quad (holes). \tag{2.28}$$

In the above equations the resistivities are assumed to be independent of magnetic field. When the equations are written as tensors, there are two resulting forms. For electrons, the transport relation between electric field and current density takes the form[1]

$$\begin{pmatrix} E_x \\ E_y \\ E_z \end{pmatrix} = \begin{pmatrix} \rho & \omega\tau\rho & 0 \\ -\omega\tau\rho & \rho & 0 \\ 0 & 0 & \rho \end{pmatrix} \begin{pmatrix} J_x \\ J_y \\ J_z \end{pmatrix} \quad (electrons). \tag{2.29}$$

For holes, the signs of the off-diagonal resistivities are reversed to yield

$$\begin{pmatrix} E_x \\ E_y \\ E_z \end{pmatrix} = \begin{pmatrix} \rho & -\omega\tau\rho & 0 \\ \omega\tau\rho & \rho & 0 \\ 0 & 0 & \rho \end{pmatrix} \begin{pmatrix} J_x \\ J_y \\ J_z \end{pmatrix} \quad (holes). \tag{2.30}$$

In general, when all magnetic field effects are included, the resistivities ρ_{xx} and ρ_{yy} are equal and represent transverse magnetoresistivities. The resistivity ρ_{zz} represents a longitudinal magnetoresistivity, since the current and magnetic field are parallel. The resistivity ρ_{yx}, which equals $\omega\tau\rho$, represents the Hall resistivity. In the low-field condition with $\omega\tau << 1$, it is seen that the Hall resistivity is much lower than the bulk resistivity ρ.

In practice, the definition of the Hall coefficient is more sophisticated than that given above. Recalling that a well-behaved, arbitrary mathematical function can be summed with itself to form either an odd or even function, the y-directed electric field can be summed with itself to form an odd function.[12] The Hall field E_H that is reported in measurements is then defined as an odd function formed from E_y (when B_z is taken as a positive magnitude) as follows[3]

$$E_H = \frac{1}{2}\left[E_y(+B_{\boldsymbol{z}}) - E_y(-B_{\boldsymbol{z}})\right]. \tag{2.31}$$

(To clarify the nomenclature in (2.31), the electric field $E_y(+B_{\boldsymbol{z}})$ should be read: "E_y as a function of plus B_z.") There is no name for the corresponding even electric field function, which for high-symmetry crystals should be very small or zero. Assuming that the electric field E_y is directly proportional to J_xB_z, the Hall coefficient may be thought of as an off-main-diagonal resistivity per unit field ρ_{yx}/B_z as stated above.

$$R_H = \frac{E_H}{J_xB_z} = \frac{\frac{1}{2}\left[\frac{E_y(+B_{\boldsymbol{z}})}{J_x} - \frac{E_y(-B_{\boldsymbol{z}})}{J_x}\right]}{B_z} = \frac{\frac{1}{2}\left[\rho_{yx}(+B_{\boldsymbol{z}}) - \rho_{yx}(-B_{\boldsymbol{z}})\right]}{B_z} \to \frac{\rho_{yx}}{B_z}. \tag{2.32}$$

Note that there is a more general definition that defines the Hall coefficient in terms of the gradient of E_H with respect to B_z, but for the purposes of this work, (2.32) is sufficient.[3]

In order to improve measurement accuracy, the test standard ASTM F76-86 extends the definition even further to make an odd function of the y-directed electric field based on a reversal of input current. That is, the definition of E_H as an odd function of B_z alone is extended to make E_H an odd function of both B_z and J_x. The Hall coefficient then reads

$$R_H = \frac{1}{2}\left\{\frac{\frac{1}{2}\left[E_y(+B_{\boldsymbol{z}}, +J_x) - E_y(-B_{\boldsymbol{z}}, +J_x)\right]}{J_x B_z} - \frac{\frac{1}{2}\left[E_y(+B_{\boldsymbol{z}}, -J_x) - E_y(-B_{\boldsymbol{z}}, -J_x)\right]}{J_x B_z}\right\} \tag{2.33}$$

where J_x and B_z are taken as positive quantities.

With reference to Figure 2.4, the y-directed electric field may be replaced by the negative gradient of the potential (V_y/w) and the current density by the x-directed current divided by the slab cross-sectional area (I_x/wt). When these substitutions are made, the resulting equation for R_H is in the form given in ASTM F76-86:

$$R_H = \frac{t}{4 I_x B_z}\left\{\left[V_y(+B_{\boldsymbol{z}}, +I_x) - V_y(-B_{\boldsymbol{z}}, +I_x)\right] - \left[V_y(+B_{\boldsymbol{z}}, -I_x) - V_y(-B_{\boldsymbol{z}}, -I_x)\right]\right\}. \tag{2.34}$$

Note that sample thickness t is the only geometrical factor included in the expression.

2.4. Two-Band Model

In cases where two charge carriers are involved in transport, one may resort to a two-band model that assumes overlapping electron and hole bands.[1, 3] The model assumes that interband transitions are not allowed and that resistivities due to each band are additive. To quote Hurd, it is a “crude oversimplification of the conduction process in most metals.” [3] However, it does give insight into the conduction process, avoids intractable mathematics, and is often applied to transition metals (electrons from an s-band and holes from a d-band). Figure 2.5 shows a vector diagram, taken from Jan,[1] which defines the relationship between a resultant electric field, which is the sum of the applied and Hall fields, and the electron and hole current densities.

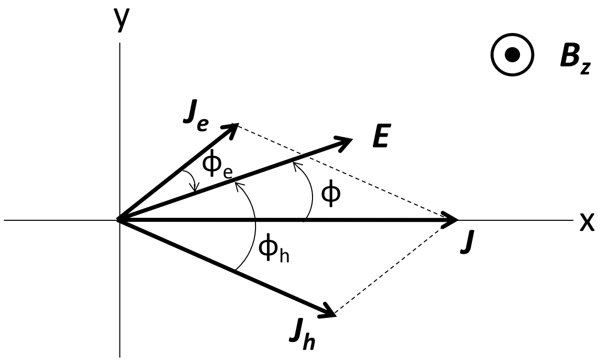

FIGURE 2.5. Two-band model showing a resultant electric field $\boldsymbol{E}$, which is the sum of an applied field $\boldsymbol{E_x}$ and the Hall field $\boldsymbol{E_y}$, and current densities in an electron band $\boldsymbol{J_e}$ and hole band $\boldsymbol{J_h}$ that add to give a resultant current density $\boldsymbol{J}$. Hall angles are counterclockwise positive. The magnetic field $\boldsymbol{B_z}$ points out of the paper toward the reader. (Reproduction of Fig.7, reference 1)

The model makes use of conductivities in the electron and hole bands according to the following definitions

$$\sigma_e = \frac{J_e}{E\cos\phi_e}, \quad \sigma_h = \frac{J_h}{E\cos\phi_h}. \tag{2.35}$$

It is noted that the x-components of the electron and hole current densities add together to equal the total current density J and that the y-components of the current densities add to zero. This yields equations for the current density and tangent of the Hall angle ϕ, which is defined as the ratio E_y/E_x:

$$J = J_e\cos(\phi - \phi_e) + J_h\cos(\phi_h - \phi) \tag{2.35}$$

$$\tan\phi = \frac{\sigma_e\cos\phi_e\sin\phi_e + \sigma_h\cos\phi_h\sin\phi_h}{\sigma_e cos^2\phi_e + \sigma_h cos^2\phi_h}. \tag{2.36}$$

Two additional equations are required to relate the Hall angles ϕ_e and ϕ_h to the carrier concentrations n_e and n_h. These are

$$\tan\phi_h = \frac{\sigma_h B_z}{n_h e}, \quad \tan\phi_e = -\frac{\sigma_e B_z}{n_e e}. \tag{2.37}$$

From above, the Hall coefficient is given by

$$R_H = \frac{\rho_{yx}}{B_z} = \frac{E\sin\phi}{JB_z}. \tag{2.38}$$

Making the necessary substitutions and working through the considerable algebra results in an expression for the Hall coefficient as a function of band conductivities, carrier concentrations, and the transverse magnetic field:

$$R_H = \frac{1}{e}\left[\frac{\frac{\sigma_h^2}{n_h} - \frac{\sigma_e^2}{n_e} + \frac{B_z^2\sigma_h^2\sigma_e^2(n_h - n_e)}{e^2 n_h^2 n_e^2}}{(\sigma_h + \sigma_e)^2 + \frac{B_z^2\sigma_h^2\sigma_e^2(n_h - n_e)^2}{e^2 n_h^2 n_e^2}}\right]. \tag{2.39}$$

For a compensated metal where n$_h$ equals n$_e$, (2.39) simplifies to

$$R_H = \frac{1}{ne}\left[\frac{\sigma_h - \sigma_e}{\sigma_h + \sigma_e}\right] = \rho(\mu_h - \mu_e) \tag{2.40}$$

where n is taken as the generic carrier concentration, mobility μ is defined as $e\tau/m$, and the resistivity ρ equals $1/(\sigma_h + \sigma_e)$. That is, the sign of the Hall coefficient of a compensated metal ultimately depends on the effective masses of electrons and holes within the two-band model in the relaxation-time approximation. The effective masses, of course, depend on the curvatures of the electron and hole Fermi surfaces. If electron and hole concentrations are unequal and the field is low, as in the experiments considered here, then (2.39) becomes

$$R_H = \frac{1}{e}\left[\frac{\frac{\sigma_h^2}{n_h} - \frac{\sigma_e^2}{n_e}}{(\sigma_h + \sigma_e)^2}\right] = \rho^2 e(n_h\mu_h^2 - n_e\mu_e^2). \tag{2.41}$$

This shows that relative concentrations, as well as mobilities, can determine the sign of the Hall coefficient.

2.5. Ettingshausen Effect and the Isothermal Hall Coefficient

Classified as a galvanomagnetic temperature gradient due to the interaction of transport current with an external magnetic field, the Ettingshausen effect, although relatively small, ensures that a Hall measurement will not be isothermal.[13,14] The following equation may be written for the temperature gradient that appears in a homogeneous, isotropic material with a x-directed current density and z-directed magnetic field, where P is the Ettingshausen coefficient

$$\boldsymbol{\nabla} T = P\boldsymbol{J}\; x\; \boldsymbol{B} = PJ_x B_z(-\hat{y}). \tag{2.42}$$

Figure 2.6 illustrates how opposite sides of the slab shown above are at different temperatures due to the Ettingshausen effect.

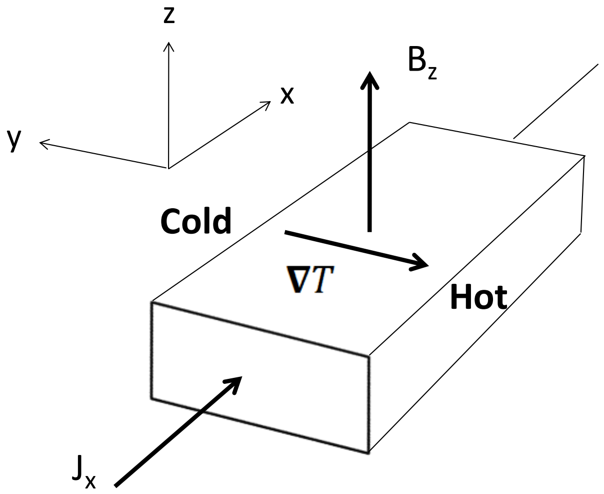

FIGURE 2.6. Illustration of the Ettingshausen temperature gradient due to transport current in a transverse magnetic field.

The Ettingshausen effect alters the Hall coefficient in the sense that an ideal Hall measurement would be isothermal, whereas a real Hall measurement is adiabatic. The relationship between the two Hall coefficients is given by

$$R_{Hi} = R_{Ha} - SP \tag{2.43}$$

where S is the Seebeck coefficient for the assumed homogeneous and isotropic material.[1,13] It will be shown in Chapter 3 that, at least for ruthenium, the Ettingshausen effect is negligible.

2.6. Van der Pauw Method

Van der Pauw showed in 1958 that the resistivity and Hall coefficient of a homogeneous sample of arbitrary shape may be measured subject to the following restrictions: contacts are on the circumference; contacts are sufficiently small; the sample has a uniform thickness; and the sample is simply connected (no holes).[15] For a sample with an arbitrary geometry such as shown in Figure 2.7, the key result is that the resistivity may be written as an average of two measured resistances that is modified by a function of the resistance ratio $f\left(R_{AB,CD}/R_{BC,DA}\right)$ which corrects for any difference in the resistances. Given a sample of thickness t, the resistivity at some temperature may be written in the van der Pauw notation as

$$\rho = \frac{\pi t}{ln\, 2}\left(\frac{R_{AB,CD} + R_{BC,DA}}{2}\right) f\left(\frac{R_{AB,CD}}{R_{BC,DA}}\right) \tag{2.44}$$

where $R_{AB,CD}$ is the resistance measured by dividing the potential difference (V_D - V_C) by current that goes into contact A and out contact B. A similar definition holds for $R_{BC,DA}$. The function f is defined from the transcendental equation

$$\frac{R_{AB,CD} - R_{BC,DA}}{R_{AB,CD} + R_{BC,DA}} = f \cosh^{-1}\left\{\frac{exp\left(\frac{\ln 2}{f}\right)}{2}\right\}. \tag{2.45}$$

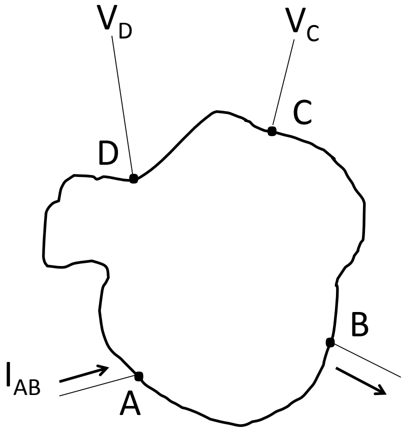

FIGURE 2.7. Illustration of a sample of arbitrary shape with electrical contacts on the boundary that may be used for resistivity and Hall measurements in the van der Pauw method.

---

[1] J. -P. Jan, *Solid State Physics*, 5, 1 (Academic, New York, 1957).

[2] G. T. Meaden, *Electrical Resistance of Metals* (Plenum, New York, 1965).

[3] C. M. Hurd, *The Hall Effect in Metals and Alloys* (Plenum, New York, 1972).

[4] W. Boas and J. K. Mackenzie, *Progress in Metal Physics*, 2 (Interscience, New York, 1950).

[5] L. Onsager, Phys. Rev. 37, 405, 1931.

[6] J. L. Nichols, J. Appl. Phys. 26, 470, 1955.

[7] W.D. Ryden, A.W. Lawson and C. C. Sartain, Phys. Rev. B 1, 1494, 1970.

[8] ASTM F76-86 (Reapproved 1996).

[9] M. A. Omar, *Elementary Solid State Physics* (Addison-Wesley, Reading, 1993).

[10] N. W. Ashcroft and N. D. Mermin, *Solid State Physics* (Thomson Learning, 1976).

[11] C. Kittel, *Introduction to Solid State Physics* (Wiley, New York, 2005).

[12] E. Kreyszig, *Advanced Engineering Mathematics* (Wiley, New York, 1967).

[13] I. S. Grigoriev and E. Z. Meilikhov, *Handbook of Physical Quantities* (CRC Press, 1997).

[14] S. W. Angrist, Scientific American, 205, 6, 124, 1961.

[15] L. J. van der Pauw, Philips Res. Repts. 13, 1, 1958.

Chapter 3

EXPERIMENTAL DETAILS

All transport measurements were made using an apparatus designed for four-point conductivity and Hall-effect measurements of thin films.[1] The apparatus, shown on the left in Figure 3.1, is one station of an ultrahigh-vacuum, deposition-and-analysis system in the Thin Film Synthesis, Processing and Characterization Laboratory at LASST.

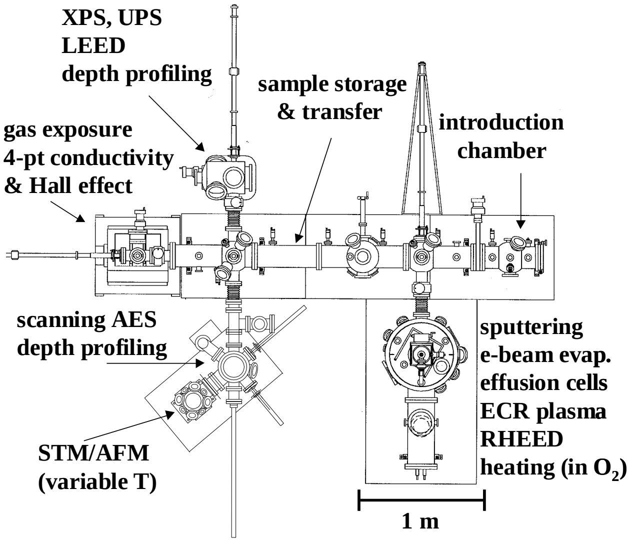

FIGURE 3.1. Ultrahigh-vacuum, thin-film-deposition, analysis and characterization system. Transport measurements were made in the “gas-exposure, 4-pt conductivity and Hall effect” station. (Reproduction of Fig. 1, reference 1)

3.1. Charge-Transport Measurement Apparatus

An elevation view of the conductivity-and-Hall-effect chamber is shown in Figure 3.2. Note that the electromagnet is a split-pair solenoid with a highly homogeneous magnetic field over the sample volume.

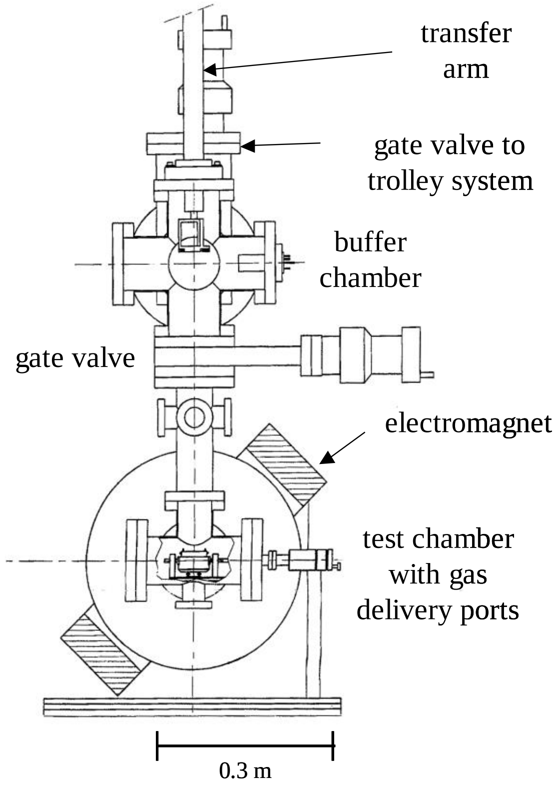

FIGURE 3.2. Elevation view of charge-transport measurement apparatus. Samples are located in the central field of the split-pair solenoid shown at the bottom. (Reproduction of Fig. 2, reference 1)

A photograph of the measurement fixture is shown in Figure 3.3. The docking stage has four gold-plated, spring-loaded Be-Cu pins that make electrical contact with the film under measurement. There are also two spring-loaded thermocouples (S and K-types) that make contact with the film substrate. Film temperature is controlled by supplying power to a movable resistance heater that is controlled by the S-type thermocouple.

An elevation-view assembly of the measurement fixture is shown in Figure 3.4. This is the key component for resistivity and Hall measurements. The four pins contact the test specimen on its periphery in accordance with the van der Pauw geometry requirements. Van der Pauw and Hall measurements are distinguished, in part, by the different pin selections for currents and voltages as explained below.

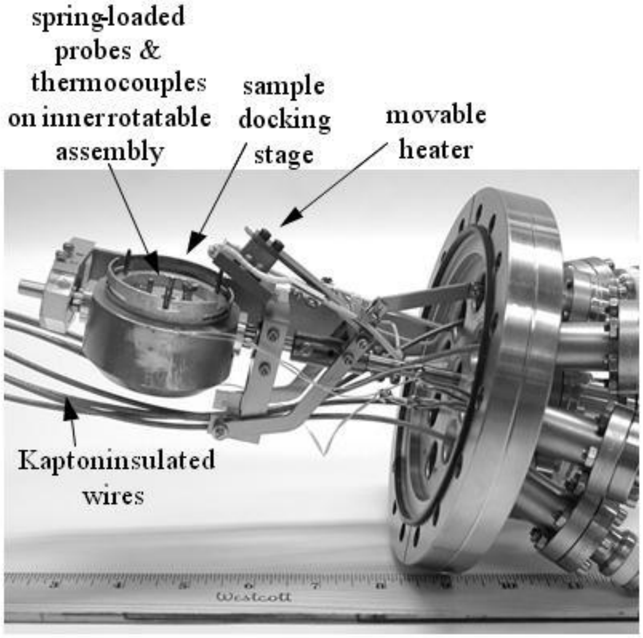

FIGURE 3.3. Measurement fixture showing the docking stage and movable heater. The docking stage contains four contact pins and two thermocouples that touch the sample, which is loaded face-down on the docking stage. (Reproduction of Fig. 3, reference 1)

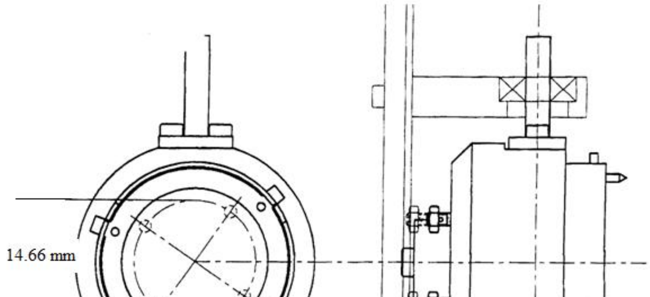

FIGURE 3.4. Docking stage showing the four contact pins hidden under the carrier in the left view. Contact pins lie on a circle of 14.66 mm diameter and are guided by Vespel SP-21 top-hat washers rated to 350 °C. (Reproduction of DCA Instruments drawing[4])

An example of a sample carrier (stainless steel or tantalum) holding a thin film deposited on a sapphire substrate is shown in Figure 3.5. The film is deposited through a mask to define the 17 mm diameter area that is contacted by the four spring-loaded probes.

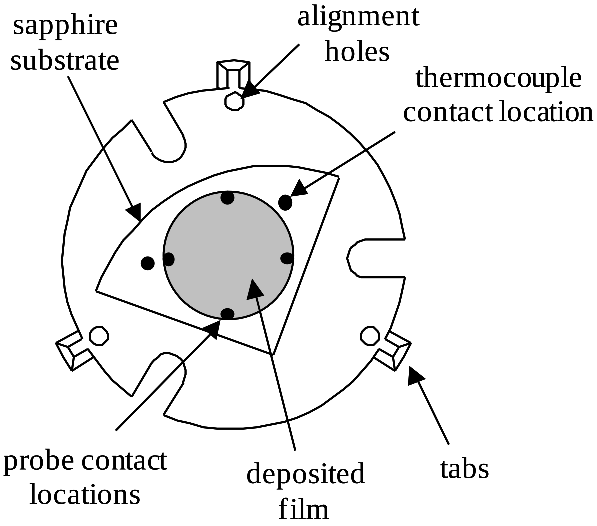

FIGURE 3.5. Example of a sample carrier holding a thin film on a sapphire substrate. (Reproduction of Fig. 4, reference 1)

Figure 3.6 shows a schematic of the overall measurement system. Electrical measurements were acquired under computer control in a series of programs written in LabView.[2] Both van der Pauw and Hall measurements were based on averages obtained by selecting different pairs of pins for current and voltage measurements. Switching among pins was done by mechanical reed switches contained in the switch box.

3.2. Four-Point Resistivity Measurement

The van der Pauw technique is a four-point measurement of dc resistivity (conductivity) where a fixed current flows through adjacent contacts and a potential difference is measured across opposite contacts as pointed out in Chapter 2. Figure 3.7 illustrates the technique, where the excitation is from a controlled current source with a 105 V compliance limit and the response is measured by a high-input-impedance voltmeter.

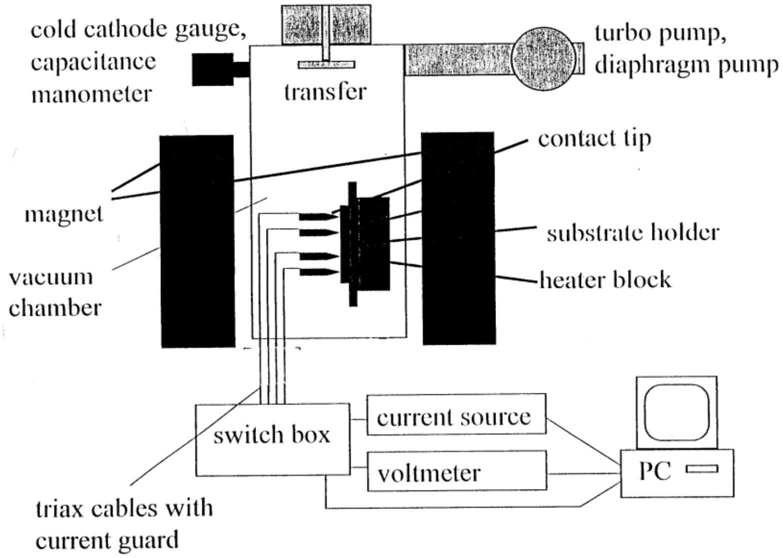

FIGURE 3.6. Schematic of measurement system. (Reproduction from reference 3)

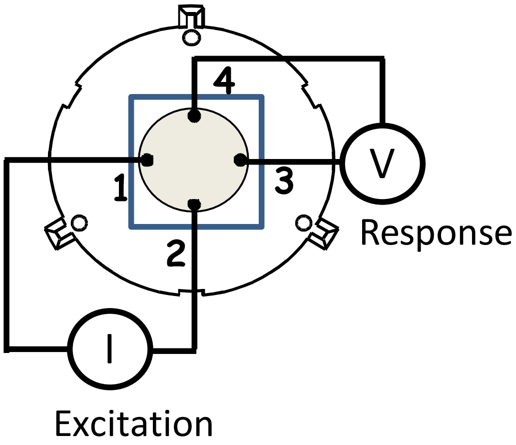

FIGURE 3.7. Illustration of the measurement of resistivity in the van der Pauw geometry. The film is shown as the central circle and the substrate as the central square. Measurement of $V_{12,34}$ is shown.

Note that contacts are labeled consecutively 1 - 4 in counter-clockwise order around the film periphery. The equations for resistivity are written below in the nomenclature of ASTM F76 - 86, where $V_{12,34}$ refers to the potential difference $V_3 - V_4$ between contacts 3 and 4 when current enters contact 1 and exits contact 2.[5] (This convention differs slightly from the original van der Pauw convention of Chapter 2.) Resistivity is found as an arithmetic average of two resistivities, called ρ_A and ρ_B, at a fixed temperature as shown in equation (3.1). That is,

$$\rho = \frac{\rho_A + \rho_B}{2}. \tag{3.1}$$

The individual resistivities are based on odd functions of an average resistance as stated in Chapter 2. For example, in equation (3.2) an average resistance would be $\left(V_{21,34} + V_{32,41}\right)/2I$, with the additional two negative terms included to make the function odd. The two resistivities are

$$\rho_A = \frac{1.1331 f_A t}{I}\left[V_{21,34} - V_{12,34} + V_{32,41} - V_{23,41}\right] \tag{3.2}$$

$$\rho_B = \frac{1.1331 f_B t}{I}\left[V_{43,12} - V_{34,12} + V_{14,23} - V_{41,23}\right] \tag{3.3}$$

where the units of resistivity are Ω cm. One of the difficulties of the F76 - 86 method is the use of hybrid “laboratory” units, which are neither SI nor cgs units. In the above equations, the constant 1.1331 is an approximation of $\pi/4ln2$, potentials are in volts, specimen thickness t is in centimeters, current I is in amperes, and the geometrical factors f_A are f_B are functions of resistance ratios (or voltage ratios), given by either Q_A or Q_B:

$$Q_A = \frac{R_{21,34} - R_{12,34}}{R_{32,41} - R_{23,41}} = \frac{V_{21,34} - V_{12,34}}{V_{32,41} - V_{23,41}} \tag{3.4}$$

$$Q_{\boldsymbol{B}} = \frac{R_{43,12} - R_{34,12}}{R_{14,23} - R_{41,23}} = \frac{V_{43,12} - V_{34,12}}{V_{14,23} - V_{41,23}}. \tag{3.5}$$

The Q's may be thought of as quality factors, where a Q of 1 represents an ideal measurement on a specimen with pin contacts on the periphery. As shown in ASTM F76 - 86, Figure 5, the geometrical factor f is approximately equal to 1 for Q's below about 1.2 and falls below 1 for higher values of Q. The equation relating Q and f is a non-algebraic, transcendental equation similar to (2.45) and is written as

$$\frac{Q-1}{Q+1} = \frac{f}{0.693}\cosh^{-1}\left\{\frac{1}{2}exp\left(\frac{0.693}{f}\right)\right\}. \tag{3.6}$$

3.3. Hall Coefficient Measurement

The measurement of the Hall coefficient is made with the sample in the configuration shown in Figure 3.8.

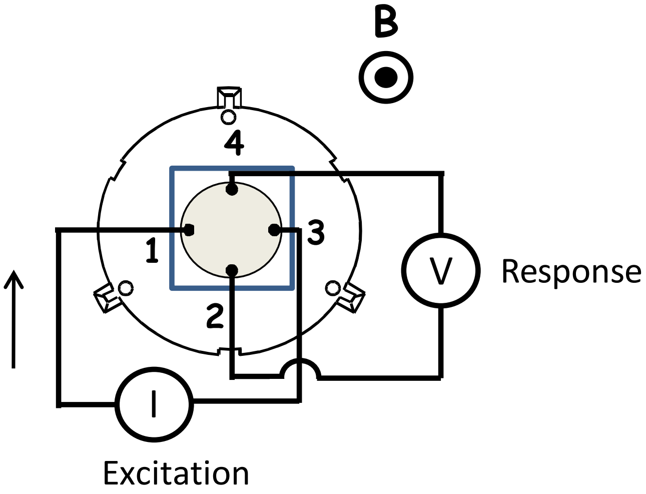

FIGURE 3.8. Illustration of the measurement of the Hall coefficient with the magnetic field B pointing out of the page.

As stated in Chapter 2, the Hall coefficient is defined as an off-diagonal resistivity per unit magnetic field given by ρ_{yx}/B_z. In the nomenclature of ASTM F76 - 86, the Hall coefficient is the average of two Hall coefficients at a fixed temperature and is defined as

$$R_H = \frac{R_{HC} + R_{HD}}{2} \tag{3.7}$$

$$R_{HC} = \frac{2.50\ \times\ 10^7 t}{BI}\left[V_{31,42}(+B) - V_{13,42}(+B) + V_{13,42}(-B) - V_{31,42}(-B)\right] \tag{3.8}$$

$$R_{HD} = \frac{2.50\ \times\ 10^7 t}{BI}\left[V_{42,13}(+B) - V_{24,13}(+B) + V_{24,13}(-B) - V_{42,13}(-B)\right] \tag{3.9}$$

where the units of R_H are cm^3/C and flux density B is given in units of gauss. In SI units, R_H could also be given in units of (Ω m/T) to reflect the character of a resistivity divided by field.

3.4. Algorithm to Minimize Baseline Drift

Background noise can make the measurement of low-level signals difficult, as is the case for Hall measurements of thin films. In particular, the baseline potential, defined as the voltage seen across measurement pins at zero current, should be zero in an ideal situation. However, the baseline potential was often observed to drift by one or two microvolts per second as witnessed by plots of baseline voltage as a function of time. The amount of baseline drift varied from day to day and was possibly due to thermal or contact potentials or to interference from the operation of the many nearby electrical devices in the Thin Film Laboratory. Since transport measurements of thin films often involve signal levels on the same order of magnitude as the drift, the drift rate represented a significant noise problem.

In order to alleviate the problem of data scatter introduced by the drift, an algorithm was written and incorporated into the LabView computer programs that were used for data acquisition. The idea behind the algorithm is to measure the baseline before turning on the excitation current, to measure the signal with the current on, and to re-measure the baseline after turning the current off. The three measurements are done rapidly and the initial and final baseline voltages are compared to a specified drift-voltage tolerance. If the baseline difference is within the tolerance, meaning an acceptable drift, then the mean baseline can be subtracted from the signal yielding a result with most of the drift error removed.

The test for baseline drift was defined as the absolute value of the difference in average baseline potentials compared to a specified drift tolerance:

$$\left|V_{BLi} - V_{BLf}\right| < V_{tol} \tag{3.10}$$

where V_{BLi} and V_{BLf} are the initial and final average baseline voltages and V_{tol} is the specified drift tolerance. If this condition was satisfied, then a corrected voltage was given as the apparent average signal V minus the mean of the two average baseline voltages:

$$V_c = V - \left(\frac{V_{BLi} + V_{BLf}}{2}\right) \tag{3.11}$$

where V_c is the corrected, or true, signal. A flow chart of the algorithm is shown in Figure 3.9 where the input quantity, n, represents the number of samples taken for each signal (n for V_{BLi}, n for V, and n for V_{BLf}) before the average of the two baselines are compared. With regard to Hall measurements, where baseline drift caused significant problems, it was found empirically that the most reliable results came from limiting n to a small value (n = 2) and then iterating the entire process in another programming loop, not shown here, 50 times for a total of 100 data points per measurement. Note that the sampling period was 25 ms.

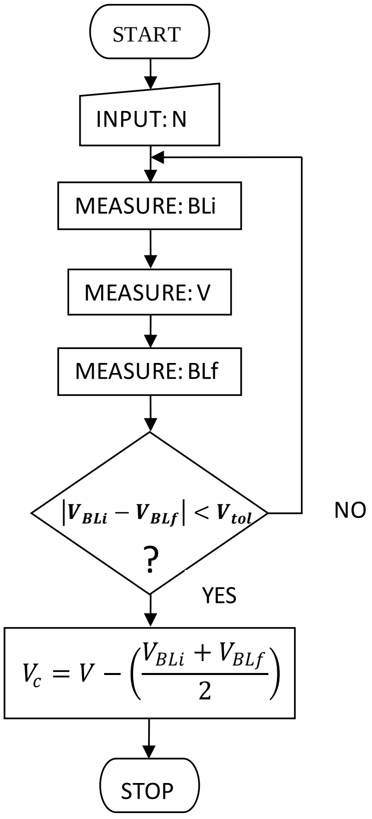

FIGURE 3.9. Flow chart for algorithm to minimize baseline drift. The signals V_{BLi}, V, and V_{BLf} are each measured n times and averaged over the number of measurements. The average baseline voltages are then compared to the specified voltage tolerance.

3.5. Sample Geometry

Most of the films were grown on GE Type 124 fused quartz substrates measuring 25 x 25 x 1.6 mm (1 x 1 x 0.0625 inches), although some Ru films were grown on glass microscope slides (see Chapter 4). The substrates were plasma cleaned prior to deposition. Circular films were deposited through 17 mm diameter masks to match the required van der Pauw geometry, which is shown in Figure 3.10.

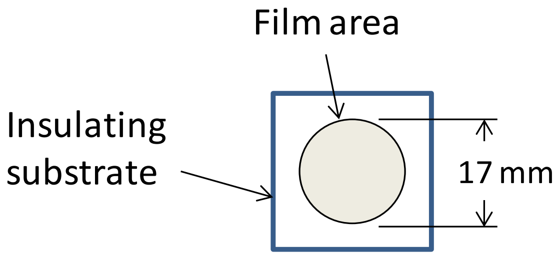

FIGURE 3.10. Geometry of thin-film samples used in transport measurements.

3.6. Thin-Film Deposition Techniques

The Ru and RuO_2 films were grown using several different deposition techniques and geometries. The vast majority of the films were grown by reactive rf magnetron sputtering, but a few were grown by plasma-assisted electron-beam evaporation. The first sputtering technique was normal-incidence dc and rf magnetron sputtering where the center of the target and center of the substrate shared the same vertical centerline. The second technique was confocal rf magnetron sputtering where the target was offset from the substrate and tilted toward the substrate but with the centerline of the target not passing through the center of the substrate.[6] The third technique was glancing-angle dc magnetron sputtering, where the substrate was above the target as in normal-incidence sputtering, but was tilted so that the particle beam arrived at the substrate at a relatively small angle forming the so-called glancing-angle deposition (GLAD) geometry, which gives rise to nanorod-structured films.[7] The three different sputtering configurations are illustrated in Figure 3.11. The e-beam deposition system is shown in Figure 3.12. Pure Ru films were deposited by rf sputtering in an argon plasma or by e-beam evaporation in a high vacuum. RuO_2 films were grown either by reactive rf magnetron sputtering using an argon-oxygen mixture or by electron-beam evaporation of Ru in the presence of an electron-cyclotron-resonance (ECR) oxygen plasma.[7-9] Deposition parameters for the RuO_2 film parametric study of Chapter 5 are given in Appendix A and the parameters for the other films are given in Chapters 4 and 7.

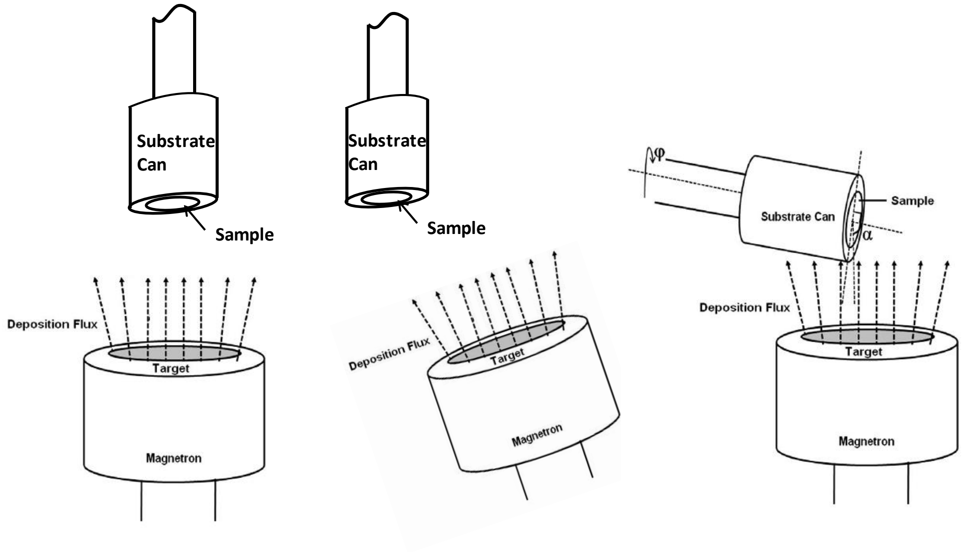

Normal incidence **Confocal** **Glancing angle**

FIGURE 3.11. Illustration of the three magnetron sputtering geometries used to grow films. In addition to the angle-of-incidence variations shown here, factors that influenced film growth were substrate temperature, substrate rotation rate, substrate roughness, adatom mobility, and deposition-chamber pressure.

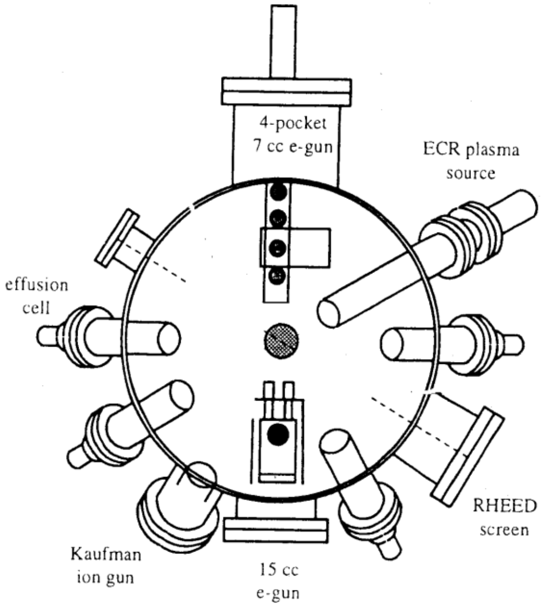

FIGURE 3.12. Film deposition chamber with a four-pocket e-gun and ECR plasma source at the 12 and 2 o'clock positions.[10]

3.7. Sources of Error and System Calibration

Sources of error in the transport measurements are outlined in reference 11. Uncertainty in film thickness was a leading source of error, but other sources such as baseline drift, instrument calibration, contact-pin placement on the sample boundary, and temperature measurement and control were contributing factors. However, the overall performance of the resistivity and Hall-effect apparatus was checked against reference materials and found to be good. That is, system calibration was often checked before and after measurements using an unannealed gold thin film and occasionally n- and p-type silicon wafers as reference materials. An additional one-time check made use of a certified commercial silicon standard from MMR Technologies (provided by Dr. J. Gu of Carnegie Mellon University). Without correcting for temperature, the system returned a room-temperature resistivity within about 3 percent and a room-temperature Hall coefficient within about 1 percent of the values specified in the MMR standard. See Appendix B for more information on calibration.

3.8. Procedure and Schematic for Gas Tests

Transport tests in gas atmospheres were carried out at zero flow in the following manner. First, the film sample was loaded into the test fixture and the chamber evacuated to approximately 10^{-5} to 10^{-6} torr and held at this level for a few hours. Next, the valves on the vacuum lines were closed and the chamber filled to typically 4 torr with either O_2 or CO. To switch gases, the chamber was evacuated again to around 10^{-5} torr and then filled immediately with the other gas. Gas switching took about 20 to 30 minutes, depending on the inlet flow rate, which was difficult to control precisely. The Eurotherm heater controller was unable to maintain a constant temperature during gas switching and the sample temperature often rose above and fell below the set point by about ± 30 °C. A schematic of the gas-control system is shown in Figure 3.13.

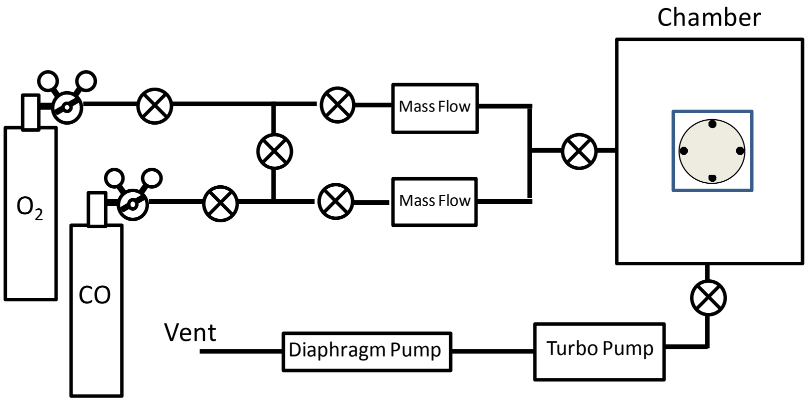

FIGURE 3.13. Schematic of gas-control system.

3.9. X-Ray Diffraction Measurements

X-ray diffraction measurements were made using a PANalytical X'Pert PRO material research diffractometer with copper K-alpha radiation. Most of the measurements presented in this document are grazing incidence scans, but θ/2θ and in-plane scans (grazing-incidence, grazing-exit) are also featured. In addition, thicknesses of many planar films were determined by x-ray reflectivity in conjunction with profilometer measurements. A photograph of the diffractometer defining the measurement angles and optics is presented in Figure 3.14. A typical grazing scan employed an x-ray mirror and divergence slits on the incident side, and a parallel-plate collimator, Soller slits, and proportional-counter detector on the receiving side.

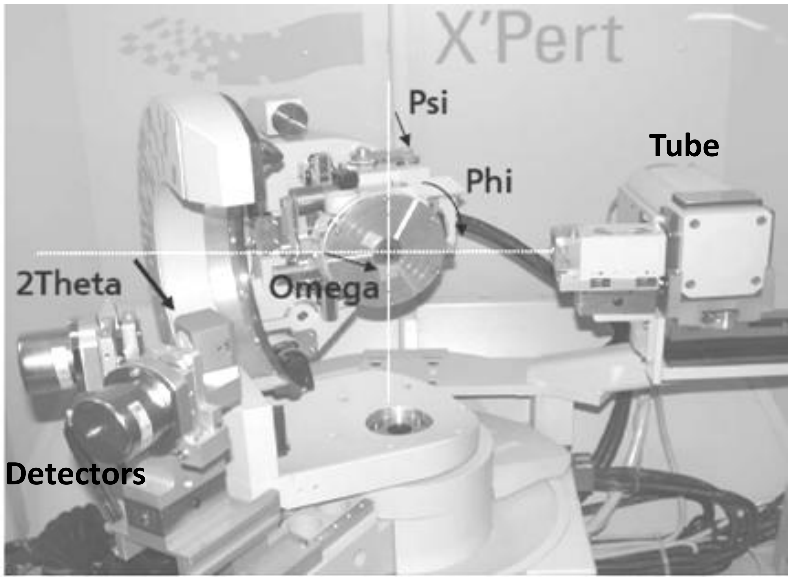

FIGURE 3.14. Photograph of the PANalytical materials research diffractometer defining the measurement angles 2theta, omega, psi, and phi. The x-ray tube and incident optics are shown on the right-hand side, the goniometer with the sample in the center, and the receiving optics and detectors on the left.

3.10. XPS Film Composition Measurement

The composition of the surface of one RuO_2 film (see Figure 6.8) was estimated by x-ray photoelectron spectroscopy (XPS) using a Specs MCD hemispherical analyzer with a 10 eV pass energy, a magnesium x-ray source anode, and CasaXPS analysis software. Signal intensities are proportional to element concentrations, and the estimate of composition was based on the areas of the O-1s and Ru-3d peaks and utilized sensitivity factors of O/Ru equal to 0.711/3.696.

---

[1] S. C. Moulzolf, D. J. Frankel and R. J. Lad, Rev. Sci. Instrum. 73, 6, 2325 (2002).

[2] LABVIEW, National Instruments Corporation.

[3] S. Ding, LASST Internal Memo (2000).

[4] DCA Instruments Corporation.

[5] American Society for Testing and Materials, ASTM F 76 – 86 (1996).

[6] AJA International, Inc.

[7] M. Ohring, *Material Science of Thin Films* (Academic, San Diego, 2002).

[8] J. Asmussen, R. Fritz, and L. Mahoney, Rev. Sci. Instrum. 61, 282 (1990).

[9] J. Asmussen, T. A. Grotjohn, P. Mak, and M. A. Perrin, IEEE Trans. Plas. Sci. 25, 6, 1196 (1997).

[10] S. C. Moulzolf, PhD Thesis, The University of Maine (1999).

[11] M. M. Steeves, PHY 510 Graduate Laboratory Report, The University of Maine (2007).

Chapter 4

RUTHENIUM THIN FILMS

4.1. Chapter Abstract

Resistivities and Hall coefficients of unannealed flat and nanorod-structured Ru thin films were investigated from 295 to 600 K. Resistivities typically decreased upon first heating due to defect annealing, but Hall coefficients were found to be independent of temperature and defect content. The temperature independence of the Hall coefficient above cryogenic temperatures was consistent with most metals. The error in the Hall coefficient due to the Ettingshausen effect was shown to be negligible. Although resistivities and Hall coefficients of planar films are determined by a nominal film thickness, it was found that resistivities of nanorod-structured films were dominated by an ultra-thin polycrystalline layer at the film-substrate interface and Hall coefficients appeared to depend on an effective thickness determined by nanorod size and spacing.

4.2. Purpose

As stated in Chapter 1, ruthenium is a p-type transition metal with ten possible oxidation states,[1] a hexagonal-close-packed structure (hcp), a resistivity[2] of 7.4 $\mu\Omega$ cm and a Hall coefficient[3, 4] of +22 x 10^{-5} cm^3/C at 295 K for bulk polycrystalline samples. Resistivity versus temperature has been reported for Ru thin films grown by metal-organic chemical vapor deposition.[5, 6] However, to the best of our knowledge, no studies prior to this one have been done to determine the influence of defects and structure on the resistivities of Ru films,[7, 8] and no data exist for the Hall coefficients of Ru thin films grown by any technique. In this study, charge transport measurements of flat and nanorod-structured polycrystalline Ru thin films grown by physical vapor deposition are reported and the effect of non-slab geometry on the resistivities and Hall coefficients of nanorod-structured thin films is considered.

4.3. Ru Film Deposition

A 252 nm thick flat film was deposited at 0.5 Å/s through a 17 mm circular mask onto a glass substrate (Fisher Scientific microscope slide) by conventional normal-incidence, RF magnetron sputtering of a 76 mm diameter, 99.95 % Ru target at 270 W in an argon-plasma deposition system. Base and deposition pressures were 0.7 µtorr and 19 mtorr and the substrate temperature was 18 °C. The target-to-substrate distance was 20 cm with no substrate rotation. RMS roughness was 18 Å over 100 μm^2 as determined by atomic force microscopy. For contrast, a 79 nm nominal thickness (SEM measurement) nanorod-structured film was grown by glancing angle deposition (GLAD) at 18 °C through the same mask at 0.5 Å/s onto a fused-silica substrate (GE type 124) with 5 rpm rotation using the same Ru target in the same chamber, but with 80 W DC magnetron sputtering at an angle of 80° from the substrate normal. Base and deposition pressures were 0.2 µtorr and 3 mtorr and the target-to-substrate distance was 11 cm. Neither film received post-deposition heat treatment prior to transport-property measurements. Scanning electron microscope (SEM) elevation-view images of the two films are shown in Figure 4.1. (See Figure 4.3 for plan-view images.)

With reference to Chapter 3, transport properties were measured in high vacuum using the four-point van der Pauw and Hall-effect apparatus.[9] System calibration was checked before and after measurements, which followed the methods in ASTM F76 - 86.[10]

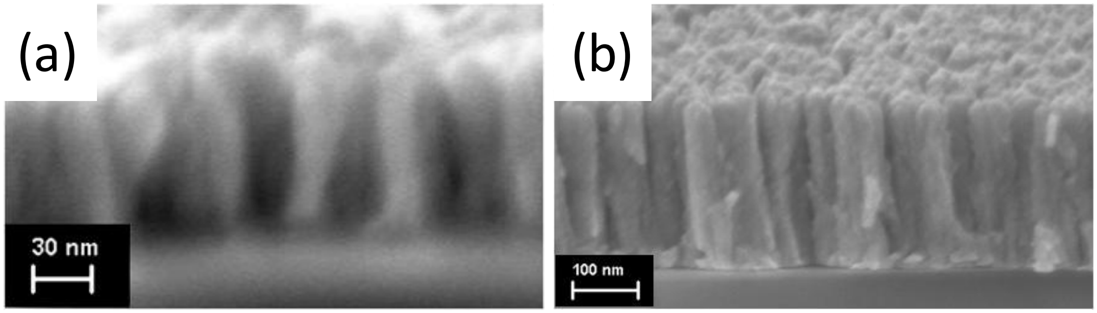

FIGURE 4.1. SEM elevation-views of Ru (a) nanorod-structured and (b) flat films.

4.4. Resistivity of Unannealed Ru Thin Films

Figure 4.2 plots resistivity based on nominal film thicknesses as a function of temperature comparing several heating cycles of the as-deposited flat and nanorod films. The fall in resistivity on first heating in both films is due to the removal of defects such as vacancies and interstitials by annealing.[11,12] Upon subsequent heating and cooling, the films exhibit reversible positive slopes characteristic of metals described by Matthiessen's rule, which states that the total resistivity ρ is the sum of a temperature-independent term ρ_0 due to impurities, other defects, and strain, and a temperature-dependent intrinsic term ρ_i due primarily to scattering of electrons by phonons.[2]

On subsequent heating from 295 K, neither film showed the slope predicted by the Gruneisen-Bloch equation, a universal curve fit for metals, where θ_R = 364 K (see below) was taken as the 'resistivity characteristic temperature' for polycrystalline Ru, which is similar in order to the Debye temperature.[2] The shallowness of the observed slopes suggests that the removal of defects by annealing is incomplete in both films. It is inferred that the defect content of the nanorod film is higher than that of the flat film because the difference from the ideal slope is greater in the nanorod case (68 % versus a

46 % difference). Note that although Ru is magnetoresistive, the test fields were too low to see any effect.[14]

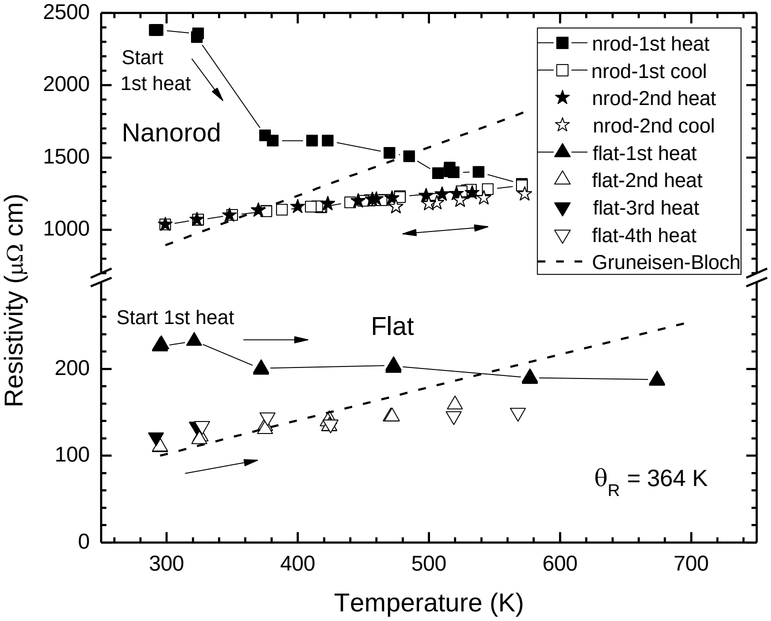

FIGURE 4.2. Resistivity as a function of temperature comparing flat and nanorod-structured Ru thin films. The legend defines the heating sequence. Dashed lines are for ideal bulk polycrystals using the Gruneisen-Bloch equation with a resistivity characteristic temperature of 364 K. Arrows indicate the test direction.

The characteristic temperature θ_R was estimated by the Nichols equation,[13,2] which states that the average resistivity of a randomly oriented, polycrystalline hcp metal is equal to $\rho_r = 2\rho_a/3 + \rho_c/3$, where ρ_a is the resistivity perpendicular to and ρ_c the resistivity parallel to the c-axis of a single crystal. The Gruneisen-Bloch equation[2] is

$$\rho = \frac{\kappa_{GB} T}{\theta_R^2} G\left(\frac{\theta_R}{T}\right) \tag{4.1}$$

where κ_{GB} is taken as a constant related to electron-phonon interaction, T is temperature, and $G(\theta_R/T)$ is the Gruneisen function. Substituting this expression for each resistivity in the Nichols equation (ρ_{iTn}, n = r, a, c) and noting that single-crystal θ_R's in the a- and c-directions are $\theta_{Ra} \approx 350$ and $\theta_{Rc} \approx 400$ K near room temperature[15] allows an overall polycrystalline $\theta_R \approx 364$ K to be estimated, since the Gruneisen function is tabulated.[2]

To clarify the steps in the procedure for finding the resistivity characteristic temperature, (2.10) is written using the Gruneisen-Bloch equation as

$$\frac{G_R\left(\frac{\theta_R}{T}\right)}{\theta_R^2} = \frac{2G_a\left(\frac{\theta_{Ra}}{T}\right)}{3\theta_{Ra}^2} + \frac{G_c\left(\frac{\theta_{Rc}}{T}\right)}{3\theta_{Rc}^2}. \tag{4.2}$$

From Volkenshteyn, Figure 3, the values of θ_{Ra} and θ_{Rc} may be estimated as $\theta_{Ra} = 350\ K$ at 273 K and $\theta_{Rc} = 400\ K$ at 293 K.[15] For convenience, the value of T was chosen to be 400 K. Then from Meaden, Table VII, it is seen that G(0.875) = 0.9579 and G(1) = 0.9465, using the tabulated values of the Gruneisen function.[2] From (4.2), it follows that

$$G_R\left(\frac{\theta_R}{400}\right) = 7.185x10^{-6}\theta_R^2\,. \tag{4.3}$$

The intersection of the curves represented by the left and right hand sides of (4.3) yields a resistivity characteristic temperature of $\theta_R \approx 364\ K$.

Figure 4.3 shows SEM plan-view images of both films. The resistivity of the nanorod film, based on a 79 nm thickness, is an order of magnitude greater than that of the flat film, which in turn is an order of magnitude greater than that of an ideal polycrystalline bulk sample (not shown - see Table 1.1). It is assumed that the resistivities of both films, which were grown by similar processes, should be roughly equal. The higher nanorod-film resistivity is likely to be due to using a nominal rather than an effective film thickness in the slab model for resistivity calculation. The structures of GLAD films often consist of an ultra-thin polycrystalline base layer near the film-substrate interface upon which nanorods grow.[16] Two possible models of effective thickness include one with this base layer plus nanorods and another with the base layer only. When the nanorods are included, the film can be modeled as an inhomogeneous conductor[17] made of square columns of equal height periodically arranged[18] on an ultra-thin, flat, simply-connected base as shown in Figure 4.3. The resistance of the film may be estimated by assuming that conducting cross-sectional areas perpendicular to the transport current include the full rod heights and that rod and base defect densities are similar.

The goal is to estimate an effective thickness t_{1n} of a nanorod film relative to that of a flat film of the same nominal thickness t_1. To do so, it is assumed that the nanorod film is square and that $l_1 \gg l_2$ and $t_1 \gg t_2$. Then the total resistance may be written as the sum of two resistances: the first due to a small slab that does not contain a nanorod and has dimensions of $l_2\ x\ t_2\ x\ (l_1 + l_2)$ and the second due to two joined slabs, one small and one large, of dimensions $l_1\ x\ l_1\ x\ t_1$and $l_1\ x\ l_2\ x\ t_2$. Since the rod and base defect densities are assumed to be similar, the resistivity is taken as a constant.

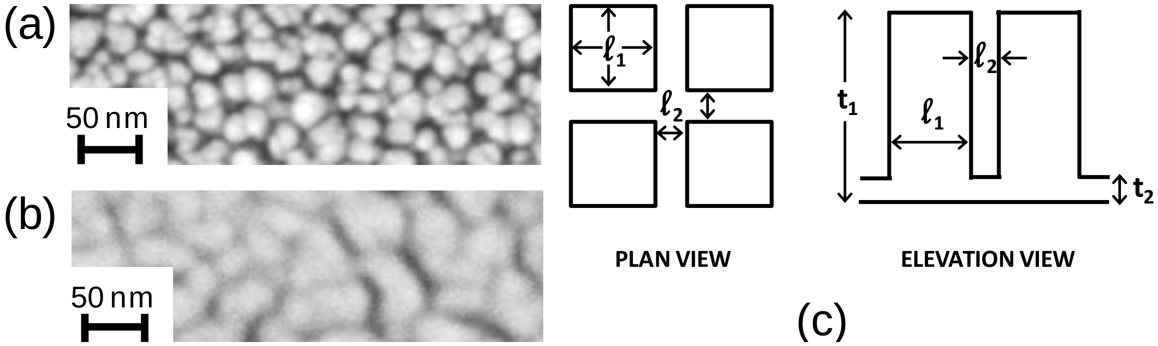

FIGURE 4.3. SEM plan-view images of Ru (a) nanorod-structured and (b) flat films. (c) Geometric model of a nanorod-structured film showing parameters to estimate effective film thickness.

The total resistance, written in terms of an equivalent thickness, is set equal to the sum of the two slab resistances:

$$R_{total} = \frac{\rho(l_1 + l_2)}{t_{1n}(l_1 + l_2)} = \frac{\rho l_2}{t_2(l_1 + l_2)} + \frac{\rho l_1}{t_1 l_1 + t_2 l_2} \quad (4.4)$$

Subject to the stated assumptions, equation (4.4) shows that the effective thickness t_{1n} of a nanorod film relative to that of a flat film of the same nominal thickness t_1 is decreased by a factor based on the product of two ratios

$$t_{1n} \approx t_1 \left[1 + \left(\frac{t_1}{t_2}\right)\left(\frac{l_2}{l_1}\right)\right]^{-1}. \quad (4.5)$$

From SEM images, the nanorod film dimensions are: $t_1 \approx 79$, $t_2 \approx 12$, $l_1 \approx 24$ and $l_2 \approx 10$ nm. These dimensions yield $t_{1n} \approx 0.27\, t_1$, which reduces the apparent nanorod-film resistivity by a factor of three. Considering that tunneling and thermionic emission[2] between nanorods spaced at $l_2 \approx 10$ nm are likely to be negligible, charge transport through the base layer alone with an effective thickness t_2 may be expected to dominate. When the 12 nm base layer is taken as the effective thickness, the flat and nanorod film resistivities are nearly equal. Any remaining difference in resistivities may be due to relative defect concentrations, discontinuity of the nanorod base layer, or perhaps to its thickness, although boundary scattering in ultra-thin films becomes important only at cryogenic temperatures.[11, 19]

4.5. Ettingshausen Effect

From Chapter 2, the measured adiabatic Hall coefficient R_{Ha} can be written in terms of the desired isothermal Hall coefficient R_{Hi} and the product of the Seebeck S and Ettingshausen P coefficients as[20]

$$R_{Hi} = R_{Ha} - SP \quad (4.6)$$

The Ettingshausen coefficient at temperature T may be written alternatively as[21]

$$P = \frac{TN}{\kappa} \tag{4.7}$$

where N is the Nernst coefficient and κ the thermal conductivity. The Nernst coefficient of polycrystalline Ru[22] falls monotonically from 6 to 2.5 x 10^{-9} m^2/K·s from 150 to 650 K while the thermal conductivity[23] is essentially constant at 104 W/m·K. An estimate at 300 K from (4.7) yields P ≈ 10^{-8} K m^3/J. Taking the Seebeck coefficient[22] as S ≈ -1 μV/K makes the product SP ≈ -10^{-8} cm^3/C. Since Hall coefficients for Ru are on the order of 10^{-4} cm^3/C, approximating R_{Hi} by R_{Ha} yields an error of about one part in ten thousand.

4.6. Hall Coefficient

The Nichols equation[2, 13] is assumed to hold for the Hall coefficient, because R_H is defined as an off-diagonal tensor-resistivity component per unit field (ρ_{yx}/B_z).[4] This yields an estimate of R_H for T ≥ 295 K of 13.1 x 10^{-5} cm^3/C, based on the low-field, single-crystal values[15] of R_{Ha} = 10.8 and R_{Hc} = 17.7 x 10^{-5} cm^3/C (a, c-directions). That is, the low-field Hall coefficient of ideal polycrystalline Ru should lie between the lower and upper bounds of R_{Ha} and R_{Hc}.

Figure 4.4 plots the Hall coefficient as a function of temperature for the flat and nanorod films using nominal thicknesses. Data were taken in the low-field limit, where the product of electron-cyclotron frequency and scattering relaxation time is much less than one ($\omega_c\tau << 1$).[4] While resistivity depends on temperature, the Hall coefficient appears to be independent of temperature in the range from 295 to 600 K. This is consistent with the Volkenshteyn data[15] that show less than 30 % variation in $R_{Ha,c}$ from 100 to 300 K.[15] The positive sign of R_H indicates that ruthenium, a compensated metal[4, 14] with equal electron and hole concentrations, has higher-mobility holes as the dominant charge carriers. With the excitation of all acoustic modes near or above Debye temperature, there is a single relaxation time and the ratio of mobilities and effective masses from the two-band model is $\mu_e/\mu_h \approx m_h/m_e \approx 0.3$.[15] The carrier concentration for the flat film follows as ≈ 4 x 10^{22} cm^{-3} and hole mobility at 300 K as ≈ 1 cm^2/Vs.

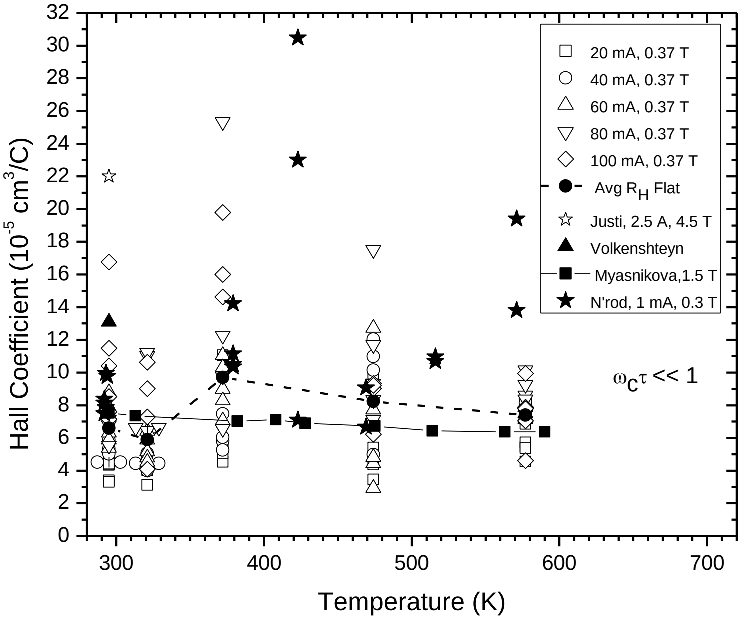

FIGURE 4.4. Hall coefficient as a function of temperature comparing flat and nanorod-structured Ru thin films to bulk data from Justi[3], Volkenshteyn[15] and Myasnikova.[21, 24] The legend lists test conditions with current as a parameter in flat-film measurements. Data were taken in the low-field condition with each point being an average of 16 measurements for the flat and 100 measurements for the nanorod films. A nominal film thickness of 79 nm was used to calculate R_H for the nanorod film.

The statistical means of the flat-film data at each temperature are shown by solid circles in Figure 4.4, which are connected by a dashed line. These are seen to lie within 30 % of data from Myasnikova for a polycrystalline Ru plate (99.8 % purity) measuring 10 x 5 x 1 mm and tested in fields up to 1.5 T.[21,24] The mean at 295 K is approximately a factor of three below the Justi[3] result of 22 x 10^{-5} cm^3/C, which is an average of 25 measurements at 2 to 2.9 A in a 4.47 T field at room temperature on a sintered powder sample (99.99 % purity, 6 % porosity) measuring 2.21 x 2.19 x 49.75 mm. The point labeled Volkenshteyn[15] represents an estimate of the Hall coefficient for an ideal random polycrystalline sample applying the Nichols equation.[2, 13] Based on the single-crystal Hall coefficients,[15] the average flat-film data of this study and the Myasnikova data[22] appear to be low, possibly due to impurity content, while the Justi[3] data appear to be high. Note that the current densities for the continuous film were 470 to 2340 A/cm^2 compared to 40 to 60 A/cm^2 for Justi (100 is typical for R_H measurements of bulk samples).[4]

The Hall coefficients of the nanorod-structured film in Figure 4.4 were calculated using a 79 nm nominal thickness, but effective film thickness also plays a key role in the determination of R_H in non-slab geometries.[10] Three possible models of effective thickness include using either the nominal thickness as in Fig. 4.4, the ultra-thin polycrystalline base-layer thickness, or the nominal thickness modified by geometry[17] (Fig. 4.3c). To account for geometry, one can assume a uniform transport-current density, a linear Hall potential across the sample, and the applicability of the rule of mixtures for the geometric model of Hall coefficients. On this basis, the effective thickness of a nanorod film t_{1n} relative to a flat film of the same nominal thickness t_1 is reduced by a factor that depends only on the rod size and spacing: $t_{1n} \approx t_1(1 + l_2/l_1)^{-2}$. (The derivation of this relationship, equation (4.21), will be given below.) If the flat-film and Myasnikova bulk data are taken to define an expected range for the nanorod-film data, then the best fit for the average nanorod-film Hall coefficients as a function of temperature is obtained from an effective thickness calculated by equation (4.21), which yields $t_{1n} \approx t_1/2 \approx 39$ nm. In contrast, applying the base-layer thickness to the R_H calculation yields roughly 2 x 10^{-5} cm^3/C from 295 to 600 K, which is too low for Ru based on the Volkenshteyn[15] and Justi[3] data.

The average nanorod-film, flat-film, and Myasnikova-bulk Hall coefficient data are nearly equivalent if allowance is made for the nanorod-film geometry. It is concluded that while non-impurity defects have no significant effect on the Hall coefficients of Ru thin films at 300 K and above, uncertainties in thickness lead to decreased accuracy of measurements on films with non-slab geometries. In addition, defects and non-slab film geometries have a major influence on film resistivities. Provided that the nanorod spacing l_2 is large enough, the height of the ultra-thin polycrystalline layer at the film-substrate interface is found to be the dominant factor in the determination of the resistivity from the measured resistance of nanorod-structured metallic thin films.

4.7. Effective Thickness of Nanorod Film for Hall Coefficient Estimation

An estimate of the effective thickness of a nanorod film starts by showing that the Hall coefficients of two adjacent slabs of the same thickness and material, carrying the same current density in a uniform external transverse magnetic field, not only equal each other but also equal the Hall coefficient of the combined slab. Refer to Figure 4.5 for a picture that shows a Hall slab split into parts A and B such that $L = L_A + L_B$ and $I_A \neq I_B$.

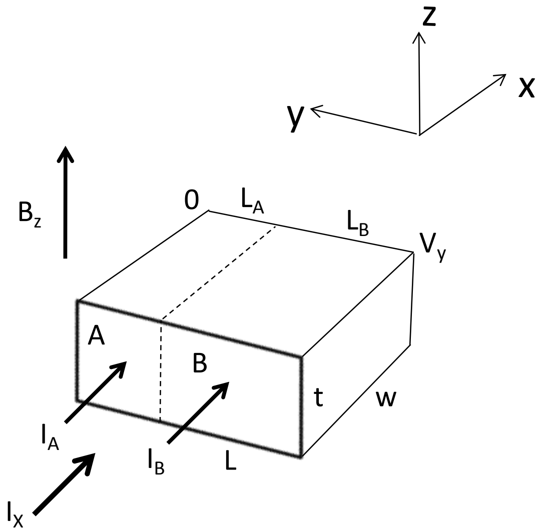

FIGURE 4.5. Homogeneous and isotropic slab divided into parts A and B and carrying a total current I_x (holes as dominant carriers) in an external magnetic field B_z. The electrostatic Hall potential is assumed to rise uniformly from zero on the left to V_y on the right.

The slab sections act as a current divider so that $I_A = (L_A/L)I_x$ and that $I_B = (L_B/L)I_x$. The Hall coefficient of section A follows as

$$R_{HA} = \frac{E_y}{J_x B_z} = \frac{V_y\left(\frac{L_A}{L}\right)t}{I_A B_z} = \frac{V_y t}{I_x B_z} = R_H\ . \tag{4.8}$$

Similarly, for section B, the Hall coefficient follows as

$$R_{HB} = \frac{\left(V_y - V_y\left(\frac{L_A}{L}\right)\right)t}{I_B B_z} = \frac{V_y t}{I_x B_z} = R_H\ . \tag{4.9}$$

That is, for parallel Hall-slab resistors with the same thickness, each section has the same Hall coefficient as the entire slab and, in general, every slab section defined by slicing parallel to the x-z plane has the same Hall coefficient. It is possible to write the Hall coefficient of the entire slab using a rule of mixtures as

$$R_H = \left(\frac{L_A + L_B}{L}\right) R_H = \left(\frac{L_A}{L}\right) R_{HA} + \left(\frac{L_B}{L}\right) R_{HB}\,. \tag{4.10}$$

While (4.10) is seemingly trivial, a rule of mixtures allows an estimate of the Hall coefficient for cases where connected slabs of different thicknesses are combined in series as will be shown below.

Next consider connected slabs with different thicknesses as shown in Figure 4.6. The source current I_x divides by face areas such that $I_A = (L_A t_A/(L_A t_A + L_B t_B))I_x$ and $I_B = (L_B t_B/(L_A t_A + L_B t_B))I_x$. The Hall coefficient of the thick slab A equals that of the thin slab B and reads

$$R_{HA} = R_{HB} = \left(\frac{V_y}{I_x B_z}\right)\left(\frac{L_A t_A + L_B t_B}{L_A + L_B}\right). \tag{4.11}$$

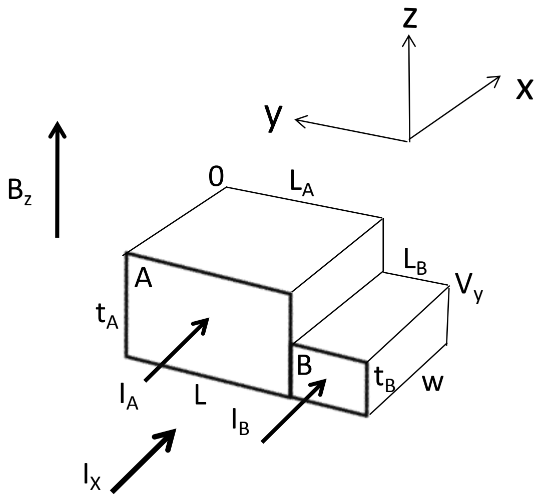

FIGURE 4.6. Homogeneous and isotropic slabs of different thicknesses labeled A and B and carrying a total current I_x in an external magnetic field B_z. The electrostatic Hall potential is assumed to rise uniformly from zero on the left to V_y on the right.

Similar to the results for the sections of the uniform thickness slab in Figure 4.5, the overall Hall coefficient of the connected slabs in Figure 4.6 is equal to the Hall coefficient of either slab since the electric fields and transport currents in both slabs are the same and the external magnetic field is constant. This is consistent with the rule of mixtures equation (4.10):

$$R_H = \left(\frac{L_A}{L}\right) R_{HA} + \left(\frac{L_B}{L}\right) R_{HB} = \left(\frac{L_A + L_B}{L}\right) R_{HA} = R_{HA} = R_{HB}\,. \tag{4.12}$$

When slabs of different thicknesses are connected in series, however, so that the current densities are not the same, it would be expected that the Hall coefficients of the slabs are different. The geometry is illustrated in Figure 4.7.

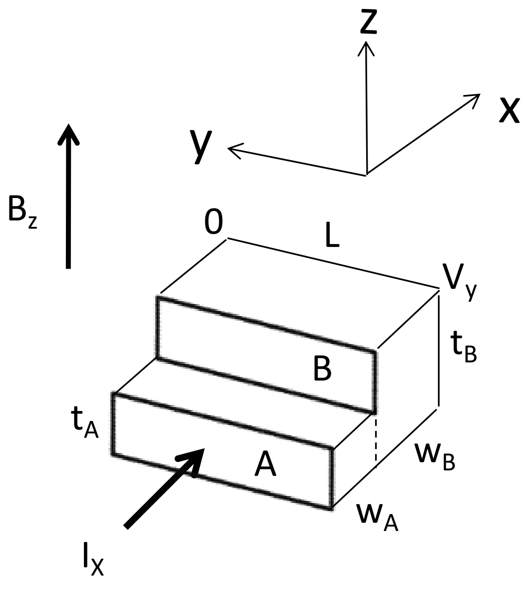

FIGURE 4.7. Connected homogeneous and isotropic slabs of different thicknesses labeled A and B each carrying a current I_x in an external magnetic field B_z. The electrostatic Hall potential is assumed to rise uniformly from zero on the left to V_y on the right.

Since the current densities in the two slabs differ, the Hall coefficients must differ because E_y and B_z are constant. The slabs are in contact yet have different Hall coefficients due to different thicknesses. The Hall coefficient of slab A is

$$R_{HA} = \frac{V_y t_A}{I_x B_z} \tag{4.13}$$

and that of slab B is

$$R_{HB} = \frac{V_y t_B}{I_x B_z}. \tag{4.14}$$

What is the overall Hall coefficient of the composite? That is, when a measurement of Hall potential for a given excitation current and external magnetic field is recorded, what effective thickness is assigned to a film that does not have a uniform thickness, such as a nanorod film, in order to determine the overall Hall coefficient? To answer this question, an effective thickness may be estimated from a Hall coefficient determined by a rule of mixtures. It is recognized that the approach is not rigorous. With reference to Figure 4.7, an overall Hall coefficient may be estimated using the widths w_A and w_B as

$$R_H \approx \left(\frac{w_A}{w_A + w_B}\right) R_{HA} + \left(\frac{w_B}{w_A + w_B}\right) R_{HB} \, . \tag{4.15}$$

Now consider the nanorod model of Figure 4.3, a modification of which is shown in Figure 4.8. For convenience, the array is taken as a lumped n x n nanorod square. (Figure 4.3 shows a 2 x 2 nanorod square where the rods and bases are not lumped together.) The picture, which is not to scale, shows lumped nanorods and lumped gaps in the rear and a lumped continuous gap in the front that extends the entire length of the film.

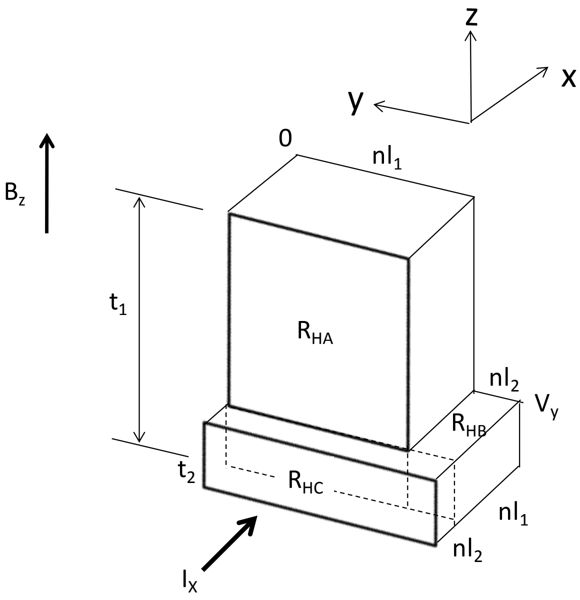

FIGURE 4.8. Lumped nanorod array as three connected homogeneous and isotropic slabs labeled by Hall coefficients as R_{HA}, R_{HB} and R_{HC}. The dimensions t_1 and t_2 represent the rod height and the base height. The nanorod film carries a current I_x in an external magnetic field B_z. The electrostatic Hall potential is assumed to rise uniformly from zero on the left to V_y on the right (y-direction).

From above, the Hall coefficients R_{HA} and R_{HB} are equal to each other and to the Hall coefficient of the composite slab made of components A and B. Using a rule of mixtures as in (4.15), an overall Hall coefficient may be estimated as

$$R_H \approx \left(\frac{l_1}{l_1+l_2}\right) R_{HA} + \left(\frac{l_2}{l_1+l_2}\right) R_{HC} \,. \tag{4.16}$$

From (4.11), R_{HA} (or R_{HB}) is given by

$$R_{HA} = \left(\frac{V_y}{I_x B_z}\right)\left(\frac{l_1 t_1 + l_2 t_2}{l_1 + l_2}\right). \tag{4.17}$$

The expression for R_{HC} is more straightforward and is given by

$$R_{HC} = \left(\frac{V_y t_2}{I_x B_z}\right). \tag{4.18}$$

When (4.17) and (4.18) are substituted into (4.16), the Hall coefficient of the overall slab becomes

$$R_H \approx \left(\frac{V_y t_1}{I_x B_z}\right)\left[\frac{1+\left(\frac{l_2}{l_1}\right)\left(\frac{t_2}{t_1}\right)+\left(\frac{l_2}{l_1}\right)\left(\frac{t_2}{t_1}\right)\left(1+\frac{l_2}{l_1}\right)}{\left(1+\frac{l_2}{l_1}\right)^2}\right]. \tag{4.19}$$

Under the assumptions that $l_2 \ll l_1$ and that $t_2 \ll t_1$, (4.19) simplifies to

$$R_H \approx \left(\frac{V_y t_1}{I_x B_z}\right)\left(1+\frac{l_2}{l_1}\right)^{-2}. \tag{4.20}$$

An effective thickness for a nanorod film t_{1n} may now be estimated by writing the film Hall coefficient as $R_H = \left(V_y t_{1n}/I_x B_z\right)$. Substituting this expression into (4.20), the effective thickness of a nanorod film relative to its nominal thickness, for purposes of Hall coefficient measurements, may be estimated as the nominal thickness decreased by a factor that depends on the rod size and spacing:

$$t_{1n} \approx t_1\left(1+\frac{l_2}{l_1}\right)^{-2}. \tag{4.21}$$

4.8. Closing Note

This chapter is an elaboration of a paper published in Applied Physics Letters in April 2010.[25] Steps in the derivations of the characteristic resistivity temperature θ_R and the effective thicknesses have been added for clarity and completeness.

---

[1] J. C. Bailar, H. J. Emeleus, R. Nyholm and A. F. Trotman-Dickenson, *Comprehensive Inorganic Chemistry* (Pergamon, Oxford, 1973).

[2] G. T. Meaden, *Electrical Resistance of Metals* (Plenum, New York, 1965).

[3] E. Justi, Z. Naturforsch. 4A, 472 (1949).

[4] C. M. Hurd, *The Hall Effect in Metals and Alloys* (Plenum, New York, 1972).

[5]F. Frohlich, D. Machajdik, V. Cambel, J. Fedor, A. Pisch and J. Lindner, J. Phys. IV France 11, 325 (2001).

[6]Y. Matsui, M. Hiratani, T. Nabatame, Y. Shimamoto and S. Kimura, Electrochem. Solid-State Lett. 5 (1), C18 (2002).

[7]S. Kim, N. Koratkar, T. Karabacak and T.-M. Lu, Appl. Phys. Lett. 88, 263106 (2006).

[8]F. Tang, T. Karabacak, L. Li, M. Pelliccione, G.-C. Wang and T.-M. Lu, J. Vac. Sci. Technol. A 25, 1, 160 (2007).

[9]S. C. Moulzolf, D. J. Frankel and R. J. Lad, Rev. Sci. Instrum. 73, 6, 2325 (2002).

[10]American Society for Testing and Materials, ASTM F 76 – 86 (1996).

[11]T. J. Coutts, *Electrical Conduction in Thin Metal Films* (Elsevier, Amsterdam, 1974).

[12]V. Vand, Proc. Phys. Soc. 55, 222 (1943).

[13]J. K. Alstad, R. V. Colvin and S. Legvold, Phys. Rev. 123, 2, 418 (1961).

[14]N. E. Alekseevskii, K.-H. Bertel, A. V. Dubrovin, V. I. Nizhankovskii and L. Urai, JETP Lett. 18, 5, 163 (1973).

[15]N. V. Volkenshteyn, V. A. Novoselov, V. Y. Startsev and Y. P. Romanov, Fiz. Metal. Metalloved. 33, 6, 1233 (1972).

[16]D. Deniz, D. J. Frankel and R. J. Lad, Thin Solid Films 518, 15, 4095 (2010).

[17]J. Volger, Phys. Rev. 79, 1023 (1950).

[18]T. Karabacak, G.-C. Wang and T.-M. Lu, J. Appl. Phys. 94, 12, 7723 (2003).

[18]E. H. Sondheimer, Adv. Phys. 1, 1, 1 (1952).

[20]J.-P. Jan, *Solid State Physics*, Vol. 5 (Academic Press, New York, 1957).

[21]H. B. Callen, *Thermodynamics* (Wiley, New York, 1960).

[22]I. S. Grigoriev and E. Z. Meilikhov, eds., *Handbook of Physical Quantities* (CRC Press, Boca Raton, 1997).

[23]R. W. Powell, R. P. Tye and M. J. Woodman, J. Less-Common Metals 12, 1 (1967).

[24]R. P. Vasil’yeva, A. V. Cheremushkina and N. N. Ivanova, Fiz. Metal. Metalloved. 35, 4, 872 (1973).

[25]M. M. Steeves, D. Deniz and R. J. Lad, Appl. Phys. Lett. 96, 142103 (2010).

Chapter 5

RUTHENIUM DIOXIDE THIN FILMS

5.1. Chapter Abstract

Polycrystalline thin films of RuO_2 were grown on fused quartz substrates and a parametric study was carried out to probe the influence of film nanostructure on the four-point van der Pauw resistivity and Hall coefficient. The films were grown via reactive RF magnetron sputtering of a Ru target in an Ar/O_2 plasma using deposition rates from 0.27 to 3.5 Å/s and substrate temperatures from 16 to 500 °C. Room temperature resistivities of the RuO_2 films ranged from 58 to 360 μΩ cm. Upon first heating following deposition, some films showed decreasing resistivity with increasing temperature, but the resistivities also decreased upon subsequent cooling suggesting that the annealing treatment reduced the film defect density. The temperature coefficient of resistance was found to be small ($<0.001\ K^{-1}$) in agreement with previous investigations. Hall coefficient measurements of the polycrystalline thin films demonstrated that either n-type or p-type carriers can be present depending on the deposition conditions and resulting nanostructure, in contrast to single-crystal RuO_2, which is an n-type metal. Grain size and homogeneous strain within the films were measured by x-ray diffraction and are correlated to the dominant carrier type.

5.2. Background Information

As pointed out in Chapter 1, stoichiometric single-crystal ruthenium dioxide[1-6] crystallizes in the same rutile structure as the more widely studied titanium dioxide[7,8] but is an n-type metal instead of a wide band-gap semiconductor. Variations of the oxygen vacancy concentration in TiO_{2-x} make it a defect-doped, n-type semiconductor with a wide range of possible resistivities. However, oxygen vacancies do not appear to significantly change the metallic character of RuO_2.[9] Based on TiO_2, it might be expected that oxygen vacancies would enhance the population of n-type carriers (electrons). However, for polycrystalline thin films of RuO_2, a report of p-type conduction[10] at 30 K and reports of zero or even negative temperature coefficients of resistance[10-15] have appeared in the literature. Negative temperature coefficients are typically associated with intrinsic semiconductors, not with metals, and it is inferred that a decrease in RuO_2 resistivity with increasing temperature must be due to the defect structures within the films.[16,17] The purpose of this work was to further investigate the dominant-carrier type, resistivity, and temperature coefficient of resistance of polycrystalline RuO_2 thin films grown by reactive RF magnetron sputtering and to correlate these transport properties to the deposition process and resulting defect structure.

5.3. Properties of RuO_2

With reference to Chapter 1, ruthenium dioxide is a stable, semi-transparent, transition-metal oxide with higher electrical conductivity than about one-third of the pure metals in the periodic table.[18] In single-crystal form, its average room-temperature resistivity[1] of 35.2 $\mu\Omega$-cm is approximately five times that of ruthenium.[18] RuO_2 is classified as a metal since its Fermi level lies in the middle of a conduction-band density-of-states curve that is comprised primarily of Ru-4d orbitals.[2] Furthermore, the energy-versus-wave vector dispersion bands at the Fermi level indicate that conduction in RuO_2 is both by electrons (dominant carriers) and holes.[2,5,6] Single-crystal ruthenium dioxide is an n-type metal with an average room-temperature Hall coefficient[1] of -11 x 10^{-5} cm^3/C, contrasted to ruthenium, which is a p-type compensated metal[19] with an average room-temperature Hall coefficient[20] of +22 x 10^{-5} cm^3/C. RuO_2 possesses the rutile structure (Structurbericht C4, space group $P4_2/mnm$) with a tetragonal unit cell (a = 4.492 Å, c = 3.107 Å) with ruthenium atoms in a body-centered configuration, each surrounded by six oxygen atoms in an octahedral coordination with two RuO_2 molecules per unit cell. In terms of oxide temperature stability, RuO_2 dissociates at 1540 °C at a pressure of one atmosphere.[21] The (110) surface is reported to be thermally stable in ultrahigh vacuum at 600 K.[22] However, as pointed out in Chapters 6 and 7, polycrystalline RuO_2 may be unstable in high vacuum above room temperature and also in reducing atmospheres, such as carbon monoxide, above room temperature.

5.4. Experimental Details

All polycrystalline RuO_2 thin films were deposited on amorphous GE Type-124 fused-quartz substrates by confocal reactive RF magnetron sputtering of a 76 mm diameter, 99.95 % pure ruthenium target in an Ar/O_2 plasma deposition system (AJA International). The Ar/O_2 ratio in the sputter gas was 45/55 at a total pressure of approximately 3.5 x 10^{-3} Torr (0.5 Pa) during depositions.[10] The target-to-substrate distance was 17 ± 1 cm with the target tilted 17° from the vertical in the direction of the rotating substrate (14 rpm). Circular films for the van der Pauw geometry experiments were deposited through a 17 mm mask to a typical thickness of 140 nm. Substrate temperatures during deposition were adjusted between 16 and 500 °C and deposition rates were varied from 0.27 to 3.5 Å/s, corresponding to RF powers of 200 to 500 W.

Transport measurements were made using a four-point van der Pauw resistivity and Hall-effect apparatus, which is described in Chapter 3.[23] Measurements were made in both high vacuum ($\approx 10^{-5}$ Torr) and in air at one atmosphere with temperatures ranging from ambient to approximately 300 °C. The transport system was calibrated using single-crystal n-type and p-type silicon wafers, unannealed gold thin films, and a commercial silicon standard (MMR Technologies). As an example of the calibration, at 293 K the transport system yielded an average Hall coefficient for a 300 nm unannealed gold film of -6×10^{-5} cm^3/C compared to published values for gold films evaporated on glass of $-8 \pm 1 \times 10^{-5}$ cm^3/C.[20] Measurements conformed to the standard test methods outlined in ASTM F76 - 86.[24]

5.5. Comparison of RuO_2 and Ru Thin Film Resistivities

Figure 5.1 compares the resistivity as a function of temperature of two films: an unannealed RuO_2 film deposited confocally at 3.5 Å/s onto a 16 °C fused-quartz substrate and an unannealed Ru film deposited normally by RF magnetron sputtering at 0.5 Å/s onto an 18 °C microscope-glass slide using a different deposition system (Lesker - Chapter 3). According to Matthiessen's rule, the resistivity of a metal should consist of two components: (i) a small residual resistivity that is independent of temperature caused by impurities, other defects, and strain, and (ii) an ideal resistivity that rises with temperature due to lattice vibrations (phonons). This behavior is clearly not the case for the two metal films, which exhibit falling resistivity upon a first heating. Since resistivity is due to deviations from a perfect, static lattice, it is evident that defects such as vacancies, interstitials, grain boundaries, and dislocations play a significant role in determining the initial resistivity. The drop in resistivity due to annealing with temperature and time for certain unannealed metal films might be attributed to the removal of vacancies and interstitials by annealing,[16,17] although reduction of other defects such as grain boundary surface areas should also lower the resistivity. When the two metal films were cooled to room temperature, the resistivities traced lines with positive slopes in accordance with the phonon component of Matthiessen's rule.

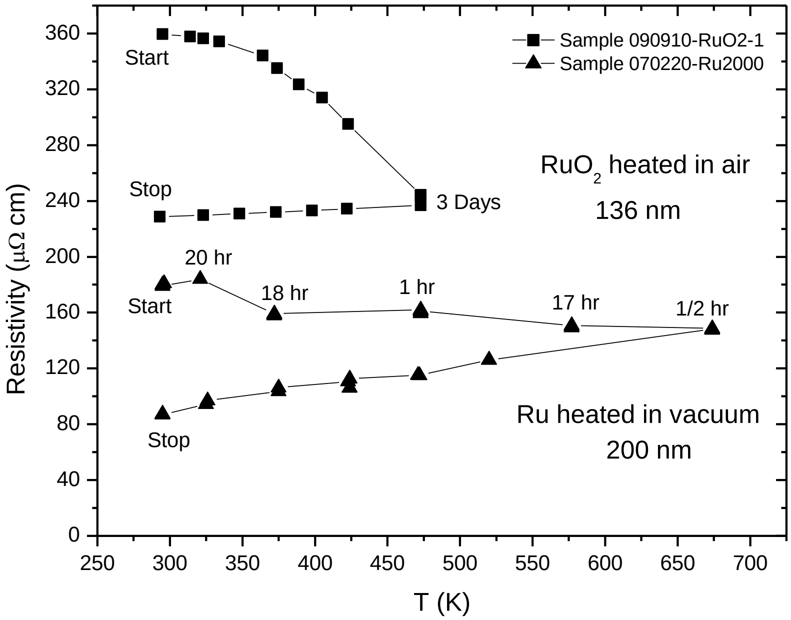

FIGURE 5.1. Comparison of RuO_2 and Ru metal films showing decreasing resistivity as a function of temperature upon first heating. Neither film received thermal treatment prior to these resistivity measurements.

The resistivities of seven RuO_2 films versus temperature are shown in Figures 5.2 and 5.3 (Figure 5.2: first heating; Figure 5.3: first cooling). The plots also show how these values compare to measured resistivity data for single-crystal RuO_2.[1] The legend in Figure 5.2 gives the film designation, while that in Figure 5.3 gives the deposition parameters and post-deposition thermal treatments, if any, of the same films. Three unannealed films deposited at relatively high rates showed falling resistivities upon first heating in the van der Pauw apparatus. Three pre-annealed and one unannealed film

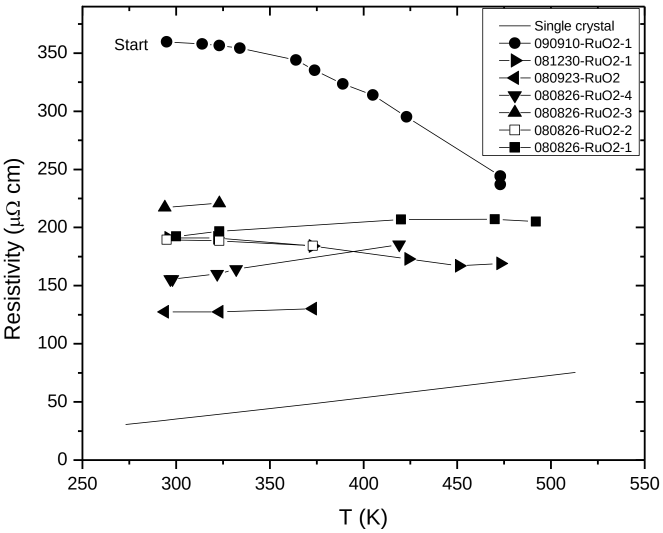

FIGURE 5.2. Resistivity during first heating for seven polycrystalline RuO_2 thin films fabricated under different conditions. The films are compared to single-crystal RuO_2.[1]

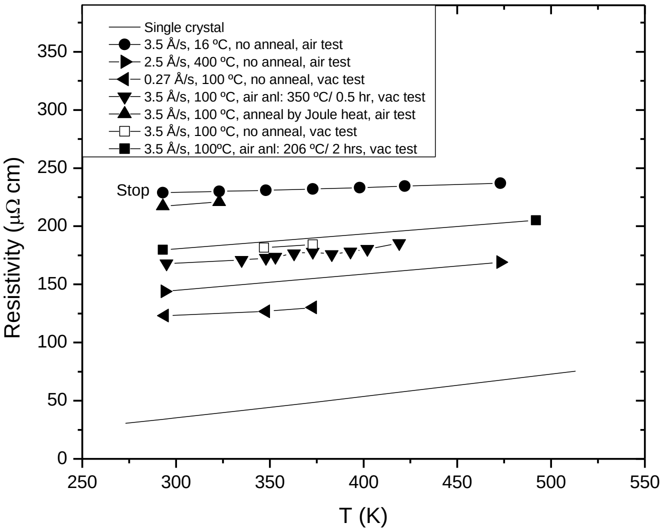

FIGURE 5.3. Resistivity during first cooling of the seven different polycrystalline RuO_2 thin films fabricated under the different conditions and shown in Fig. 5.2.

showed rising resistivities upon first heating. Upon first cooling, all seven films showed positive slopes which are characteristic of metallic behavior. Subsequent thermal cycling (data not shown) exhibited positive slopes with final room-temperature resistivities lower than those in Figure 5.3 by a few percent.

5.6. Temperature Coefficient of Resistance

The temperature coefficient of resistance, defined as $\alpha = (1/\rho)(\partial\rho/\partial T)$, at 293 K for the seven RuO_2 films shown in Figures 5.2 and 5.3 is plotted against room-temperature resistivity in Figure 5.4. In temperature coefficient of resistance calculations, the slopes were those of the cooling curves and the resistivities were those of the points labeled “Stop” in Figure 5.3. Included in Figure 5.4 are values for a number of metals and alloys[25] for comparison to the RuO_2 films. Single-crystal RuO_2 has a value similar to bulk metals like indium, tin, or zirconium. The seven polycrystalline RuO_2 films tested in this study have extremely small temperature coefficients of resistance, comparable to bulk nickel alloys like nichrome, invar, or constantan. It should be noted, however, that the RuO_2 film resistivities are significantly higher than those of the nickel-based alloys.

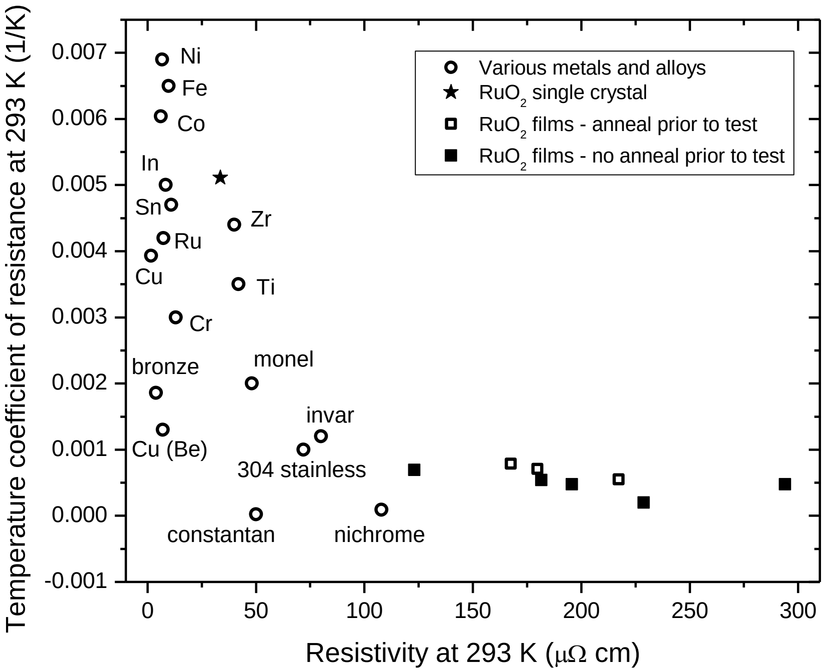

FIGURE 5.4. Temperature coefficient of resistance versus resistivity at 293 K comparing RuO_2 in single-crystal form (star) and polycrystalline thin-film form (squares) to various metals and alloys.[25] Uncertainty in RuO_2 data is about half the plotted values.

5.7. Resistivity as a Function of Process

The resistivities of twenty four different films measured at 295 K are plotted as a function of substrate deposition temperature with deposition rate as a parameter in Figure 5.5. The room-temperature resistivity drops with increases in deposition substrate temperature from 16 to 500 °C, but the decrease is not monotonic with a small peak at midrange temperatures for all rates from 0.27 to 3.5 Å/s. The lowest resistivity film observed (58 μΩ-cm) resulted from a deposition rate of 1.2 Å/s on a 500 °C substrate; this resistivity was 65% higher than the single-crystal average. The two highest resistivities were observed at the fastest deposition rate of 3.5 Å/s but at substrate temperatures of 16 and 300 °C.

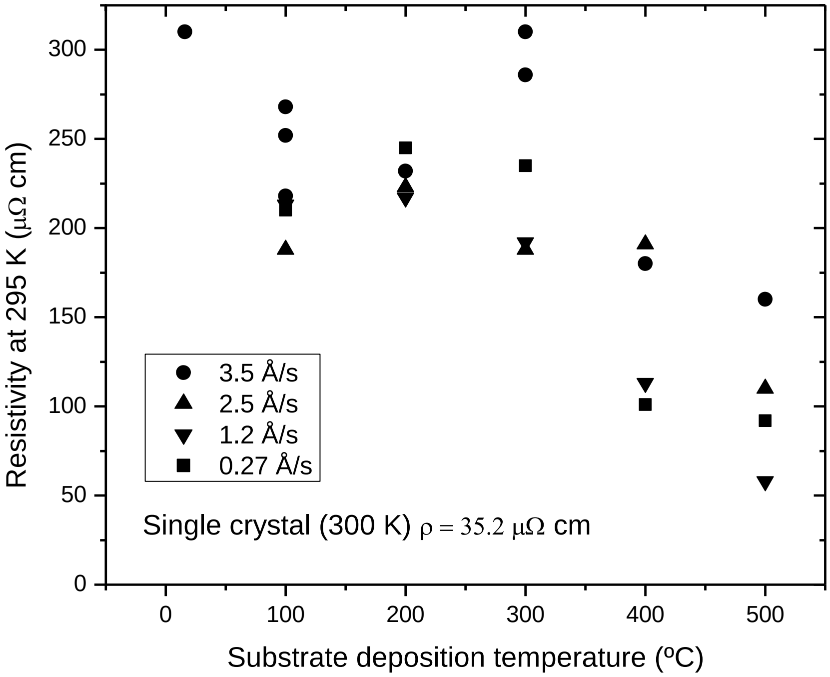

FIGURE 5.5. Resistivity at 295 K as a function of substrate deposition temperature with deposition rate as a parameter. Data for 24 different RuO_2 films are shown. Uncertainty in resistivity is about ± 5 % of measured values. Films that were grown by the same process showed about a 50 μΩ cm spread in resistivity (see 3.5 Å/s data at 100 °C).

5.8. Hall Coefficient as a Function of Process

The Hall coefficients for fourteen different films measured at 295 K with a 0.3 T magnetic field are plotted in Figure 5.6 as a function of substrate deposition temperature with deposition rate as a parameter. These data indicate that conduction occurs by both p-type and n-type majority carriers in contrast to bulk single-crystal RuO_2, in which conduction is exclusively n-type.[1] The results are difficult to generalize, but the slowest deposition rate (0.27Å/s) appeared to yield electrons as dominant carriers, while higher rates yielded either electrons or holes as dominant carriers as substrate temperature was increased. The appearance of both types of carriers is consistent with the energy-band dispersion curves[2-6] (energy versus wave vector) for RuO_2 at the Fermi energy.

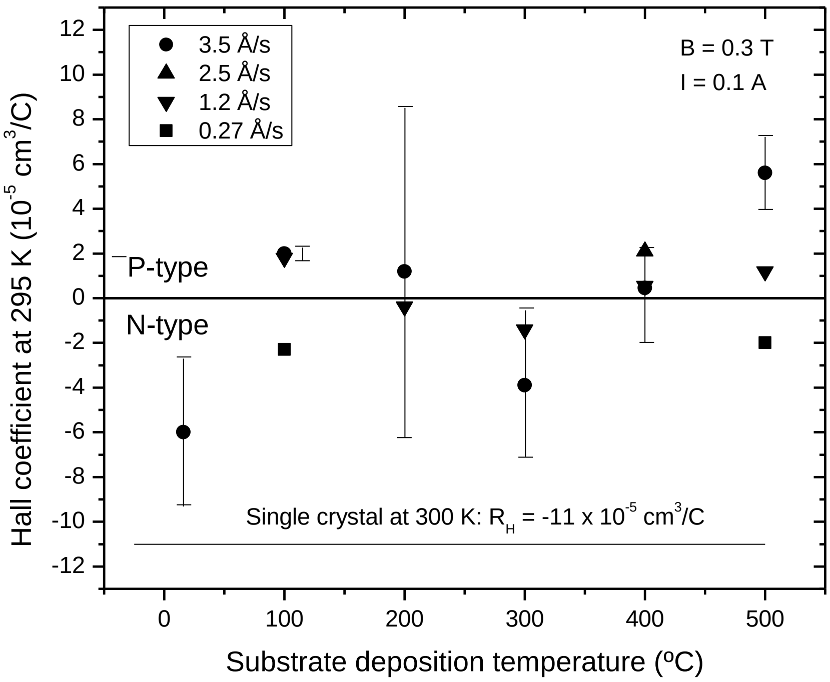

FIGURE 5.6. Hall coefficient at 295 K as a function of substrate deposition temperature with deposition rate as a parameter. Data for 14 different RuO_2 films are shown. Error bars are included for the 3.5 Å/s samples as an example of measurement uncertainty.

5.9. Hall Coefficient as a Function of Current

Figure 5.7 shows the Hall coefficient at 295 K and 0.3 T as a function of measuring current for two samples grown under contrasting conditions with no post-deposition annealing (3.5 Å/s, 100 °C substrate and 0.27 Å/s, 500 °C substrate). The data scatter is significantly higher at low currents, illustrating a serious concern for accuracy of Hall measurements of very thin films in a noisy environment. At larger test currents, the signal-to-noise ratio and data reliability are much improved, but at these larger currents, Joule heating from the test current becomes more important. During the Hall testing shown in Figure 5.7, Joule heating annealed both films thereby lowering resistivity and film defect density. However, the results in Figure 5.7 show that defect annihilation which presumably occurs by Joule heating has minimal, if any, effect on the Hall coefficients, at least for these two samples.

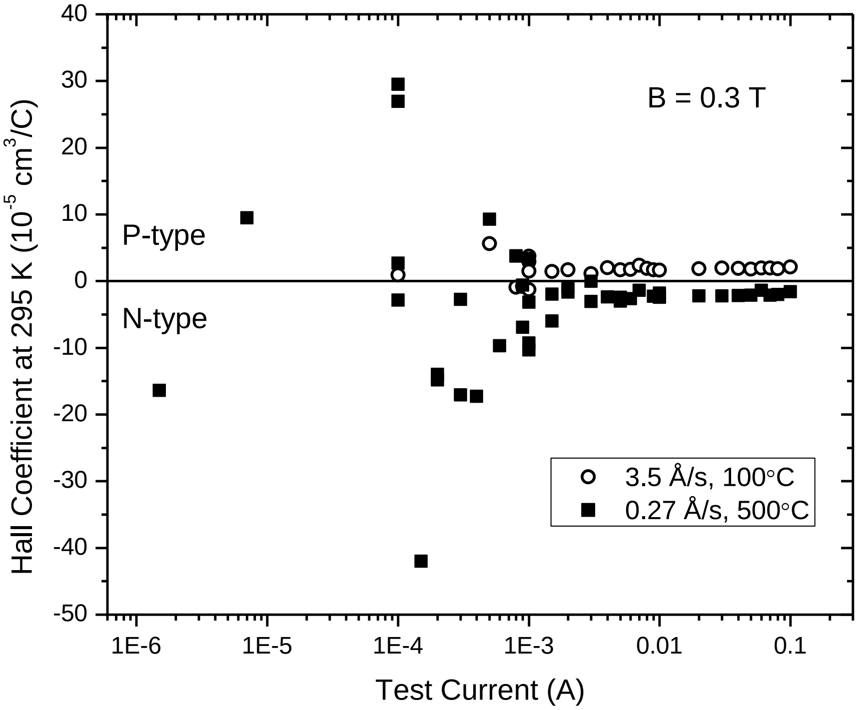

FIGURE 5.7. Hall coefficient at 295 K as a function of test current for two contrasting samples: high-rate, low-substrate temperature versus low-rate, high-substrate temperature. Background noise significantly scattered measurements for currents below one milliampere.

5.10. Grain Size and Homogeneous Strain

The crystalline structures of the two films reported in Figure 5.7 were investigated by three techniques of x-ray diffraction (θ/2θ, grazing incidence, and in-plane scattering) to examine crystallite planes that were respectively parallel, tilted, and perpendicular to the film surface. Figure 5.8 shows grain size as a function of tilt angle from the surface plane of the film based on diffraction from different Miller index (hkl) planes of RuO_2.

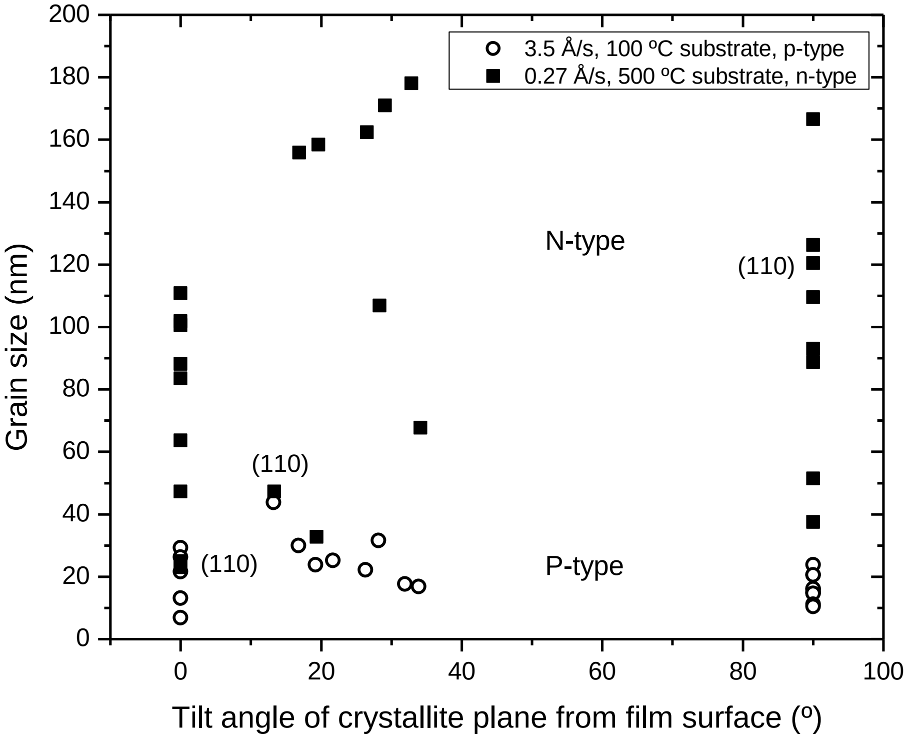

FIGURE 5.8. Grain size as a function of tilt angle of crystallite planes from the film surface as measured by x-ray diffraction. Points represent different Miller-index planes. Data at 0° are from $\theta/2\theta$ scans (size transverse to surface), at 13° to 34° from grazing incidence scans (size angled from surface), and at 90° from in-plane scans (size parallel to surface). The (110) planes for the n-type sample are shown as an example. See Table 5.1 for a detailed listing of the data.

Note that the intent of Figure 5.8 is simply to demonstrate by measurement that the n-type sample consisted of larger crystallites than the p-type sample; the sizes plotted should be taken as indicative of relative sizes and not as accurate sizes. That is, grain sizes were estimated by the Scherrer equation and are likely to be overestimates since, in general, the statistical size distribution is expected to be log-normal.[26]

TABLE 5.1. Tilt angle, grain size, and Miller index plane for data of Figure 5.8.

0.27 Å/s, 500 °C substrate, n-type			3.5 Å/s, 100 °C substrate, p-type		
Tilt (deg)	Size (nm)	hkl	Tilt (deg)	Size (nm)	hkl
0	25	110	0	29.3	110
0	110.8	101	0	26.3	200
0	101.9	200	0	13.1	211
0	88.1	111	0	21.6	220
0	47.3	211	0	6.9	310
0	100.6	002	13.2	43.8	110
0	83.5	112	16.8	30	101
0	23	301	19.2	23.8	200
0	63.7	202	21.7	25.2	210
13.4	47	110	26.3	22.2	211
16.9	156	101	28.1	31.6	220
19.4	33	200	31.9	17.7	310
19.6	158	111	33.9	16.8	301
26.5	162	211	90	20.5	110
28.3	107	220	90	15.9	101
29.1	171	002	90	23.8	111
32.9	178	112	90	15.2	211
34.1	68	301	90	14.8	220
90	120.4	110	90	16.2	002
90	166.6	101	90	14.6	310
90	126.2	200	90	11.2	112
90	88.7	210	90	10.4	301
90	93	211	90	20.5	202
90	109.5	220			
90	51.4	310			
90	37.5	301			

With regard to measurement technique, instrumental peak broadening was negligible compared to sample broadening and peak positions were calibrated using LaB_6 powder as a standard reference material.[27] The average grain sizes are listed in Table 5.2 along with average homogeneous strains parallel and perpendicular to the film surface, calculated from x-ray diffraction peak shifts. It is seen that the average grains are approximately cubical and that the low-rate film contains average crystallite volumes that are roughly 100 times larger than the high-rate film. As indicated in Table 5.2, strains in the fast-deposition-rate film were about an order of magnitude higher than those in the slow-rate film, which was nearly strain free. Based on Poisson's ratio considerations for macroscopic strains, it might be expected that the strain parallel to the film surface for the fast-rate sample would be compressive (negative sign) and not +0.39 % as shown, because strain perpendicular to the surface was tensile. The fact that positive strains were observed in both directions suggests that there may be two different types of grains, each with tensile components either parallel or perpendicular to the film.

TABLE 5.2. Comparison of two unannealed films with different dominant carriers.

Deposition rate, substrate temp	0.27 Å/s, 500°C	3.5 Å/s, 100°C
Resistivity (295 K)	92 μΩ cm	218 μΩ cm
Film thickness	180 nm	150 nm
Strain parallel to surface	0.09 %	0.39 %
Strain perpendicular to surface	-0.05 %	0.91 %
Avg grain size parallel to surface	99 nm	16 nm
Avg grain size perpendicular to surface	72 nm	19 nm
Dominant carrier	Electrons	Holes

Figure 5.9 presents the θ/2θ and in-plane (grazing entrance – grazing exit) scans of the two films listed in Tables 5.1 and 5.2. The two films are clearly textured and do not show a random distribution of crystallites. In general, thin films show fiber texture in a direction perpendicular to the substrate.

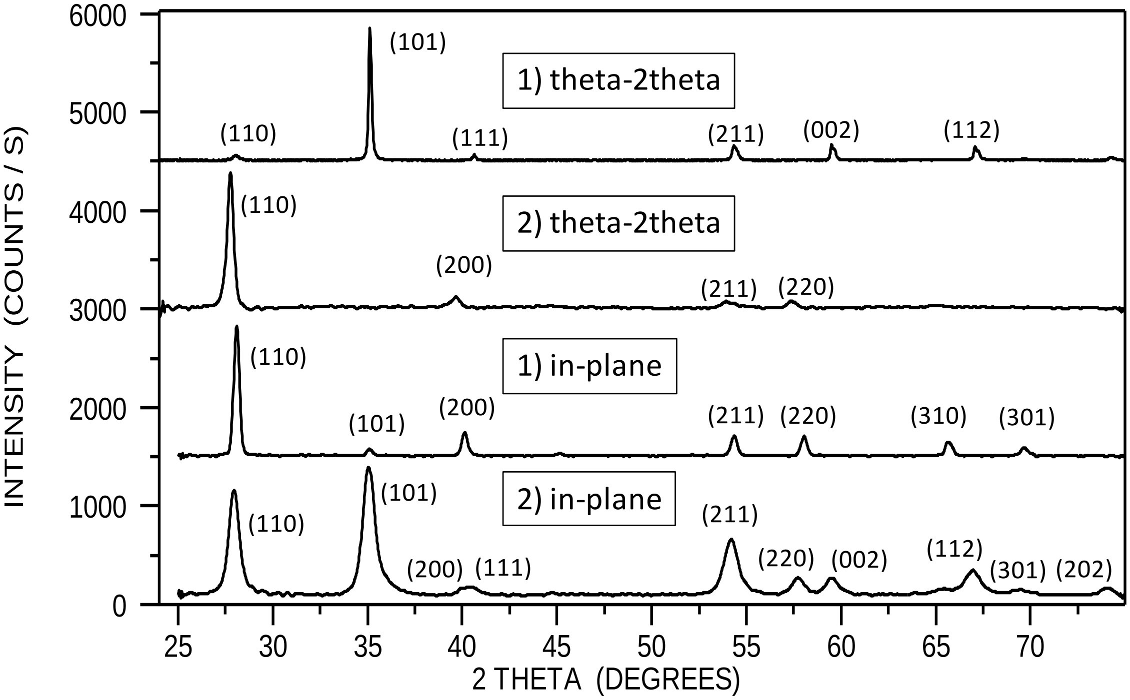

FIGURE 5.9. X-ray diffraction scans examining crystallite planes that are parallel (θ-2θ) and perpendicular (in-plane) to the surfaces of two highly contrasting RuO_2 films. Both films were unannealed and are characterized as 1) 0.27 Å/s, 500 °C substrate, n-type, large grains and 2) 3.5 Å/s, 100 °C substrate, p-type, small grains.

5.11. Discussion

When thin metal films show decreasing resistivity upon heating, the decreases must be due to less carrier scattering caused by a reduction in the film defect density, with kinetics governed by a specific time-temperature annealing process. Once a large number of film defects are eliminated, the resistivity will increase with increasing temperature in accordance with Matthiessen's rule. This behavior applies to RuO_2 as well as to pure metals such as ruthenium and also applies to non-stoichiometric RuO_{2-x} (oxygen vacancies as defects). There is no defect-doped semiconducting phase of RuO_2 as there is for TiO_2, where conduction by activation energy would improve upon heating, thereby lowering resistivity. The polycrystalline RuO_2 films synthesized in this study do display smaller resistivity-versus-temperature slopes and lower temperature coefficients of resistance than single-crystal RuO_2, in agreement with observations by other investigators.

The changes in the sign of the Hall coefficient with different deposition conditions indicate that two-carrier conduction takes place in RuO_2 films. It is believed that the occurrence of positive Hall coefficients in RuO_2 is not due to a combination of contact misplacement and non-uniform resistivity as is possible, for example, in the case of the n-type semiconductor ZnO.[28] It appears likely that the hole concentration in single-crystal RuO_2 is either just slightly smaller than the electron concentration or equal to the electron concentration with holes having lower mobilities. Two-carrier conduction with equal carrier concentrations is a situation found in compensated metals[19] and RuO_2 follows this trend. The results indicate that annealing via Joule heating during the Hall coefficient measurement does not appear to influence the sign of the Hall coefficient.

When comparing a slow-deposition-rate, high-substrate-temperature film to a fast-deposition-rate, low-substrate temperature film (Figures 5.7-5.9), a change in the sign of the Hall coefficient from n-type to p-type was brought about by changing from high surface adatom mobility during deposition to a condition where adatom mobility becomes much more limited during the growth process. Dominant conduction by electrons correlates with larger grains and nearly zero homogeneous strain, as measured by x-ray diffraction, which is produced during a high adatom mobility growth condition. Dominant conduction by holes correlates with smaller grains and order-of-magnitude higher film strain, suggesting that the defect grain boundaries may be the major source of the p-type carriers.

5.12. Conclusions

The resistivity and temperature-coefficient-of-resistance of RuO_2 thin films are strongly dependent on the film defect density, but the Hall coefficient appears to be less sensitive to the defect structure. Highly defective films show decreasing resistivity upon a first heating, which is reminiscent of the behavior of an intrinsic semiconductor, but this behavior is due to annealing of film defects. Subsequent cooling and heating treatments lead to the characteristic resistivity versus temperature dependence that is expected for metal films. The RuO_2 films do have very low temperature coefficients of resistance (<0.001 K^{-1}), a characteristic that can be exploited in several technical applications, provided that the film structure displays long-term time stability. The RuO_2 thin films in this study exhibited mixed electron-hole conduction, with the hole concentration being nearly equal to the electron concentration. It was found that different RF magnetron sputtering parameters, and hence different film grain structures and strains, can lead to changes from n-type to p-type conduction.

5.13. Closing Note

This chapter is a slight modification of a paper published in the Journal of Vacuum Science and Technology A in July-August 2010.[29]

---

[1] W. D. Ryden, A. W. Lawson and C. C. Sartain, Phys. Rev. B 1, 1494 (1970).

[2] L. F. Mattheiss, Phys. Rev. B 13, 2433 (1976).

[3] J. E. Graebner, E. S. Greiner and W. D. Ryden, Phys. Rev. B 13, 2426 (1976).

[4] J. H. Xu, J. Jarlborg and A. J. Freeman, Phys. Rev. B 40, 7939 (1989).

[5] K. M. Glassford and J. R. Chelikowsky, Phys. Rev. B 47, 1732 (1993).

[6] K. M. Glassford and J. R. Chelikowsky, Phys. Rev. B 49, 7107 (1994).

[7]U. Diebold, Surface Science Reports 48, 53-229 (2003).

[8]P. A. Cox, *Transition Metal Oxides* (Oxford, New York, 1992).

[9]L. Krusin-Elbaum, Thin Solid Films 169, 17-24 (1989).

[10]K. Y. Tong, V. Jelenkovic, W. Y. Cheung and S. P. Wong, J. Mat. Sci. Let. 20, 699 (2001).

[11]Q. X. Jia, Z. Q. Shi, K. L. Jiao, W. A. Anderson and F. M. Collins, Thin Solid Films 196, 29-34 (1991).

[12]K. L. Jiao, Q. X. Jia and W. A. Anderson, Thin Solid Films 227, 59-65 (1993).

[13]V. G. Grebenkina, D. E. Dyshel, M. D. Smolin and V. N. Fedorov, Soviet Powder Metallurgy and Metal Ceramics 29, 396-399 (1990).

[14]E. V. Jelenkovic, K. Y. Tong, W. Y. Cheung and S. P. Wong, Microelectronic Engineering 71, 237-241 (2004).

[15]Y. T. Kim, Appl. Phys. Lett. 70 (2), 209 (1997).

[16]T. J. Coutts, *Electrical Conduction in Thin Metal Films* (Elsevier, Amsterdam, 1974).

[17]V. Vand, Proc. Phys. Soc. 55, 222-246 (1943).

[18]G. T. Meaden, *Electrical Resistance of Metals* (Plenum, New York, 1965).

[19]N. E. Alekseevskii, K. H. Bertel, A. V. Dubrovin, V. I. Nizhankovskii and L. Urai, JEPT Letters 18 (5), 163 (1973).

[20]C. M. Hurd, *The Hall Effect in Metals and Alloys* (Plenum, New York, 1972).

[21]P. Kofstad, *Nonstoichiometry, Diffusion, and Electrical Conductivity in Binary Metal Oxides* (Wiley, New York, 1972).

[22]K. Reuter and M. Scheffler, Phys. Rev. B 65, 035406 (2001).

[23]S. C. Moulzolf, D. J. Frankel and R. J. Lad, Rev. Sci. Instrum. 73, 2325 (2002).

[24]American Society for Testing and Materials, ASTM F 76 – 86 (1996).

[25]General Electric Company, *Technical Data* (1976).

[26]M. Birkholz, *Thin Film Analysis by X-Ray Scattering* (Wiley-VCH, Weinheim, 2006).

[27]National Institute of Standards and Technology, Standard Reference Material 660a (LaB_6).

[28]T. Ohgaki, N. Ohashi, S. Sugimura, H. Ryoken, I. Sakaguchi, Y. Adachi and H. Haneda, J. Mater. Res. 23, 2293 (2008).

[29]M. M. Steeves and R. J. Lad, J. Vac. Sci. Technol. A 28, 4, 906 (2010).

Chapter 6

OXYGEN LOSS IN DEFECTIVE RUO_2 THIN FILMS

6.1. Chapter Abstract

During the course of this study it was noticed that certain RuO_2 films lost oxygen upon heating to a few hundred degrees Celsius in high vacuum (≈ 10^{-5} torr) and became two-phase mixtures of Ru and RuO_2 as evidenced by x-ray diffraction. The existence of two phases might explain, in some cases, how a polycrystalline RuO_2 film, which is an n-type conductor when stoichiometric, or nearly so, might show p-type conduction in Hall measurements. The films that lost oxygen were typically those with higher defect contents, i.e., films that were grown at high confocal deposition rates on cold substrates. As pointed out in Chapter 1, studies have suggested that even single-crystal RuO_2 surfaces are non-stoichiometric,[1] and this lack of surface stoichiometry along with high sub-surface defect contents may be enough to destabilize films in some situations. Note that loss of oxygen from RuO_2 films was also observed in films exposed to reducing carbon monoxide atmospheres as will be shown in Chapter 7. The discussion in this chapter is restricted to films exposed to and annealed in high vacuum.

6.2. Oxygen Loss in High Vacuum

According to a high temperature study of the ruthenium-oxygen system by Bell and Tagami,[2] the dissociation pressure of RuO_2 in one atmosphere of pure oxygen is 1540 °C. A pressure-temperature phase diagram for RuO_2 was presented by Brunetti et al.[3] that covers the range of temperatures from 986 to 1221 K (713 to 948 °C). They propose a dissociation pressure (kPa) according to the following equation:

$$log(p) = (10.52 \pm 0.30) - \left(\frac{15143 \pm 400}{T}\right). \tag{6.1}$$

This equation indicates that at 986 K (713 °C) oxygen will be lost from the surface of RuO_2 at a pressure of 14.5 mPa ($1.1x10^{-4}$ torr), which corresponds to high vacuum. Extrapolation to temperatures of the order of 300 °C predicts dissociation pressures below the ultrahigh vacuum range (≈ 10^{-15} torr), far below the high vacuum levels in the experiments of this study (≈ 10^{-5} torr).

A plot of the Gibbs free energy of formation of RuO_2 is compared to rutile TiO_2 in Figure 6.1 (Ellingham diagram), where it is clearly seen that TiO_2 is a far more stable oxide. When tie lines from the origin in the upper left hand corner are extended to the right hand vertical axis at a given pressure, the intersection of the lines with the formation-energy lines gives the temperature corresponding to that pressure. Pressures have been calculated from the equilibrium expression for the reaction between ruthenium metal and oxygen gas $Ru(s) + O_2(g) = RuO_2(s)$ where s stands for solid and g for gas. The standard Gibbs free energy with the chemical activities of the two solids taken as unity follows as

$$\Delta G_f^o = RTlnp_{O_2}. \tag{6.2}$$

Figure 6.1 shows that from the point of view of equilibrium thermodynamics, stoichiometric RuO_2 should be stable in high vacuum at temperatures ranging from 100 to 300 °C. That is, ruthenium dioxide should not undergo a significant loss of oxygen resulting in a two phase system of Ru and RuO_2.

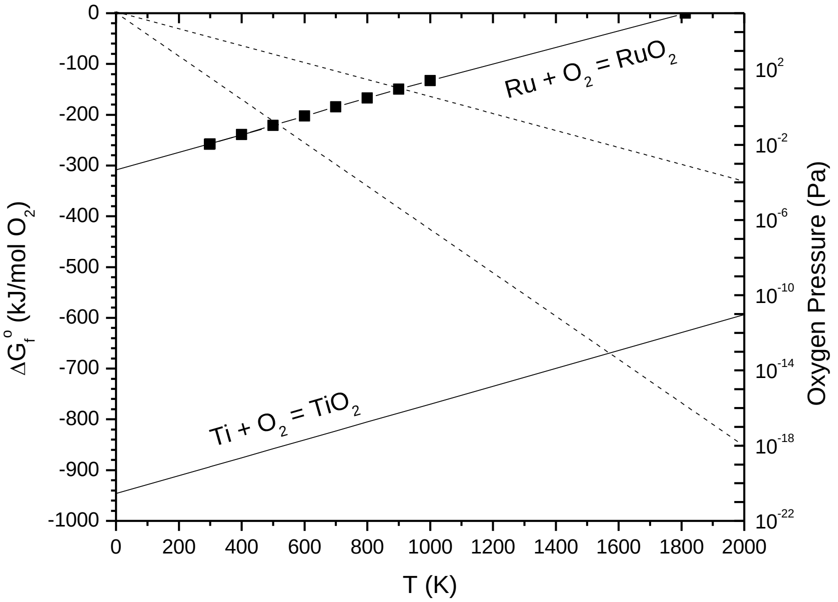

FIGURE 6.1. Free energy of formation as a function of temperature comparing RuO_2 and rutile TiO_2. Temperatures corresponding to given oxygen pressures may be read from intersections of the solid lines with the dashed lines, which are shown as examples. Data for RuO_2 are from references 2 and 4; data for TiO_2 are from reference 5.

6.3. Experimental Evidence of Oxygen Loss in Defective RuO_2 Films

As argued above, from the point of view of equilibrium thermodynamics, RuO_2 thin films should not lose oxygen in high vacuum at temperatures in the 100 - 300 °C range. Yet some films grown under deposition conditions favoring a high defect content did indeed lose oxygen during post-deposition annealing and became two-phase systems. As an example of oxygen loss from a RuO_2 sample, consider Figure 6.2. Exposure to moderate temperatures in high vacuum significantly altered the nanostructure of the film and gave rise to a pure ruthenium phase.

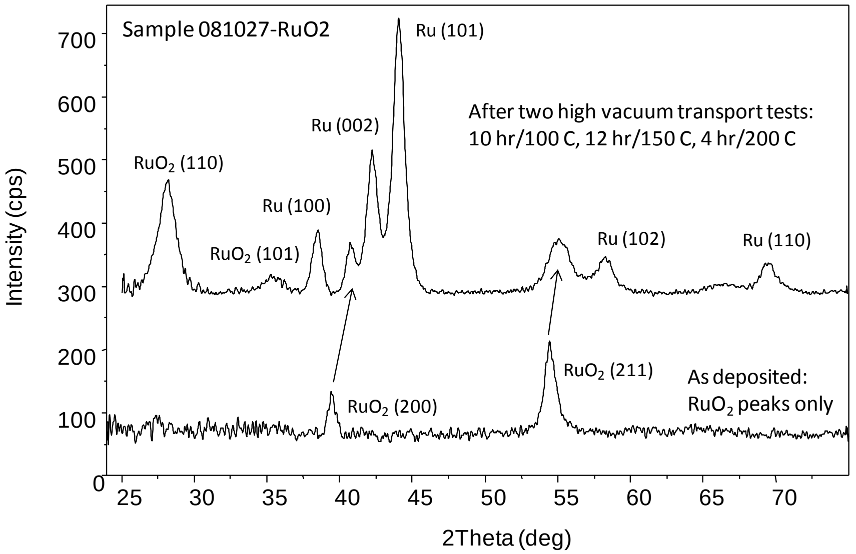

FIGURE 6.2. X-ray diffraction grazing-incidence scans of a sample (081027-RuO2) grown by reactive magnetron sputtering at a high rate on a cold substrate (3.5 Å/s, 16 °C) in a confocal deposition system. The lower trace shows the as-deposited sample. After one day at 100 - 200 °C in a vacuum of roughly 10^{-6} torr, the upper trace shows both RuO_2 and Ru peaks.

Another example is shown in Figure 6.3, where a sputtered film grown at a high deposition rate on a warmer substrate (3.5 Å/s, 100 °C) was followed by a low temperature anneal in air (206 °C for 2 hours). There are no evident Ru peaks seen from the air-annealed film, but when the film was placed in high vacuum and heated in the range of 200 - 300 °C for about one day, Ru peaks became evident. That is, oxygen loss allowed for nucleation and growth of pure ruthenium crystallites.

A final example is shown in Figure 6.4. Here a film was grown on a 200 °C sapphire substrate by electron-beam evaporation of Ru in the presence of an electron-cyclotron-resonance (ECR) oxygen plasma and was then annealed at 600 °C in an ECR oxygen plasma for 30 minutes. The film was tested in high vacuum for about a half day at temperatures in the range of 100 - 300 °C. The film lost oxygen and the xrd spectra therefore show that loss may also occur in RuO_2 films with lower defect contents. It needs to be emphasized, however, that only some of the RuO_2 films heated in vacuum lost oxygen. Other films did not, as evidenced by x-ray diffraction. Why some films lost oxygen and others did not is unclear. It is speculated that oxygen loss is associated with film defects, and in this context, free surfaces, grain-boundary surfaces, and film strain count as defects. It is also possible that film texture, and hence the shape of grains and grain boundaries, may be a factor in oxygen loss.

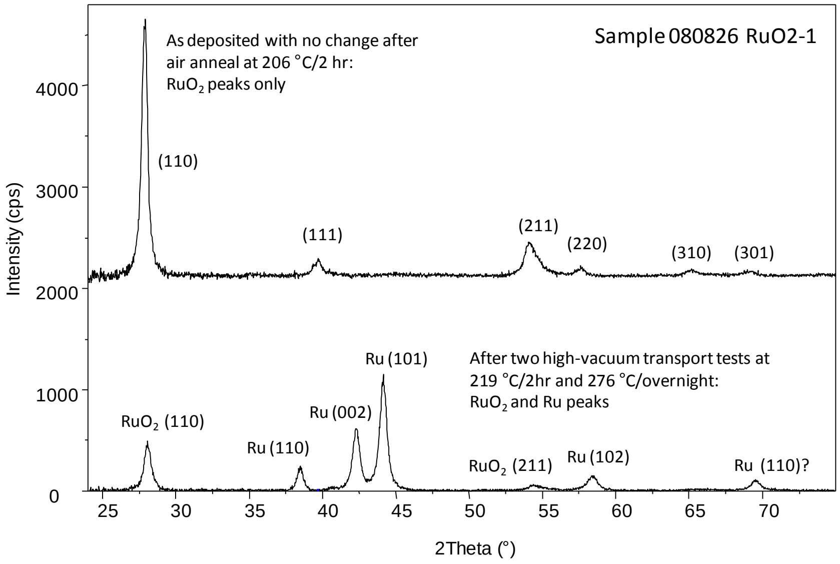

FIGURE 6.3. X-ray diffraction grazing-incidence scans on sample (080826-RuO2-1) grown by reactive magnetron sputtering at a high rate on a warm-substrate (3.5 Å/s, 100 °C) in a confocal deposition system. The upper trace made from the as-deposited film was unaltered by an air anneal at 206 °C for 2 hours. The lower trace shows the effects of heating in high vacuum for roughly one day.

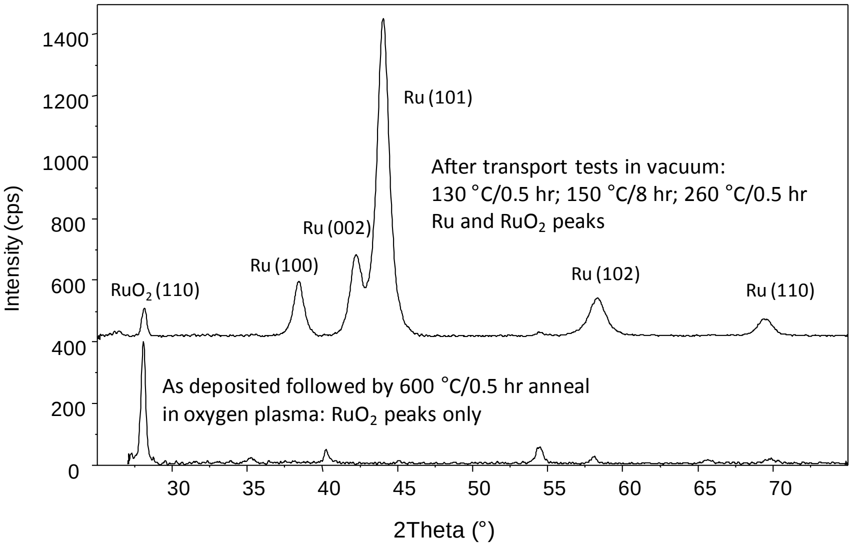

FIGURE 6.4. X-ray diffraction grazing-incidence scans made on a sample (080227-RuO2) grown on a 200 °C substrate by e-beam evaporation of Ru in the presence of an ECR oxygen plasma. The film was post-deposition annealed in the presence of an ECR oxygen plasma for 30 minutes at 600 °C.

6.4. Why a Phase Transformation Might Occur

Christian's book on the theory of phase transformations states that the first question to be considered is why a particular transformation might occur.[6] The answer lies in which equilibrium configuration of atoms in a solid has the lowest (most negative) binding energy or the highest (most positive) cohesive energy. Determining the correct configuration often involves a comparison of structures with energies that might differ by no more than a few percent.[7] The present paradigm for calculating the binding energy of ground-state structures is density functional theory (DFT), a method that employs the Khon-Sham equation to find the electron distribution that gives the lowest energy for a specified structure.[8] As of early 2011, it appears that no DFT calculations have been made on the RuO_2 system with regard to a progressive atom-by-atom oxygen loss.

As experimentally shown above, oxygen loss ultimately results in a phase transformation of individual crystallites from a tetragonal phase of RuO_2 to a hexagonal phase of pure Ru. Although the use of pair potentials is an empirical method and a Lennard-Jones style of equation for materials other than noble gases is, to quote Finnis, [8] "a very poor model indeed," this method allows a very rough comparison of the structural stability of non-stoichiometric versus stoichiometric RuO_2. The goal is to follow the methodology of Pettifor[7] to gain insight into structural stability, while recognizing that a transition-metal oxide like RuO_2 cannot, strictly speaking, be properly described by pair potentials. The following assumptions are made for a single crystallite of RuO_2:

1. A pair-potential model works on a 4d transition-metal oxide.
2. Bonds between ruthenium atoms are weak and may be neglected.[9]
3. All non-strain defects except oxygen vacancies may be neglected.
4. The structure is strain free.
5. The rutile tetragonal structure remains stable as oxygen atoms are removed (no sub-oxide formation).
6. First-order bond energy is a measure of structural stability.[7]

The pair-potential model is of the Lennard-Jones form with binding energy given by two terms. The first represents a repulsive energy and the second a bonding energy between a single pair of atoms

$$\frac{V}{E} = \left(\frac{R_h}{R}\right)^{n\lambda} - \left(\frac{R_h}{R}\right)^{n} \tag{6.3}$$

where V/E is the normalized potential energy, R_h is the position of zero potential, R is the distance between atoms, λ is the hardness of the potential, and n is the bonding exponent.[6] Figure 6.5 illustrates the form for the case of n = 2 with λ as a parameter. The comparison of structures is based on Pettifor's structural energy difference theorem,[7] which states that the energy difference ΔU between two competing structures is given to first order by the difference in bonding energies with repulsive energies made equal:

$$\Delta U = [\Delta U_{bond}]_{\Delta U_{rep=0}}. \tag{6.4}$$

When many atoms are involved, the bonding and repulsive terms in the pair-potential equation are modified by effective coordination numbers based on the arrangement of nearest neighbors:

$$U = Z_{rep}\left(\frac{R_h}{R}\right)^{n\lambda} - Z_{bond}\left(\frac{R_h}{R}\right)^{n} \tag{6.5}$$

where Z_{rep} and Z_{bond} are effective coordination numbers.

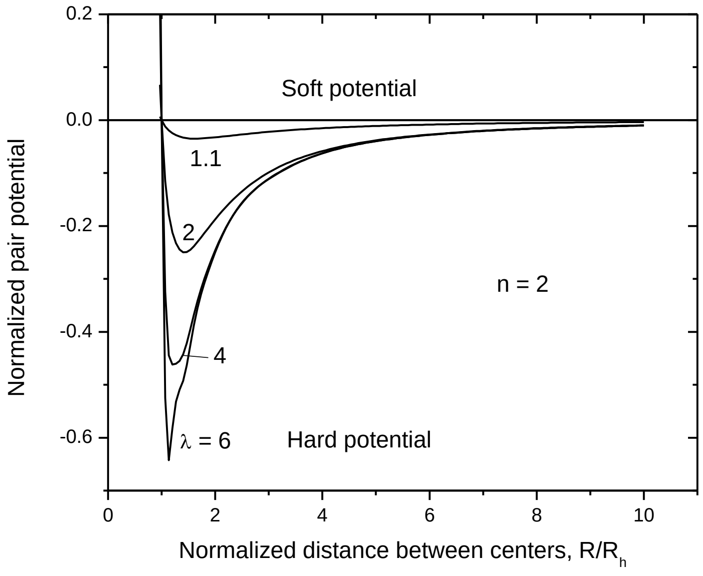

FIGURE 6.5. Normalized pair potential energy as a function of normalized distance between centers with a bonding exponent of 2 and hardness λ as a parameter (after Pettifor[7]).

The goal is to compare the stability of non-stoichiometric RuO_2 populated with oxygen vacancies to that of fully stoichiometric RuO_2. This may be done by taking the ratio of bond energies (non-stoichiometric to stoichiometric) determined by satisfying the structural energy difference theorem. If the ratio is less than one, then the non-stoichiometric structure is less stable and therefore more likely to undergo a phase transition. The method may be illustrated by comparing two four-atom planar structures: a line versus a square as shown in Figure 6.6. Which is the more stable structure?

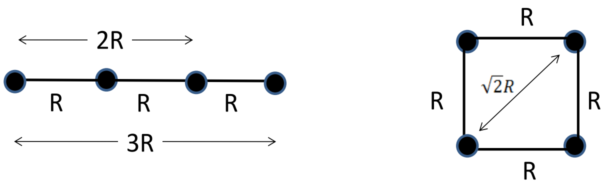

FIGURE 6.6 Illustration of the method: two simple four-atom structures used for a stability comparison.[7]

The binding energies of the two structures depend on the number of atom pairs and their spacing

$$U_{line} = 3V(R) + 2V(2R) + V(3R) \tag{6.6}$$

$$U_{square} = 4V(R) + 2V(\sqrt{2}R). \tag{6.7}$$

These algebraic forms allow for factorization of the radial terms to give effective coordination numbers.s

$$\begin{aligned}\frac{U_{line}}{E} &= \left[3 + \frac{2}{(2)^{n\lambda}} + \frac{1}{(3)^{n\lambda}}\right]\left(\frac{R_h}{R}\right)^{n\lambda} - \left[3 + \frac{2}{(2)^{n}} + \frac{1}{(3)^{n}}\right]\left(\frac{R_h}{R}\right)^{n} \\ &= \left[Z^l_{rep}\right]\left(\frac{R_h}{R}\right)^{n\lambda} - \left[Z^l_{bond}\right]\left(\frac{R_h}{R}\right)^{n}\end{aligned} \tag{6.8}$$

$$\begin{aligned}\frac{U_{square}}{E} &= \left[4+\frac{2}{\left(\sqrt{2}\right)^{n\lambda}}\right]\left(\frac{R_h}{R}\right)^{n\lambda} - \left[4+\frac{2}{\left(\sqrt{2}\right)^{n}}\right]\left(\frac{R_h}{R}\right)^{n} \\ &= \left[Z_{rep}^{s}\right]\left(\frac{R_h}{R}\right)^{n\lambda} - \left[Z_{bond}^{s}\right]\left(\frac{R_h}{R}\right)^{n}\end{aligned} \tag{6.9}$$

The superscripts *l* and s on the effective coordination numbers refer to line and square respectively.

At this point the structural energy difference theorem is applied by setting the repulsive energies equal while using the square as the reference structure. That is, the line-bond-distance ratio is written in terms of the square-bond-distance ratio using the effective coordination numbers as the adjustment factor.

$$\left[Z_{rep}^{l}\right]\left(\frac{R_{h,l}}{R_l}\right)^{n\lambda} = \left[Z_{rep}^{s}\right]\left(\frac{R_{h,s}}{R_s}\right)^{n\lambda} \tag{6.10}$$

$$\left(\frac{R_{h,l}}{R_l}\right) = \left(\frac{R_{h,s}}{R_s}\right)\left(\frac{Z_{rep}^{s}}{Z_{rep}^{l}}\right)^{\frac{1}{n\lambda}} \tag{6.11}$$

The next step is to compare bond energies by making a ratio of the bond energy of the line to the bond energy of the square.

$$\frac{U_{bond,l}}{U_{bond,s}} = \left(\frac{-Z_{bond}^{l}}{-Z_{bond}^{s}}\right)\frac{\left(\frac{R_{h,l}}{R_l}\right)^{n}}{\left(\frac{R_{h,s}}{R_s}\right)^{n}} \tag{6.12}$$

$$\frac{U_{bond,l}}{U_{bond,s}} = \left(\frac{-Z_{bond}^{l}}{-Z_{bond}^{s}}\right)\frac{\left(\frac{R_{h,s}}{R_s}\left(\frac{Z_{rep}^{s}}{Z_{rep}^{l}}\right)^{\frac{1}{n\lambda}}\right)^{n}}{\left(\frac{R_{h,s}}{R_s}\right)^{n}} = \left(\frac{Z_{bond}^{l}}{Z_{bond}^{s}}\right)\left(\frac{Z_{rep}^{s}}{Z_{rep}^{l}}\right)^{\frac{1}{\lambda}} \tag{6.13}$$

This shows that the stability of the line relative to the square depends on the ratios of the bonding and repulsive coordination numbers and the hardness of the potential but not on the bonding exponent n. Using the Lennard-Jones potential reveals that the bond energy of the line is 83 % of that of the square and is therefore a less stable structure, as might be guessed intuitively.

Now applying the same procedure to model oxygen loss in RuO_2, the bonding energy can be written as a function of the number of atoms in a unit cell, m; the bonding exponent, n; and the hardness, λ. The bond energy ratio in terms of effective coordination numbers follows as

$$\frac{U_{bond}(m,n,\lambda)}{U_{bond}(6,n,\lambda)} = \frac{Z_{bond}(m,n,\lambda)}{Z_{bond}(6,n,\lambda)}\left[\frac{Z_{rep}(6,n,\lambda)}{Z_{rep}(m,n,\lambda)}\right]^{\frac{1}{\lambda}} \tag{6.14}$$

where six oxygen atoms have been assigned to the central unit cell reflecting the octahedral coordination of each ruthenium atom by six oxygen atoms, and m is an integer less than 6. Note that two of the six oxygen atoms are internal to the unit cell and four are on opposite cell faces. The distribution of ruthenium nearest neighbors to the six oxygen atoms in terms of the lattice constant a (4.499 Å) is given in Table 6.1.

TABLE 6.1. Distribution of Ru nearest neighbors to 6 unit-cell oxygen atoms.

Nearest neighbor position	Number of Ru neighbors	Distance in terms of unit cell
1st	6	0.433a
2nd	12	0.444a
3rd	12	0.759a
4th	12	0.822a
5th	24	0.900a
6th	6	0.982a
7th	24	1.031a
8th	8	1.083a

An interesting property of the rutile structure is that the numbers of the first seven nearest neighbors are integer multiples of the six oxygen atoms in the unit cell. To show what this means practically, consider the bond energy ratio for the loss of one oxygen atom in terms of the first two nearest neighbors. The bonding and repulsive effective coordination number ratios reduce to the simple forms

$$\frac{Z_{bond}(5,n,\lambda)}{Z_{bond}(6,n,\lambda)}=\left[\frac{\frac{5}{0.433^n}+\frac{10}{0.444^n}}{\frac{6}{0.433^n}+\frac{12}{0.444^n}}\right]=\frac{5}{6} \tag{6.15}$$

$$\frac{Z_{rep}(6,n,\lambda)}{Z_{rep}(5,n,\lambda)}=\left[\frac{\frac{6}{0.433^n}+\frac{12}{0.444^n}}{\frac{5}{0.433^n}+\frac{10}{0.444^n}}\right]^{\frac{1}{\lambda}}=\left(\frac{6}{5}\right)^{\frac{1}{\lambda}} \tag{6.16}$$

because of the factorization allowed in both the numerators and denominators of these expressions. Then up to the seventh nearest neighbor, equation (6.14) reduces to an expression that depends only on the hardness of the potential

$$\frac{U_{bond}(m=5,n,\lambda)}{U_{bond}(6,n,\lambda)}\cong\frac{5}{6}\left(\frac{6}{5}\right)^{\frac{1}{\lambda}}. \tag{6.17}$$

The bond energy ratio as a function of the number of oxygen atoms with hardness as a parameter is presented in Figure 6.7. The general trend is a weakening of stability as the unit cell becomes less stoichiometric due to oxygen loss. The pair potential model of this study implies that as the hardness of the potential increases (deeper wells), oxygen loss becomes more destabilizing to the overall structure. Of course this may not be true due to the assumptions of the model, but the key point is that as RuO_2 films lose oxygen, their binding energy becomes less negative and they become more prone to transforming back to the parent metal, an experimental result that was observed in this study.

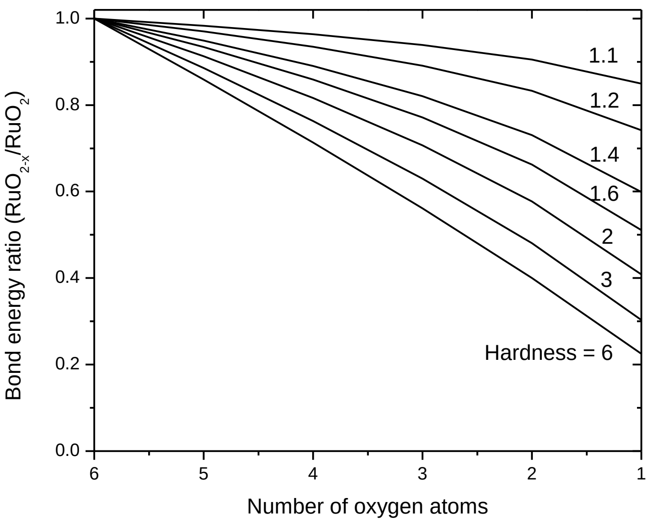

FIGURE 6.7. Bond energy ratio as a function of the number of oxygen atoms in a unit cell of RuO_2 with hardness of the potential as a parameter. Oxygen loss is more destabilizing as the hardness increases.

6.5. How a Phase Transformation Might Occur

Christian's book on the theory of phase transformations states that the second question to be considered is how a particular transformation might occur.[6] Heterogeneous phase transformations from one chemical composition (RuO_2) to another (Ru) depend on the presence of defects, strain energy, and surface energy, as well as free energy differences between the initial and final structures. The transformation requires the presence of nucleation sites and is governed by solid-state diffusion (chemical kinetics). In defective films with small grain sizes, for example, the grain boundary diffusion of oxygen atoms out of a film will be more rapid than that of ruthenium atoms due to different atomic sizes, possibly causing an aggregation of ruthenium atoms on boundaries and a subsequent phase change driven by binding energy differences from the tetragonal structure of RuO_2 to the hexagonal-close-packed structure of Ru. It is difficult to pinpoint the mechanism of transformation, but it is hypothesized that the mechanism is related to the presence of defects, including surfaces and film strain as defects.

An interesting approach to calculating the formation energies of rutile metal oxides is given by Martinez et al.,[10] where formation energies are broken into two parts. The first part is the deformation energy due to stretching of the bulk metal lattice to allow entrance of oxygen atoms, and the second part is the bonding energy associated with oxygen atoms that have entered. The deformation energy per atom of the lattice is defined as

$$G_{deform} = E_{bulk}^{expanded} - E_{bulk}^{pure} \tag{6.18}$$

where $E_{bulk}^{expanded}$ is the energy per metal atom of the rutile structure without oxygen atoms and E_{bulk}^{pure} energy per metal atom in the pure metal bulk crystal (hcp structure for Ru). The deformation energy per atom of ruthenium is found to be about 3.8 eV;[10] that is, each Ru atom in a tetragonal lattice without oxygen has associated with it an additional 3.8 eV above the binding energy of the lattice. The system is unstable, and given an external perturbation, strain energy may be sufficient to drive a phase transformation from the tetragonal to the hexagonal-close-packed structure.

6.6. Hall Coefficient Phase Diagram

It is possible to formulate a phase diagram that relates the Hall coefficient at room temperature in the low-field condition ($\omega\tau << 1$) to the composition of sub-stoichiometric RuO_2. Such a diagram is presented in Figure 6.8 where it is shown that the dominant charge carrier type must change from electrons in n-type ruthenium dioxide to holes in p-type ruthenium as oxygen is lost from ruthenium dioxide crystallites. The crossover from n- to p-type behavior is likely to take place in the range from 33.3 to approximately 37 atomic percent Ru based on x-ray photoelectron spectroscopy measurements of sample 080827-RuO2 (e-beam evaporation of Ru with ECR oxygen plasma and annealed at 600 °C for 30 minutes in an ECR oxygen plasma). Ruthenium is a compensated metal where the concentration of electrons equals that of holes and is p-type because hole mobility exceeds electron mobility. Ruthenium dioxide is an n-type metal. If it is also a compensated metal like ruthenium, then it is one with electron mobility greater than hole mobility. Note that the Hall coefficient for Ru is unchanged[13] and that for RuO_2 is increased[14] from -11 to -8x10^{-5} cm^3/C as temperature is lowered from 300 to 77 K.

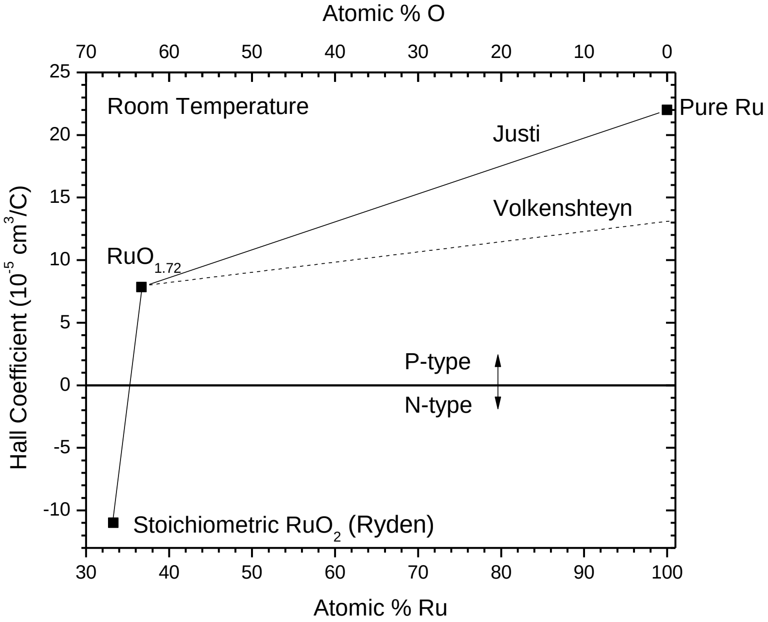

FIGURE 6.8. Hall coefficient phase diagram for the ruthenium-oxygen system at room temperature and in the low-field condition. Loss of oxygen results in a change in dominant charge carrier type from electrons in stoichiometric RuO_2 to holes in pure Ru. The lines labeled Justi[12] and Volkenshteyn[13] indicate the probable range of the Hall coefficient of Ru. The stoichiometric RuO_2 point was taken from Ryden.[14]

A question to ask is what causes the change of dominant charge carrier type from electrons to holes as oxygen is lost from RuO_2. A speculative answer to this question is that the nucleation and growth of a ruthenium phase forms a two-phase system consisting of individual Ru and RuO_2 crystallites. A progressive loss of oxygen would then result in a continual growth of the Ru phase at the expense of the RuO_2 phase. At some point the transport properties of the Ru phase overwhelm the RuO_2 phase in the composite film with holes becoming the dominant carriers. According to the phase diagram, the changeover to p-type behavior takes place at approximately 35 atomic percent ruthenium.

One might think that as oxygen is lost in a single-phase RuO_2 film, the film would gain conduction electrons via the type of defect doping seen in metal-oxide semiconductors such as TiO_2. The unbound electrons freed by chemical reduction of the oxide should increase the conduction electron concentration in the film, which would therefore become more strongly n-type. However, observations indicate a trend from n-type to p-type behavior with oxygen loss, as would be shown by a line with a positive slope starting at the stoichiometric RuO_2 point. There was no evidence of changes from n-type behavior to a more negative n-type behavior in any of the films investigated except for a single case, which was a RuO_2 film grown by normal-incidence sputtering and heated for 46 hours in CO (see section 7.10).

In summary, evidence indicates that progressive oxygen loss from RuO_2 films deposited by the techniques of this study ultimately results in a two-phase mixture of Ru and RuO_2 with a subsequent change from n-type to p-type conduction. It is conjectured that the mechanism of oxygen loss is related to point and extended defects, non-stoichiometric surfaces, and film strains. It is likely that oxygen loss can be lessened or possibly eliminated by air or oxygen anneals prior to vacuum tests, but this is experimentally unproven.

---

[1] V. E. Henrich and P. A. Cox, *The Surface Science of Metal Oxides*, (Cambridge, 1994).

[2] W.E. Bell and M. Tagami, J. Phys. Chem. 67, No. 11, 2432 (1963).

[3] B. Brunetti, P. Scardala and V. Piacente, Matls. Chem. Phys. 83, 145 (2004).

[4] E. H. P. Cordfunke, R. J. M. Konings, E. F. Westrum, Jr. and R. Shaviv, J. Phys. Chem. Solids 50, 4, 429 (1989).

[5] R. A. Swalin, *Thermodynamics of Solids*, (Wiley, New York, 1972).

[6] J. W. Christian, *The Theory of Transformations in Metals and Alloys*, (Pergamon, Oxford, 1965).

[7] D. G. Pettifor, *Bonding and Structure of Molecules and Solids*, (Clarendon, Oxford, 2002).

[8] M. W. Finnis, *Interatomic Forces in Condensed Matter*, (Oxford, 2003).

[9] K. Murai, Y. Akune, Y. Suzuki, T. Moriga and I. Nakabayashi, Int. J. Mod. Phys. B, 20, Nos. 25, 26 &27, 4111 (2006).

[10] J. I. Martinez, H. A. Hansen, J. Rossmeisl and J. K. Norskov, Phys. Rev. B 79, 045120, (2009).

[11] C. M. Hurd, *The Hall Effect in Metals and Alloys*, (Plenum, New York, 1972).

[12] E. Justi, Zeitschrift fur Natufurschung, 4a, 472 (1949).

[13] N. V. Volkenshteyn, V. A. Novoselov, V. Ye. Startsev and Ye. P. Romanov, Phys. Met. and Metallography 33, 6, 105 (1972).

[14] W. D. Ryden, A. W. Lawson and C. C. Sartain, Phys. Rev. B 1, 1494 (1970).

Chapter 7

TRANSPORT EFFECTS CAUSED BY SURFACE REDOX REACTIONS

7.1. Chapter Abstract

Transport properties of planar and nanorod-structured ruthenium dioxide and ruthenium thin films were measured in reducing and oxidizing atmospheres by exposing films to CO and O_2 at various pressures. The experiments were performed because, although Ru and RuO_2 are well studied catalysts supported by a large literature,[1-7] little if any attention has been paid to the effects of reduction-oxidation (redox) reactions on the transport properties of these metals. The key reaction is the oxidation of carbon monoxide to carbon dioxide ($CO + ½ O_2 \rightarrow CO_2$) over Ru and RuO_2 surfaces. To the best of our knowledge, no one else has measured charge transport properties during these reactions and the work that follows is believed to be unique. Note that the chapter is organized as a series of experimental observations followed at the end by interpretation of those observations.

7.2. Background Information

The main purpose of the work was to investigate the resistivity and Hall coefficients of RuO_2 polycrystalline films during exposure to CO and O_2 gases. Another purpose was to determine how the sign of the dominant charge carriers would be affected by surface redox reactions. A third purpose, recognized after the experiment began, was to investigate the stability of RuO_2 films under reducing atmospheres in light of observed oxygen loss from the films.

Given the large body of work devoted to catalysis on Ru and RuO_2 surfaces, it might appear that research in this area is largely complete. Surprisingly, that is not the case and there are still open questions that affect the interpretation of results. The following quote from Seitsonen and Over[8] nicely summarizes the state of knowledge in 2009. "A sustaining but unaccomplished dream of theorists is to be predictive. To be honest, even for the simple CO oxidation reaction this ultimate goal of theory is still out of reach." The main issue from the viewpoint of catalysis seems to be the so-called "pressure gap" with regard to ruthenium.[6-7, 9] Of the platinum group metals, Ru is the least reactive toward CO oxidation under UHV conditions but the most reactive at higher pressures (≈ 1 torr) and lower temperatures (≤ 450 K).[9] Strong arguments have been made that the formation of catalytic RuO_2 from Ru at high pressures explains the gap,[2] but counterarguments state that catalysis in certain pressure-temperature ranges may be due to a chemisorbed oxygen phase on ruthenium surface steps.[9-10] For the temperatures (20 - 250°C) and pressures (1 - 5 torr) considered in this study, the chemisorbed-oxygen-phase hypothesis appears to be more consistent with the results, because after exposure to pure CO causing reduction of RuO_2 to Ru, followed by exposure to pure O_2, the RuO_2 phase was not generally re-established. That is, it has been found that the oxidation of Ru back to RuO_2 requires temperatures above 500 K, which was near the upper limit of temperatures available in the experimental apparatus.[5]

As stated above, the primary goal of the experiments performed in this study was to see if changes in surface chemistry (including grain boundary surfaces) by catalysis would affect transport properties. As shown by data presented in the remainder of the chapter, several significant findings were made: (i) the occurrence of a large resistivity increase in RuO_2 films upon first exposure to pure CO at temperatures in the range of 100 to 200 °C, (ii) the observation of gas-switched resistivity changes in all films subjected to long exposures to CO and the subsequent development of resistivity hysteresis loops, and (iii) the phase change, erosion, and breakup of films caused by oxygen loss and film stress. The occurrence of gas-switched resistivity hysteresis loops appears to be related to pure ruthenium and possibly to a physical breakup of the films and the formation of increased surface areas. Perhaps the most surprising finding is that flat- and nanorod-structured RuO_2 films were unstable in CO over the range of temperatures and pressures considered in the experiment.

7.3. Rationale for Choice of P-T Parameter Space

The pressures and temperatures used in the experiment were chosen in part to match other studies and in part by limitations of the measurement apparatus. As pointed out in Chapter 6, some of the RuO_2 films were observed to lose oxygen under high vacuum conditions ($\approx 10^{-5}$ torr). Thus, higher pressures were chosen to maintain RuO_2 phase stability. The available mass flow controllers were configured for relatively high flows, which would quickly drain the small CO gas bottle that was required to fit inside the safety enclosure. Thus, measurements were made in static CO to prevent bottle drainage in experiments over several days. The available platinum heater could not raise sample temperatures safely above 250 °C (523 K). Thus, temperatures were kept below 250 °C to preserve the heater. In addition to the stability and equipment constraints, it was noted that practical catalysis usually involves higher rather than lower pressures (i.e., about 1 atmosphere versus UHV). The choice of pressures from 1 to 5 torr and temperatures from 20 to 250 °C was well suited to address the pressure gap of ruthenium and the parameter spaces examined by other investigators.

7.4. Sample Matrix

Three types of films were investigated. These may be classified by the angle of incidence as illustrated in Chapter 3: glancing-angle, confocal, and normal-incidence deposition. GLAD films were emphasized because of the large surface areas available with their nanorod-structured morphologies. Table 7.1 lists the parameters of the films, all of which were grown on amorphous fused-quartz substrates. Note that GLAD film thicknesses are from the substrate to top of nanorods, since the effective thickness of films in the nanorod geometry is difficult to ascertain.[11] Thicknesses were measured by quartz-crystal microbalances, x-ray reflectivity, profilometry, and SEM elevation views.

TABLE 7.1. Deposition parameters for samples used in reduction-oxidation gas tests.

Sample	**Metal**	**Method**	**Base P** (μtorr)	**Dep P** (mtorr)	**Sub T** (°C)	**Power** (W)	**Rtn** (rpm)	**Time** (s)	**Thk** (Å)	**Rate** (Å/s)
017-10	RuO_2	GLAD	0.38	3	RT	100 dc	5	2369	2800	1.2
019-10	RuO_2	GLAD	0.32	3	190	100 dc	5	2036	2300	0.74
023-10	RuO_2	GLAD	0.29	3	460	100 dc	5	2373	2500	1.1
042-09	Ru	GLAD	0.19	3	RT	80 dc	5	1518	790	0.5
061-10	RuO_2	GLAD	0.11	3	RT	100 dc	5	2370	2800	1.2
064-10	RuO_2	Normal	0.18	3	RT	100 dc	0	1420	1500	1.1
090910-RuO2-1	RuO_2	Confocal	1	2.6	16	500 rf	14	420	1360	3.2
090910-RuO2-2	RuO_2	Confocal	1	2.6	16	500 rf	14	420	1360	3.2

<u>Key:</u>
Base P = base pressure
Dep P = deposition pressure
Sub T = substrate temperature
Rtn = substrate rotation
dc = direct current
rf = radio frequency
Thk = film thickness
RT = room temperature (unheated)

7.5. Assumption of a Slab Model

Before discussing the results, a note of caution is in order due to the physical degradation of the films in the reducing CO atmosphere. Implicit in all resistivity and Hall measurements is the assumption of a slab model where the slab is simply connected and has a uniform thickness.[12-13] Holes and thickness variations caused by CO reduction developed in the films and, as a result, the underlying assumption of a slab configuration is not strictly valid. This is an issue for the films subjected to longer-term CO exposures that were measured in days. It is perhaps best to regard the resistivity results after multiple heat cycles as more indicative of physical changes in the films rather than as absolute resistivity measurements. The physical degradation of the films complicates the uncertainty in thickness already inherent in nanorod films due to the lack of a non-slab geometry.[11]

7.6. Stability of RuO_2 Films in an Oxidizing Environment

After deposition, all of the RuO_2 films were stored in air at one atmosphere for several months to years. No measureable changes in the room-temperature transport properties of the films were observed, and no visible changes to the film compositions or morphologies were apparent over this time. The observed stability of RuO_2 in an oxidizing environment of room-temperature air is consistent with reports from other investigators.[14-15] However, as will be shown below, even an exposure to a small amount of carbon monoxide brings about irreversible changes in the resistivity under certain conditions of temperature and pressure. The irreversibility may have been caused by the high defect content in some films due to deposition conditions. For example, many films were grown at high deposition rates on cold substrates, an approach which guarantees a high defect content by limiting the activation energy available for surface diffusion.

7.7. Film Annealing Prior to Transport Tests

When certain films grown either by glancing-angle or confocal deposition were heated above room temperature the first time in a static CO atmosphere, the resistivity underwent a significant increase that was not reproduced in subsequent heat cycles. A confounding factor for the measurement in CO was the frequent initial fall in resistivity due to defect annealing, irrespective of the annealing environment.[16-17] To counter this effect, some films were heated in air or oxygen prior to transport tests to allow defect annihilation and to separate the annihilation effect from the gas effect. Furthermore, it was noted that the characteristic time scales of the two effects were different. Measurements from 20 to 250 °C indicated that the characteristic times of defect annealing were hundreds of minutes, whereas those of the CO-induced response at 1-to-5 torr were tens of minutes. However, a dilute mixture of 96 ppm CO in 28 torr air did cause a slower response in resistivity upon heating that occurred on time scales comparable to defect annealing as will be shown in the next section.

7.8. Resistivity Response on First Heating in a Carbon Monoxide Atmosphere

Figure 7.1 plots resistivity changes in nanorod sample 019-10 during defect annealing under exposure to 96 ppm CO in 28 torr air. (In the following discussion, the word “point” refers to laboratory notebook entries.) Point 17, which shows the effects of defect annealing, was reached after approximately 24 hours and point 28 after approximately 44 hours. When the system was held at 247 °C (520 K) in the air-CO mixture for 24 hours, resistivity rose by 15 percent from point 28 to point 40. These data show that prolonged exposure to 3 millitorr CO in 28 torr air increased film resistivity, but on a significantly longer time scale than exposure to pure 4 torr CO, as will be demonstrated below. When the film was cooled and reheated in air, resistivity showed a linear response with temperature that is characteristic of a metal (points 42 to 46).

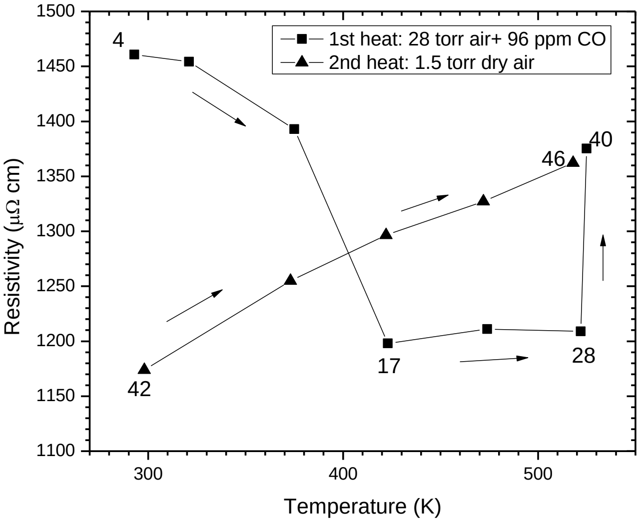

FIGURE 7.1. Resistivity as a function of temperature with atmosphere as a parameter for RuO_2 nanorod sample 019-10. Heating in a mixture of 28 torr dry air and 3 millitorr CO took place over 44 hours (points 4 to 28). Points 28 to 40 show the rise in resistivity due to CO exposure at 520 K over 24 hours. The sample was then cooled to 293 K and heated a second time in 1.5 torr dry air (points 42 to 46).

For the record, it is noteworthy that sample 019-10 was a 2.54 cm square film. For measurements of resistivity, voltage and current pins were not on the outside edge of the sample and a correction factor was required. The factor was determined when the transport test series was completed by scribing a circle of the correct van der Pauw geometry in the center of the square and then re-measuring the room temperature resistivity with the proper geometry. These resistivity data were then multiplied by the resulting correction factor of 1.432.

The sample was then cooled again to room temperature and reheated in 1.6 torr CO to 101 °C (374 K), which is shown as point 60 in Figure 7.2. At point 60, the pressure was raised to 5 torr CO and then the temperature was raised to 153 °C (426 K). While heating, an increase in resistivity was observed as the sample temperature approached 153 °C (point 61). The resistivity continued to rise and then fell in an exponential behavior as can be seen in Figure 7.2 by looking at points 61 to 82; peak resistivity at point 65 was about 30 percent higher than that of point 60. The resistivity increase was probably a continuation of the gas-induced process shown by points 28 to 40 in Figure 7.1, which was incomplete. One possible explanation for the resistivity response is the formation and escape of CO_2 from film base-layer grain boundaries, which could lead to an exponential growth and fall of resistivity by changing grain-boundary electron reflection coefficients.

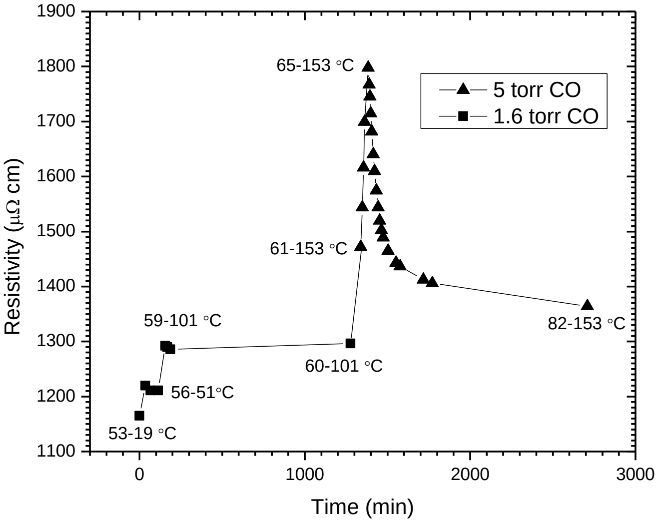

FIGURE 7.2. Resistivity as a function of time for RuO_2 nanorod sample 019-10 in pure CO. The pressure was increased from 1.6 to 5 torr at point 60 before the temperature was ramped up to 153 °C (426 K).

Another more dramatic example of CO-induced resistivity changes is shown in Figure 7.3 where a RuO_2 sample with nanorod geometry (017-10) and no initial anneal in air or oxygen was heated in 5 torr of pure CO from 50 to 102 °C (323 to 375 K), with the result that the resistivity increased by more than a factor of three. The time between measurement of points 2 and 3 was approximately 16 hours. With continued heating, the resistivity fell by roughly a factor of eight over a 24 hour period (points 3 to 7). Further heating led to a minimal change in resistivity (points 7 - 13).

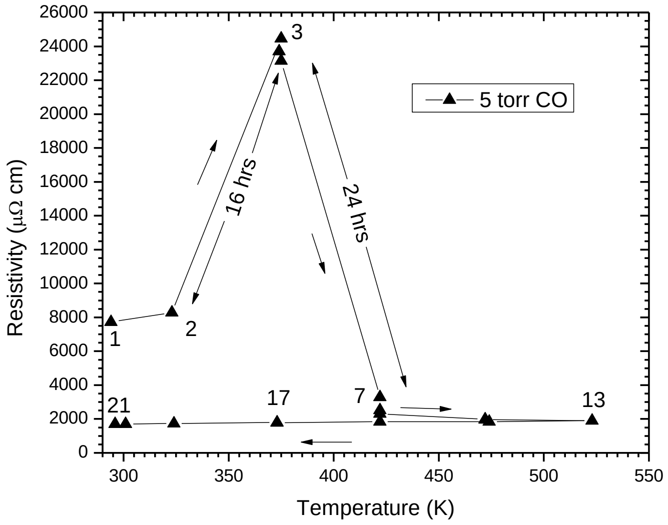

FIGURE 7.3. Resistivity as a function of temperature for RuO_2 nanorod sample 017-10 heated the first time in carbon monoxide at a pressure of 5 torr. The film was not pre-annealed in either air or oxygen.

An additional example of a CO-induced resistivity increase is shown in Figure 7.4 for a nanorod film grown under identical deposition conditions to sample 017-10, but heated first in pure oxygen to 250 °C and held overnight at that temperature. By switching from O_2 to CO exposure, the resistivity increased by a factor of two.

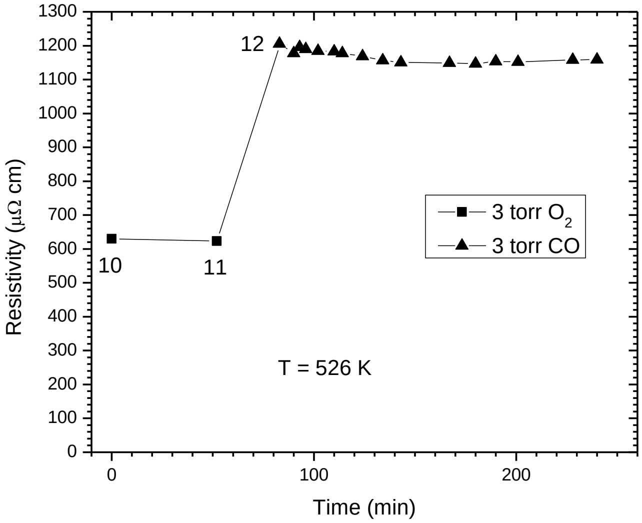

FIGURE 7.4. Resistivity as a function of time for RuO_2 nanorod sample 061-10 first heated in oxygen to 526 K (253 °C) at 3 torr for 18 hours: points 10 and 11 show the end of that interval. When the atmosphere was switched to CO at point 11, resistivity was increased by a factor of two over 30 minutes (points 11 - 12). The sample was identical to 017-10.

The responses in Figures 7.2 - 7.4 were irreversible in the sense that additional exposures to O_2 and CO did not reproduce the exponential rise and fall of resistivity regardless of the duration of CO exposure. The irreversibility implies permanent structural changes, which is consistent with the results of Gao et al.,[9] who also observed structural changes and found that “under stoichiometric and reducing reaction conditions RuO_2 gradually converts to a surface oxide and then to a chemisorbed oxygen phase between 400 and 600 K.”

Lest it be thought that the CO-induced response was confined to RuO_2 film morphologies with large surface areas (i.e., nanorods), Figures 7.5 and 7.6 show that it was also possible to get large changes in the resistivity of planar RuO_2 films. Figure 7.5 shows the resistivity versus temperature during the first heating of a planar RuO_2 film in air for 50 hours. The familiar fall in resistivity due to defect annealing is seen (points 1 to 10) and is followed by the linear cooling curve that is a characteristic of a metal (points 12 to 18). Figure 7.6 shows that the same film undergoes an order-of-magnitude change in resistivity when first heated in 4 torr CO, which was the largest change in resistivity observed in this study. It is speculated that the lack of a significant exponential decay in resistivity over the 5 hour period after the peak was reached (point 51) is due to CO_2 trapped along grain boundaries of the planar film. That is, the escape path of CO_2 from interior grain boundaries to the film surface is longer in planar-structured films than in nanorod-structured films.

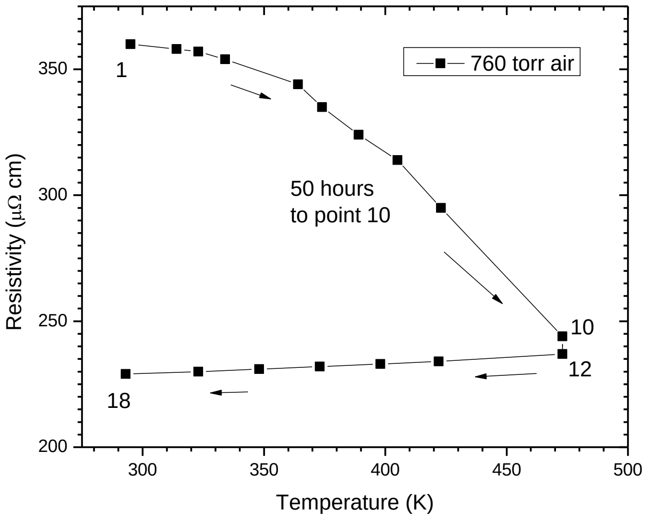

FIGURE 7.5. Resistivity as a function of temperature in air at one atmosphere during the first heating of planar RuO_2 sample 090910-RuO2-1. The top curve shows the fall in resistivity due to defect annealing and the bottom curve shows the linear behavior expected for a metal.

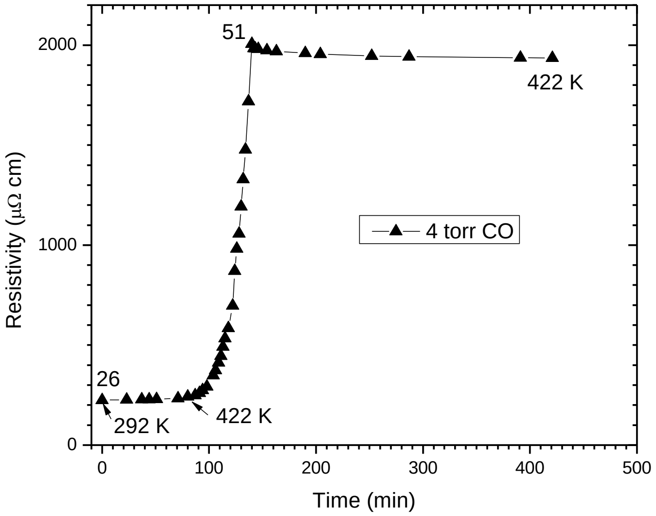

FIGURE 7.6. Resistivity of planar sample 090910-RuO2-1 as a function of time in 4 torr CO as temperature is raised from 292 K (19 °C) to 422 K (150 °C) and held constant. The temperature reached 422 K after approximately 80 minutes (1.6 °C/min ramp rate).

The resistivity of a pure ruthenium nanorod-structured film was also changed on the first exposure to carbon monoxide as shown in Figure 7.7. The film was heated in O_2 from room temperature to 522 K . At point 11, the atmosphere was switched from O_2 to CO with a rise in resistivity over 25 minutes to point 12. The CO-induced gas response, therefore, was not restricted to RuO_2 samples, and it may be inferred that the presence of ruthenium metal is the common factor. The steep fall in resistivity between points 19 and 20 may represent the full release of CO_2 from the ultra-thin base-layer grain boundaries over a period of about 4 hours. The fall in resistivity from points 25 to 29 is due to a lowering of heater power and a subsequent drop in temperature.

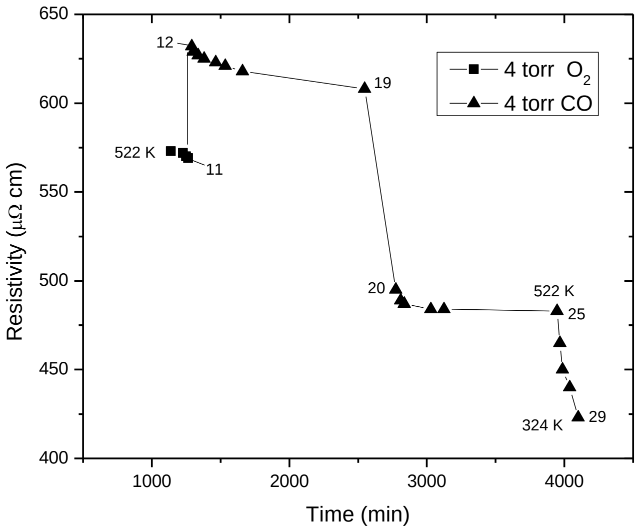

FIGURE 7.7. Resistivity as a function of time for Ru nanorod sample 042-09 in O_2 and CO environments. The film was heated in 4 torr O_2 from 293 K to 522 K. The atmosphere was then switched to 4 torr CO at point 11.

A planar RuO_2 film grown by conventional normal-incidence dc magnetron sputtering with no prior annealing (sample 064-10) did not show a resistivity gas response when first heated in carbon monoxide. This is in contrast to the films mentioned above that were grown either by dc glancing-angle or radio-frequency confocal magnetron sputtering. Resistivity versus temperature over a two day period is shown in Figure 7.8. The normal incidence film, however, was severely degraded by exposure to carbon monoxide and the resistivity became infinite (point number 28). Upon removal from the test fixture, visual inspection of the film showed it to be almost completely transparent. It is interesting to note that despite the optical change, the resistivity did not change by more than about 20 percent over the course of the test.

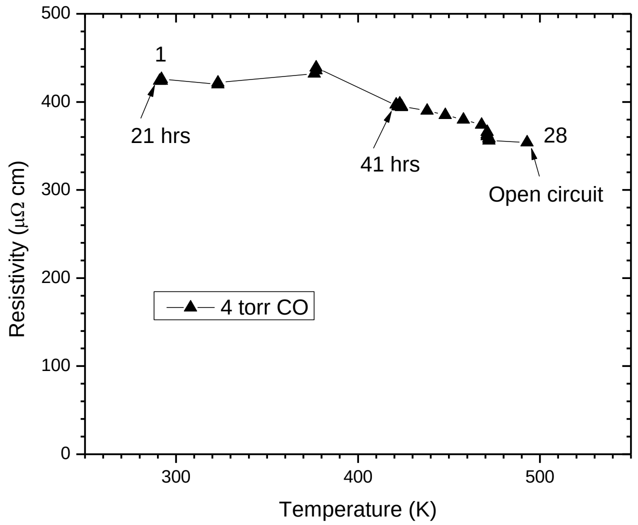

FIGURE 7.8. Resistivity as a function of temperature during the first heating in 4 torr CO of planar RuO_2 film 064-10 grown by normal-incidence magnetron sputtering. The sample was held at room temperature for 21 hours in CO before heating. Total exposure time to CO was 49 hours.

7.9. Switching of Resistivity Caused by Gas Exposure

After the RuO_2 samples of Table 7.1 had been thermally cycled a number of times, it became clear that the magnitude of the resistivity could be switched up or down by switching the atmosphere between oxygen and carbon monoxide. Thermal cycles gave rise to resistivity hysteresis loops when the atmosphere on a temperature up-ramp differed from the atmosphere on a temperature down-ramp. Examples of the resulting hysteresis loops are shown in Figure 7.9, where it is seen that resistivities on the 7th through 9th heat cycles of nanorod sample 019-10 change as much as 30 percent as a function of the atmosphere.

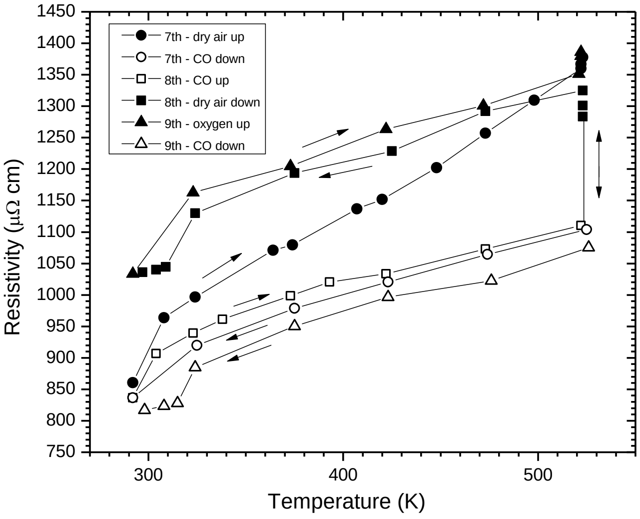

FIGURE 7.9. Resistivity as a function of temperature during up and down heat ramps of RuO_2 nanorod sample 019-10 in different gas environments. Exposures were to dry air, O_2, and CO at 4 torr. Ramp times varied from about 3 to 20 hours. Arrows indicate the direction of heating or cooling.

Figure 7.10 compares gas-switched hysteresis loops on the fourth thermal cycle for two RuO_2 nanorod-structured films grown with contrasting substrate temperatures of 16 and 460 °C. The lower deposition substrate temperature raised the overall resistivity of sample 017-10 relative to sample 023-10 by roughly a factor of four (subject to the caveat that the slab model of resistivity may not apply after multiple heat cycles). Both films developed loops, from which it may be inferred that the development of loops is independent of substrate temperature. It appears that films with higher defect contents, in this case the film with the 16 °C substrate, yield the largest hysteresis loops.

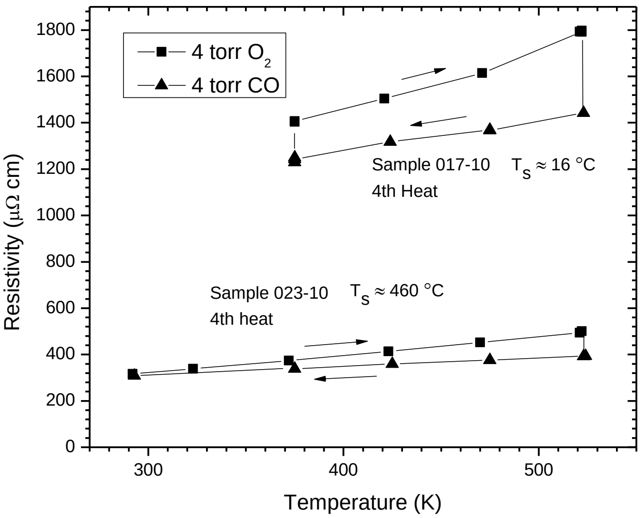

FIGURE 7.10. Resistivity as a function of temperature during the 4th heating and cooling cycles of RuO_2 nanorod samples 017-10 and 023-10, which were grown at respective substrate temperatures of 16 and 460 °C. Exposures were to 4 torr O_2 and CO. The time between measurement points varied but was roughly one hour.

Figure 7.11 shows two grazing-incidence x-ray diffraction scans of RuO_2 sample 017-10, one immediately after deposition and another after the fourth heat cycle in O_2 and CO atmospheres. Prior to the fourth cycle, the cumulative exposure to both gases was over a period of several days. It is evident that the film underwent a phase change from rutile tetragonal RuO_2 to hexagonal-close-packed Ru. That is, RuO_2 was completely reduced to Ru upon long exposures to CO at the temperatures and pressures applied in this experiment. Based on Figure 7.11, it seems likely that catalysis on the surfaces of ruthenium metal is the source of the gas-switched resistivity hysteresis loops. This reduction of RuO_2 upon CO exposure is an observation that is consistent with the findings of Gao.[9]

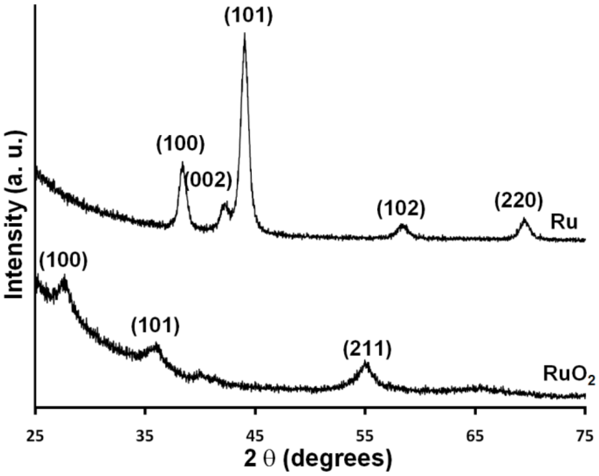

FIGURE 7.11. Grazing incidence x-ray diffraction scans of RuO_2 nanorod sample 017-10 before (lower) and after (upper) multiple exposures to 4 torr O_2 and 4 torr CO at temperatures from 20 to 250 °C over a period of several days. A phase change from RuO_2 to Ru is evident.

Figure 7.12 shows scanning-electron-microscope (SEM) images of the morphological changes in RuO_2 sample 017-10 due to the multiple heat cycles with CO or O_2 exposures. The nanorod geometry was significantly altered as the film underwent a phase change to ruthenium with rods aggregating in clumps with large spaces in between. The surface-to-volume ratios of individual crystallites were altered as were the morphologies of both free and grain boundary surfaces.

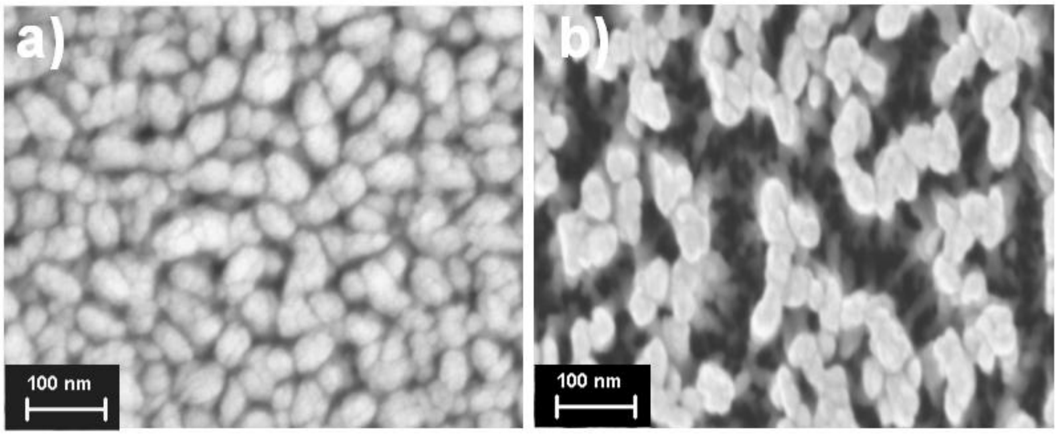

FIGURE 7.12. Plan-view SEM micrographs of RuO_2 sample 017-10: a) as-deposited and b) after multiple exposures to 4 torr O_2 and 4 torr CO at temperatures from 20 to 250 °C over a period of several days.

A question to ask at this point is whether RuO_2 is a necessary starting material for gas switching of resistivity. In answer, Figure 7.13 shows that gas switching is also possible when the starting material is pure Ru. The role that surface oxygen plays in the resistivity hysteresis loops is unclear, but the presence of Ru appears to be necessary.

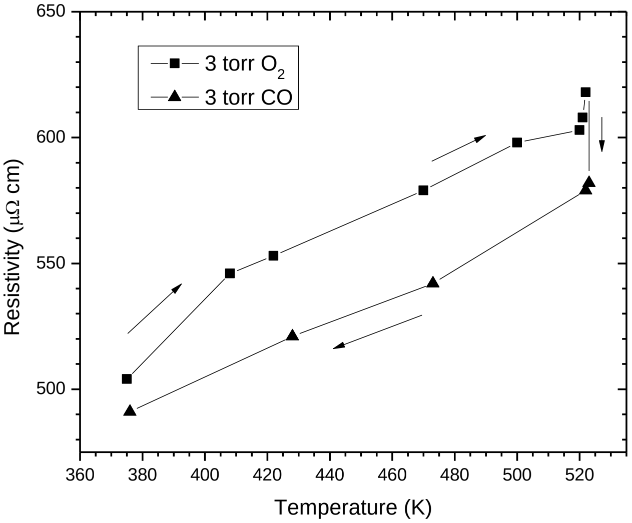

FIGURE 7.13. Resistivity versus temperature for the 3rd heat cycle of Ru nanorod sample 042-09 in 3 torr O_2 and CO. This shows that the resistivity of a Ru film can be switched.

A further question concerning the observed resistivity switching is whether the increased surface area of a nanorod-structured film is necessary or whether the effect can occur on planar films. In answer to this question, the planar RuO_2 film shown in Figure 7.6 was thermally cycled while switching atmospheres between O_2 and CO. It was found that the planar film also yielded a resistivity loop as seen in Figure 7.14.

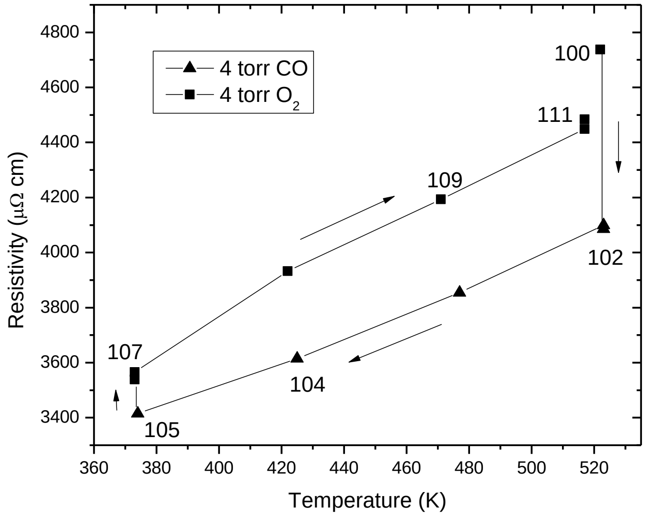

FIGURE 7.14. Resistivity as a function of temperature showing that gas changes can switch the resistivity of a RuO_2 planar film (090910-RuO2-1). The film morphology was severely altered by exposure to CO. Parts of the 4th and 5th heat cycles are shown, starting at point 100.

Immediately after the data were taken, it appeared that the presence of nanorods was unnecessary for switching. Later, however, when the film was inspected, it was found to have been severely eroded as shown in Figure 7.15. This erosion can be seen in Figure 7.16 as a breakup of the film, probably into separate Ru and RuO_2 regions. The transformation of the film may have increased the overall surface area, so the question of whether a large free-surface area is necessary for gas switching is difficult to answer.

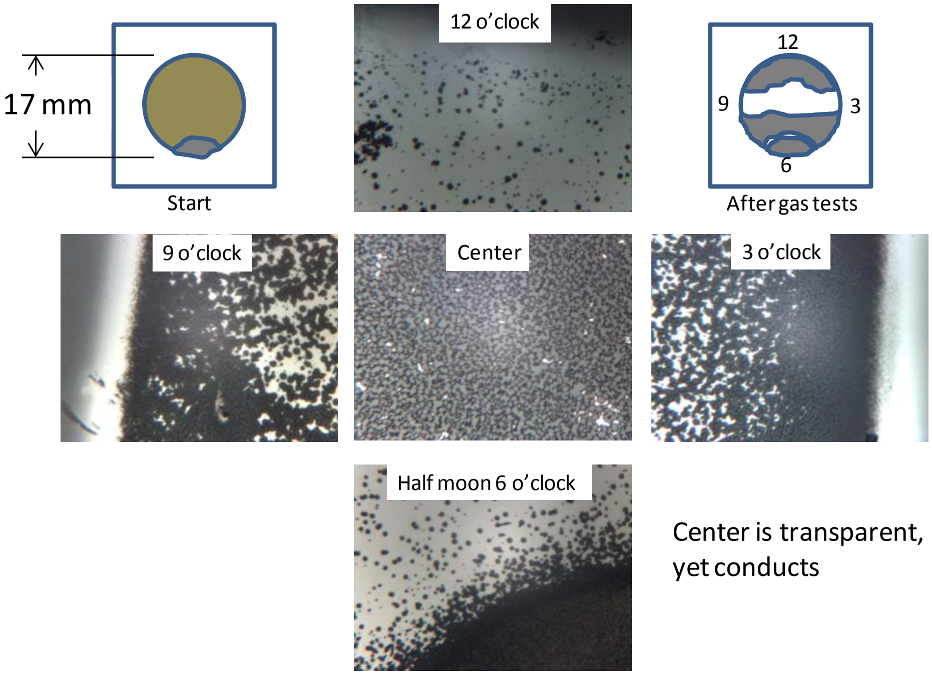

Center is transparent, yet conducts

FIGURE 7.15. Optical microscope images of RuO_2 planar film 090910-RuO2-1 after six thermal cycles in 4 torr O_2 and CO atmospheres. Severe erosion of the film by reaction to CO is evident. Magnification was not noted when the images were taken.

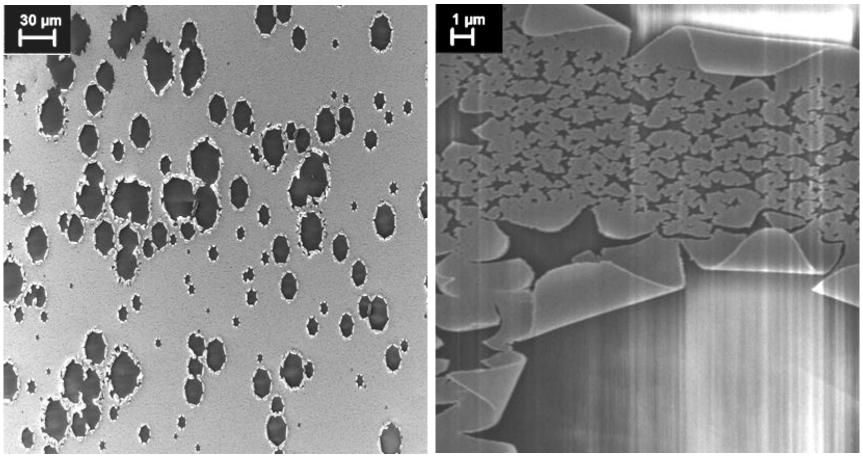

FIGURE 7.16. SEM images of the RuO_2 planar film shown in Figure 7.15.

7.10. Film Breakup Due to Thermal Cycling and Gas Switching

Gas tests eroded the film shown in Figure 7.15 to the point where it was nearly transparent in certain spots. This again raises the issue of the validity of the slab model and of the overall van der Pauw measurements, since they are predicated on the use of a structure with a uniform thickness and without holes. The measured resistivities are therefore likely to be in error, possibly by an order of magnitude or more. However, in spite of the physical breakdown of the film shown, it was still an electrical conductor with a finite resistivity that could be changed in magnitude by roughly 5 to 10 percent by changing from an oxidizing to a reducing gas.

The oxygen loss from RuO_2 films during reducing gas tests differed from that during vacuum tests in one important way. During vacuum tests there was no CO in the chamber and the RuO_2 films changed from dark blue into shiny, nearly silver-gray Ru metal films that showed no physical breakup or erosion. In contrast, the oxygen losses during O_2/CO reductions were linked to physical breakup of the films. It is inferred that exposure to reducing CO at pressures on the order of one torr is the cause of the breakup.

7.11. Effect of Gas Switching on Hall Coefficient

Planar sample 090910-RuO2-2 was grown under the same deposition conditions as planar sample 090910-RuO2-1. It was then annealed in high vacuum (10^{-6} torr) for one hour at 500 °C. A subsequent XRD scan (Figure 7.17) revealed loss of oxygen during the vacuum anneal as discussed in Chapter 6.

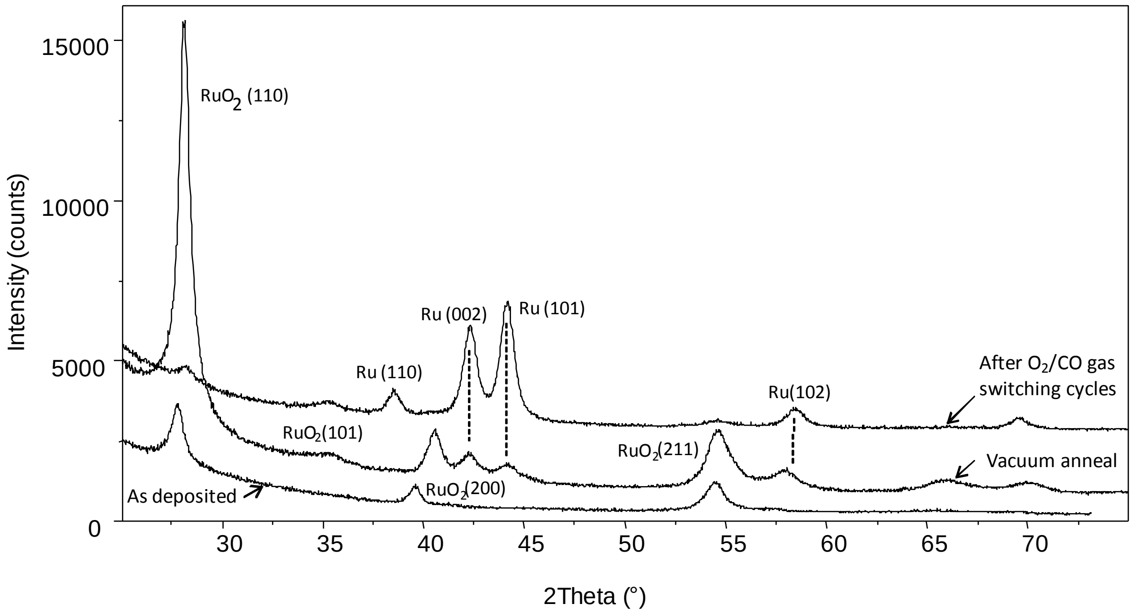

FIGURE 7.17. Grazing-incidence x-ray diffraction scans from planar sample 090910-RuO2-2 in three conditions: as deposited, after a vacuum anneal at 500 °C for 1 hour, and after O_2/CO gas switching thermal cycles.

Gas tests on sample 090910-RuO2-2 started in a 4 torr oxygen atmosphere as shown in Figure 7.18. When the film was heated to 530 K during the first transport test, the resistivity showed the linear increase with temperature that is characteristic of a metal. This was expected from the long anneal at 500 °C. When the atmosphere was switched to 4 torr CO at 250 °C (523 K), there was a pronounced gas response whereby the resistivity increased by about 40 percent over the course of approximately 20 minutes (point 8 to point 9). The total time of exposure to carbon monoxide (points 8 to 13) was approximately one hour. When the gas was switched back to oxygen (point 13) and the temperature lowered back to room temperature (point 25), the resistivity again showed a linear behavior, albeit one at a higher overall magnitude (≈ 10 % increase at 300 K).

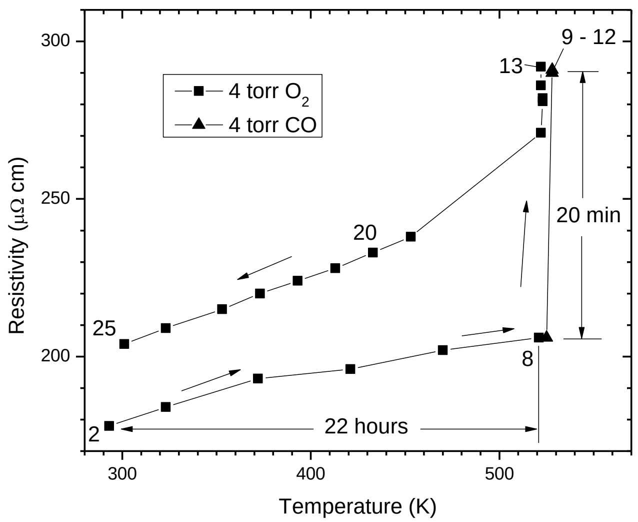

FIGURE 7.18. Resistivity as a function of temperature with atmosphere as a parameter for the first transport test of RuO_2 planar sample 090910-RuO2-2, which was annealed at 500 °C for 1 hour in high vacuum prior to heating in O_2. The film shows the linear behavior characteristic of a metal and a large increase in resistivity upon a first exposure to CO.

High quality Hall coefficient measurements were obtained on sample 090910-RuO2-2 during the first transport-test heat cycle. It is conjectured that minimal film degradation occurred during the relatively short exposure to CO (1 hour) thus enabling the low-noise measurements. Note that most other Hall measurements of films during thermally-cycled gas tests showed high scatter and were unreliable, probably due to film degradation from long exposures to CO. A plot of the Hall coefficient as a function of temperature is shown in Figure 7.19. The magnitude and uncertainty of the key measurement point, which is designated H2 and shows a sign change from H1, is given as -1.2 ± 0.5 cm^3/C. The uncertainties of two other points, H1 and H3, are shown for comparison.

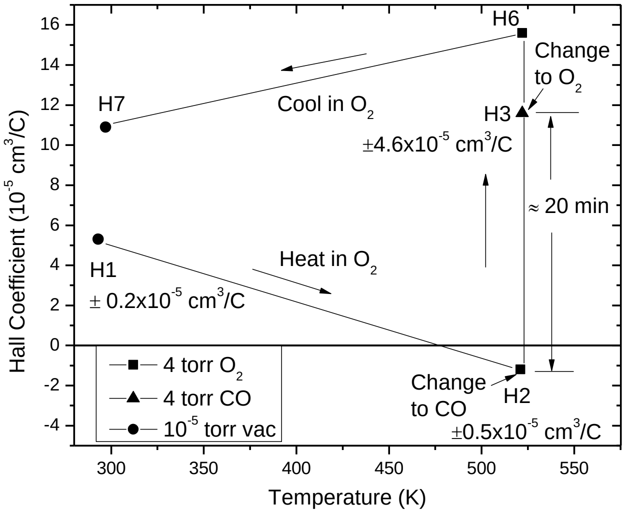

FIGURE 7.19. Hall coefficient as a function of temperature with atmosphere as a parameter for sample 090910-RuO2-2. In going from H1 to H2, the dominant carriers changed from holes to electrons. Uncertainties in points H1 - H3 are shown below their labels.

Following the vacuum anneal at 500 °C, the film was expected to be p-type at room temperature due to the presence of a ruthenium phase and this is borne out in Figure 7.19 (point H1). When the film was heated in 4 torr O_2 to 250 °C (523 K), the Hall coefficient changed to n-type with electrons as dominant carriers (point H2). Switching to 4 torr CO changed the dominant carriers back to p-type and significantly increased the magnitude of the Hall coefficient (point H3). Switching back to 4 torr O_2 at the same temperature then caused an even higher Hall coefficient (point H6), which could be due to data scatter. Cooling back to room temperature in O_2, followed by evacuation to 10^{-5} torr vacuum, resulted in the final value (point H7) of approximately +11 x 10^{-5} cm^3/C, which is not far from the Hall coefficient of bulk ruthenium metal (nominally +22 x 10^{-5} cm^3/C, see Chapter 4).

With regard to the experimental procedure, it needs to be pointed out that changing gases created problems for the temperature controller due to changes in the gas/vacuum heat transfer coefficients. The film temperature therefore varied around the 250 °C set point by roughly ± 35 °C before equilibrium was re-established. This temperature deviation is believed to have had little impact on the outcome of the Hall measurements, since the total temperature excursion lasted no longer than about 15 minutes.

In Figure 7.20, the Hall coefficients at points H1, H2 and H7 in Figure 7.19 are plotted on the RuO_2 phase diagram discussed in Chapter 6 (Figure 6.8) under the assumption that a room-temperature phase diagram will be roughly similar to one at 523 K. The validity of the assumption may be questionable. It is true that the Hall coefficient of ruthenium is not strongly dependent on temperature as shown in Chapter 4, so the Ru-rich side of the phase diagram may apply at higher temperatures. However, according to Ryden et al.,[18] the Hall coefficient of RuO_2 at 77 K is about 75 % of that at 300 K, so the Hall coefficient of RuO_2 does show a small temperature dependence. Thus, the RuO_2 side of the phase diagram may not apply at 523 K (also compare points H6 and H7 in Figure 7.18).

The transition from p-type to n-type behavior due to heating in O_2 is shown by points H1 and H2 in Figure 7.20. When the atmosphere was switched to CO at 250 °C, the dominant charge carriers changed from electrons back to holes. Changing from CO back to O_2 did not reverse the sign of the Hall coefficient. Finally, cooling to room temperature in O_2 lowered the Hall coefficient by about 30 percent, and the final measurement in vacuum is shown by point H7, which is placed at two possible extremes in Figure 7.20. That is, uncertainty in the Hall coefficient of pure ruthenium, as explained in Chapter 4, implies that point H7 could lie on or between the lines labeled Justi or Volkenshteyn. Although the uncertainty is rather large, the key point is that the Hall coefficient can be changed from p-type to n-type by heating in O_2 and then returned from n-type to p-type by heating in CO.

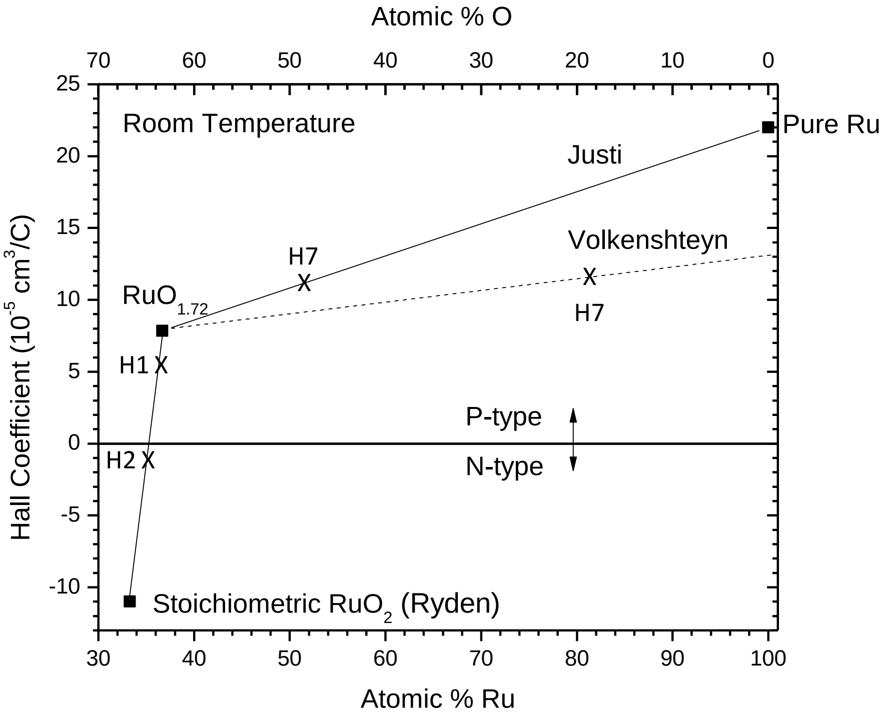

FIGURE 7.20. Room-temperature Hall coefficient phase diagram showing measurement points from sample 090910-RuO2-2. Uncertainty in the Hall coefficient of pure ruthenium leads to uncertainty in the position of point H7, which could lie on or between the two positions shown.

Hall measurements as a function of temperature were also obtained on sample 064-10 and are plotted in Figure 7.21. This film was a planar RuO_2 sample grown by normal-incidence sputter deposition without substrate rotation. The resistivity as a function of temperature for this sample was shown in Figure 7.8 where no gas response was evident. As stated above, after approximately 2 days of heating in CO at 4 torr, the film appearance was nearly transparent and the morphology resembled that shown in Figure 7.15. Interestingly, exposure to CO for 46 hours lowered the Hall coefficient of the film, which seems to contradict the results for planar sample 090910-RuO2-2.

Referring back to Table 7.1, it is seen that both of these films were grown on room temperature substrates and hence had high defect contents. However, two major differences were that: (i) sample 064-10 was grown at normal incidence with no substrate rotation, while 090910-RuO2-2 was grown at off-normal incidence with substrate rotation, and (ii) sample 064-10 had no post-deposition anneal, while sample 90910-RuO2-2 underwent a 500 °C vacuum anneal for 1 hour. To summarize, sample 064-10 was a single-phase RuO_2 film that did not show a resistivity gas response and did not show a change in the sign of the Hall coefficient, which started out as n-type and apparently stayed n-type when exposed to CO for 46 hours. On the other hand, sample 090910-RuO2-2 was a two-phase mixture of RuO_2 and Ru that did show a resistivity gas response and did show a change in the sign of the Hall coefficient, going from p-type to n-type when heated in O_2 and then reverting back to p-type when heated in CO. It is speculated that the presence of a Ru phase in sample 090910-RuO2-2 and the lack of a Ru phase in sample 064-10 prior to CO exposure may explain the contradiction in behavior, but the nature of the physical mechanism for the observed results is unclear. With the sole exception of sample 064-10, the Hall coefficients of all samples became progressively more p-type as oxygen was lost from the films as reflected in the Hall coefficient phase diagram of Figure 6.8. Note also that both of these films were badly eroded by CO exposure.

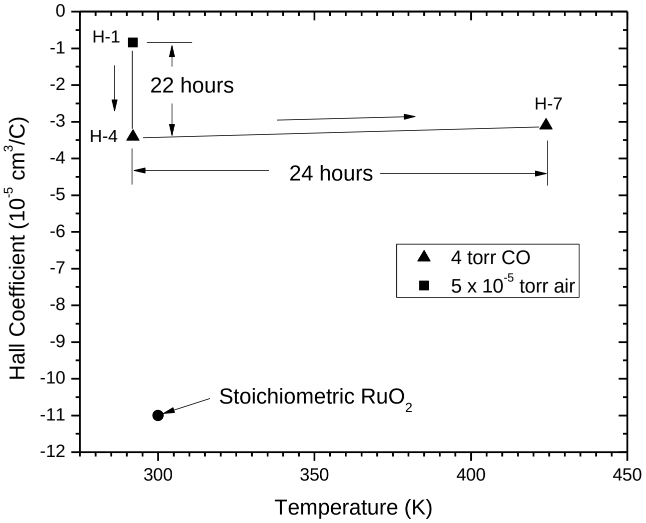

FIGURE 7.21. Hall coefficient as a function of temperature for RuO_2 planar sample 064-10 when exposed to 4 torr CO for 46 hours. No change in the sign of the Hall coefficient was observed. Measurement uncertainties were: H-1 ($\pm 0.15 \times 10^{-5}$ cm^3/C), H-4 ($\pm 0.3 \times 10^{-5}$ cm^3/C), and H-7 ($\pm 0.03 \times 10^{-5}$ cm^3/C).

7.12. Oxygen Loss in a Reducing Environment

Perhaps the most significant result of the transport tests in O_2 and CO was the instability and subsequent phase change from RuO_2 to Ru due to exposure to a reducing CO atmosphere. The stripping of oxygen from RuO_2 surfaces by catalysis of CO into CO_2 was expected since previous work had demonstrated experimentally that CO will remove oxygen from a RuO_2 surface.[2] Furthermore, Gao et al.[9] have demonstrated that a RuO_2 surface exposed to a mixture of O_2 and CO can be reduced to a Ru surface covered by a chemisorbed oxygen phase. The exposure to a reducing gas may create a roughened Ru surface with a high density of reactive sites for CO_2 catalysis. According to Sljivancanin and Hammer,[10] these reactive sites are likely at ruthenium step edges.

To the best of our knowledge, what has not been demonstrated is the loss of interior oxygen and the full reduction of a RuO_2 film to a Ru film due to exposure to CO. Hiratani et al.[19] observed the reduction and loss of volume of a RuO_2 electrode to Ru metal at 200 °C in 0.3 % H_2 and at 300 °C in 0.03 % H_2, but no similar studies pertinent to CO are believed to exist. The loss of interior oxygen most likely starts with the loss of oxygen on free and grain boundary surfaces. Oxygen removal then results in ruthenium-rich areas that can act as nucleation points for further growth of pure Ru grains under favorable conditions. That is, continuous oxygen diffusion to the surface depletes oxygen throughout the film leading to pure Ru. For example, it has been shown that after a 10 Langmuir CO exposure, a carbon-monoxide-covered RuO_2 (110) surface is formed, which when heated briefly to 600 K (327 °C) will desorb both CO and CO_2.[2] Some of the oxygen is believed to come from the subsurface lattice, leaving ruthenium-rich areas behind. A reproduction of a figure from Over et al.[2] is shown in Figure 7.22 where the bright protrusions are thought to be clusters of Ru atoms. These clusters are consistent with the nucleation points needed to produce a phase change from RuO_2 to pure Ru.

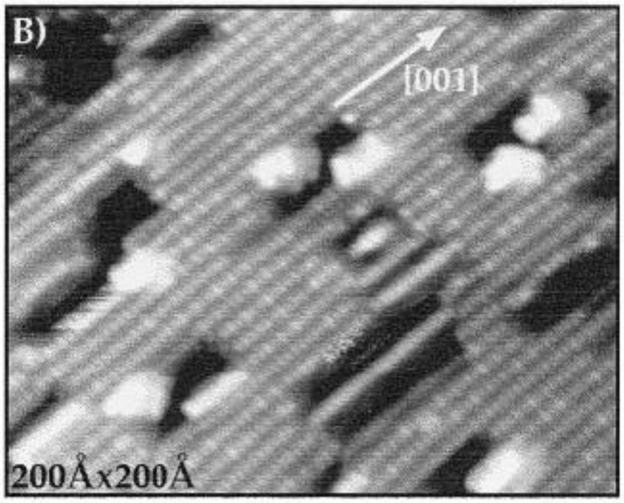

FIGURE 7.22. Scanning-tunneling microscope image of a CO-covered RuO_2 (110) surface after annealing to 600 K. The removal of CO molecules creates both dark holes 1.5 Å to 3.0 Å deep and bright spots thought to be clusters of Ru atoms. The Ru clusters are potential nucleation sites for a phase change from RuO_2 to Ru. (Reproduction of Fig. 4B, reference 2)

7.13. Interpretation of Transport Measurement Results

In thin films, imperfections comprise point and extended defects such as vacancies, interstitials, dislocations, strain, free surfaces, and grain-boundary surfaces. These structural imperfections raise resistivity above what can be accounted for by lattice vibration alone (phonons). On short time scales, redox reactions in RuO_2 and Ru thin films change the defect densities and associated morphology (topography) of free and grain boundary surfaces. On longer time scales, surface, boundary, or lattice diffusion can introduce imperfections and nanostructural changes in the bulk lattice, roughen surfaces, and change the ratio of free-to-grain-boundary surface areas. In a reducing atmosphere such as CO, diffusion can ultimately lead to film breakup and erosion as has been demonstrated.

A phenomenon that makes interpretation of resistivity changes during CO/O_2 reactions difficult is the inversion of resistivities seen on first exposure to CO relative to those seen after multiple exposures and thermal cycles. For example, when films were first heated in O_2 and then switched to CO at a fixed temperature, the resistivity increased. After multiple heat cycles, however, the opposite was true - the resistivity in O_2 was higher than that in CO. This behavior was observed in both RuO_2 and Ru films: see, for example, Figures 7.7 and 7.13 for Ru nanorod sample 042-09. It is believed that the change of resistivities from CO-high/O_2-low to CO-low/O_2-high is related to long-term heating and exposure to CO, which can alter: (i) grain size and therefore the ratio of free to grain-boundary surface areas and (ii) surface roughness.

7.13.1. Surface versus Bulk Diffusion

The diffusion rate of atoms along metal surfaces is many orders of magnitude greater than bulk diffusion as seen in Figure 7.23. Ruthenium melts at roughly 2600 K. At 1300 K, where $T_m/T = 2$, Figure 7.23 indicates that the free-surface diffusivity, D_s, is nearly 10^9 times the bulk diffusivity D; the grain-boundary diffusivity, D_{gb}, is nearly 10^8 times D. Since temperatures in the experiment were roughly 500 K ($T_m/T \approx 5$), it is concluded that on time scales measured in tens of minutes, diffusion along surfaces was vastly faster than through the bulk and was responsible for changes in transport properties such as the CO-induced resistivity peak. On longer time scales, measured in tens of hours, oxygen loss and the subsequent phase change from RuO_2 to Ru are evidence that all diffusion mechanisms played a role.

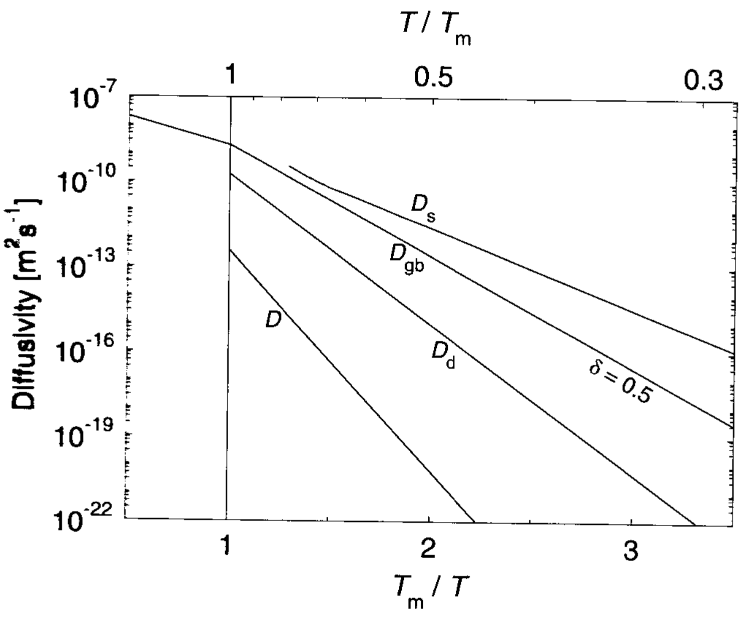

FIGURE 7.23. Schematic illustration of the trend in diffusion rates in generic metals in a reduced temperature scale; T_m denotes the melting temperature. Diffusion coefficients (diffusivity) are D for bulk, D_d for dislocation pipeline, D_{gb} for grain boundary, and D_s for free surface. (Reproduction of Fig. 31.2, reference 20)

According to measurements by Deckert et al.,[21] the surface diffusivity of CO on Ru(001) at 290 K is 1 x 10^{-8} cm^2/s for a surface coverage of 0.33 ML and increases up to 1 x 10^{-6} cm^2/s for a surface coverage of 0.58 ML. Using Figure 7.23 to estimate grain-boundary diffusivity by extrapolation, with T_m/T equal to 5, yields an approximate value of $D_{gb} \approx 10^{-12}$ cm^2/s for the 0.33 ML coverage, which might very roughly approximate grain boundary coverage. It seems likely that the grain-boundary diffusivity of CO_2 would be less than or equal to this value because it is a larger linear molecule than CO and should therefore diffuse more slowly along boundaries.

The hypothesized diffusion of CO_2 out of the base-layer grain boundaries of RuO_2 nanorod sample 019-10 in Figure 7.2 allows an estimate of the diffusivity based on the exponential decay of resistivity versus time. That is, the diffusion coefficient may be written in terms of an estimated grain-boundary length and a characteristic decay time $D_{gb} \approx l^2/t$. Taking the base-layer grain-boundary length as roughly twice the base-layer height, or about 20 nm, and the characteristic decay time as roughly 70 minutes to fall to 37 % of the peak value of resistivity in Figure 7.2, yields an estimated grain-boundary diffusivity of $D_{gb} \approx 10^{-15}$ cm^2/s. This result may be compared to measurements of diffusion of inert gases in polycrystalline copper by Rickers and Sorensen.[22] They measured the diffusivity of Kr in copper at 450 °C to be 2 x 10^{-15} cm^2/s. Based on the Kr diffusivity and the extrapolation for CO at 500 K given above, 10^{-15} cm^2/s is a plausible order-of-magnitude estimate for grain-boundary diffusivity of CO_2 in RuO_2 and Ru films.

7.13.2. Resistivity Based on Surface Scattering Effects

It is hypothesized that the changes in resistivity, whether due to a first exposure to CO or to repeated CO/O_2 redox reactions, were caused by changes in surface morphology that altered the scattering mechanism of conduction electrons similar to the findings of Watanabe and Hiratuka,[23] although changes in the overall charge concentration may have played some role if surface-to-volume ratios were high. To quantify the morphology effect, Sun et al.[24] show how the intrinsic resistivity, which is given by Matthiessen's rule as a sum of phonon and bulk defect contributions, can be altered by a multiplicative factor that incorporates the following surface parameters: (i) grain-boundary reflection coefficients,[25] (ii) specular scattering coefficients,[26-27] and (iii) roughness.[28]

Generally, at temperatures well above the cryogenic range, electron scattering at the grain boundaries of a thin polycrystalline film is the primary cause of increased resistivity above that of a thin single-crystal film. However, free surface scattering may have played a role in the films investigated in this study due to morphology changes induced by long-term CO exposure. An expression for resistivity that incorporates the surface parameters is given by

$$\rho = \rho_o\left(f_{gb} + f_{fs} + f_r\right) \tag{7.1}$$

where the film resistivity ρ equals the intrinsic bulk resistivity of a single crystal, ρ_o, modified by three coefficients related to surfaces. A key assumption in this expression is that free-surface and grain-boundary scattering are non-interacting.[24]

The grain boundary factor f_{gb}, posed by Mayadas and Shatzkes,[25] is

$$f_{gb} = \left[1 - \frac{3}{2}\alpha + 3\alpha^2 - 3\alpha^3 ln\left(1 + \frac{1}{\alpha}\right)\right]^{-1} \tag{7.2}$$

with the scattering parameter α given by

$$\alpha = \left(\frac{l_o}{d}\right)\left(\frac{R}{1 - R}\right) \tag{7.3}$$

where l_o is the electron mean free path, d is the average distance between grain boundaries, and R is the surface reflection coefficient, i.e., the fraction of electrons that bounce back from the boundary ($0 < R < 1$). For a single crystal with no grain boundaries, the value of d becomes infinite making α zero and f_{gb} equal to one. It is noteworthy that for the long heat cycles in the RuO_2 experiments, grain growth would cause increases in d and possibly also change l_o due to point defect annealing.

The free surface factor f_{fs}, determined by Fuchs and Sondheimer,[26-27] is

$$f_{fs} = \frac{3}{8\kappa}(1 - p) \tag{7.4}$$

under the assumption that $\kappa >> 1$, where $\kappa = h/l_o$ is the ratio of the grain height, h, to the electron mean free path, l_o, and p is the specular scattering coefficient. The assumption made here of a large κ is open to question, but for highly defective films the electron mean free path might be on the order of one tenth of a grain diameter. Note that in the Fuchs-Sondheimer model, h is the thickness of a single-crystal film.

Finally, the surface roughness factor f_r, determined by Rossnagel and Kuan,[28] is

$$f_r = f_{fs}\left(1 + \frac{r}{n_{RK}}\right) \tag{7.5}$$

where r is the root-mean-square (rms) roughness of the surface and n_{RK} is a factor that incorporates film thickness and Fermi wavelength and is determined by Monte Carlo calculations of electron trajectories.[24] As stated above, it is hypothesized that changes in the parameters R, p, and r are primarily responsible for the changes in resistivity brought about by surface redox reactions.

7.13.3. Surface Morphology and Electron Scattering

Consider a Ru nanorod-structured thin film such as sample 042-09. Surface morphology of this film was changed by gas exposure in two ways on different time scales. The CO/O_2 redox reactions changed the nature of the chemisorbed layers on free and grain-boundary surfaces over short time scales (tens of minutes). On longer time scales (tens of hours) including thermal cycles, it is believed that the CO/O_2 redox reactions roughened the Ru film surfaces as well as increased grain size. Figure 7.24 shows a ball-and-stick model of an O atom and also CO and CO_2 molecules adsorbed to ruthenium at a surface. The topological configurations represent different potential energy barriers and hence different boundary conditions for electron reflection. In terms of surface parameters for a given roughness, the grain-boundary reflectivities of the three configurations would be unequal ($R_O \neq R_{CO} \neq R_{CO_2}$) and the free-surface specular scattering coefficients would also be unequal ($p_O \neq p_{CO} \neq p_{CO_2}$).

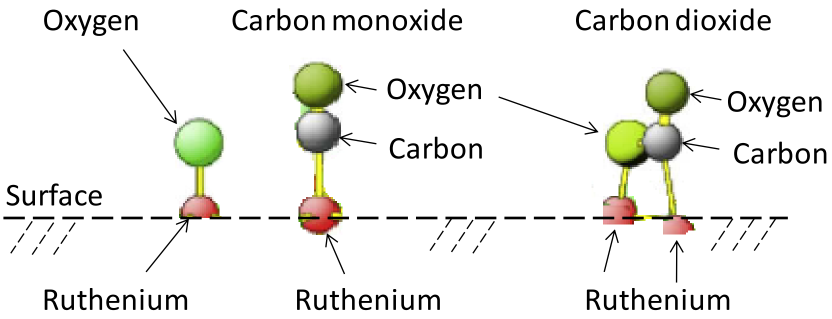

FIGURE 7.24. Ball-and-stick model showing O, CO, and CO_2 bonded to Ru surface atoms forming different boundary conditions for electron reflection.[8] Note that the O_2 molecule is separated into individual oxygen atoms on the surface.

Electron scattering will change according to which gases are present on the surfaces. Carbon dioxide, as a product of catalysis, has a small residence time and quickly desorbs from a ruthenium surface while chemisorbed oxygen and carbon monoxide are stable. It is interesting to note that the ranking of the gases in terms of molecular size is $CO_2 > O_2 > CO$, from which it may be inferred that CO would diffuse fastest along grain boundaries and free surfaces and CO_2 would diffuse slowest.

Atomic-scale roughness on a Ru(0001) surface is illustrated in Figure 7.25 reproduced from Sljivancanin and Hammer.[10] The two types of monatomic steps of ruthenium atoms labeled I and II are sites of CO oxidation to CO_2 and represent different boundary conditions for electron scattering as captured by the specularity coefficient p and roughness parameter r.

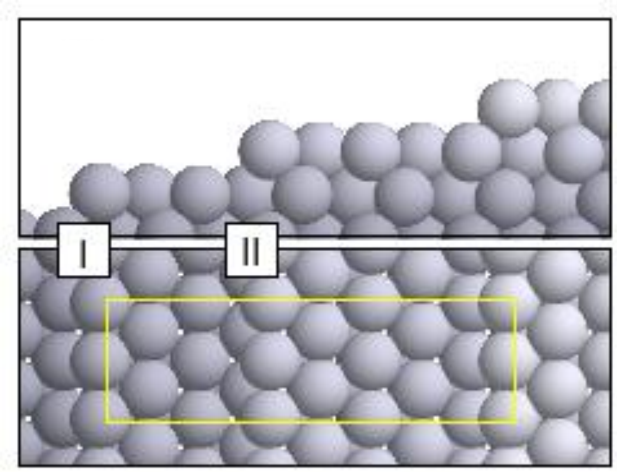

FIGURE 7.25. Ru(0001) surface shown in elevation (top) and plan (bottom) views. Two types of monatomic steps, marked I and II, are sites of catalysis. (Reproduction of Figure 1, reference 10)

It is also possible that exposure of RuO_2 surfaces to pure O_2 may have formed a surface carbonate. For example, Rossler et al.[29] found evidence that exposure of a $RuO_2(110)$ surface to 152 torr O_2 at room temperature gave rise to a strongly bound carbonate. When the O_2 gas was removed, the carbonate was found to be stable at room temperature in a pure CO atmosphere of 16 torr. If stable at higher temperatures, a carbonate would obviously yield a surface morphology different than the model presented here for O_2, CO, and CO_2. It is worth noting that Over et al.[5] claim to have never observed a carbonate in CO oxidation over $RuO_2(110)$ in pressures up to 76 mtorr and temperatures up to 600 K.

7.13.4. Resistivity Increase on First Exposure to Carbon Monoxide

Typically, first exposures to CO took place after relatively short periods of heating, thereby limiting any grain growth due to annealing. To interpret the rise in resistivity observed for a Ru film, consider the 10 percent resistivity increase seen for the nanorod-structured film of Figure 7.7 due to switching of gases from 4 torr O_2 to 4 torr CO at 522 K. Catalysis of CO to CO_2 at Ru step edges, like those shown in Figure 7.25, may have removed oxygen from free and grain-boundary surfaces, which subsequently became covered by chemisorbed CO_2 and CO. Due to the speed of the resistivity rise, which is on the order of tens of minutes, it is hypothesized that changes in the reflection coefficient at grain-boundary surfaces and the scattering parameter at free surfaces are the major sources of the resistivity increase. Although this particular film had a nanorod geometry with a large free surface area, it is further assumed that grain-boundary reflections were dominant because: (i) the temperature was 522 K (not cryogenic), (ii) smaller grain sizes mean larger ratios of grain-boundary to free surface areas, and (iii) the distance between grain boundaries, d, was relatively smaller due to the smaller grain sizes. In terms of the electron reflection coefficient, the argument is that CO_2 and CO on grain boundaries scatter electrons more effectively than O on grain boundaries for fixed surface roughness ($R_{CO_2} > R_{CO} > R_O$). After the exponential rise in resistivity, it is speculated that the slower exponential fall in resistivity may have been due to the desorption and slow diffusion of CO_2 from grain boundaries. Alternatively, the slow fall in resistivity may have been due to desorption of CO_2 from free surfaces.

7.13.5. Resistivity Hysteresis Loops during CO/O_2 Redox Reactions

Still focusing on a Ru film, resistivity hysteresis loops occurred after thermal cycling in CO and O_2. Multiple cycles resulted in lower resistivities in CO than in O_2 (e.g., see Figure 7.13). Heat cycles on the order of days allowed for grain growth, thereby increasing the grain-size parameter d. It is conjectured that surface roughness was also increased by long exposures to CO.[9] An increase in roughness would mean that the specularity coefficient would get smaller and that the rms roughness parameter would increase. Assuming that the reflection coefficients at grain boundaries maintain the same relationship as above (i.e., $R_{CO} > R_O$), one interpretation for gas-switched resistivity changes is that electron scattering from the free surfaces is greater than that from grain boundary surfaces with the specularity coefficients having the form $p_O > p_{CO}$ and the roughness parameters having the form $r_O > r_{CO}$. This is saying that the parameters f_{fs} and f_r become the governing factors in equation 7.1. A second possible interpretation is that the grain-boundary surfaces are still dominant in terms of electron scattering, but surface roughening somehow leads to a switch in the strength of the grain-boundary reflection coefficients causing $R_O > R_{CO}$. Whichever model, if either, applies to the observations could not be answered by the experiments. A third model of the resistivity hysteresis loops is based on redox as will be explained below.

7.13.6. Carrier Concentration Changes from Redox Reactions

The arguments given above have focused on changes in surface parameters that alter electron scattering and hence resistivity. No mention has yet been made of alterations in carrier concentrations due to exposure to reducing or oxidizing gases. Specifically, the oxidization of CO to CO_2 will liberate two electrons and thereby reduce the surface ($CO + O^{2-} \rightarrow CO_2 + 2e^-$).[30] It would be expected, therefore, that as chemisorbed oxygen is removed from ruthenium surfaces by CO, resistivity would drop according to the model for two-carrier conduction,

$$\rho = (n_e e \mu_e + n_h e \mu_h),^{-1} \tag{7.6}$$

because the electron concentration, n_e, in individual crystallites would increase. (Here e is the charge on the electron, n_e and n_h the electron and hole concentrations, and μ_e and μ_h

the electron and hole mobilities). Given enough surface area, modulations in charge carrier concentrations accompanying the redox chemistry can, in principle, explain the resistivity hysteresis loops (lower resistivity in CO; higher in O_2).

The weakness of the argument is that surfaces have about 10^{15} atoms per square centimeter.[31] A 1 cm^2 planar film with a 100 nm thickness would therefore release roughly 10^{15} extra electrons. This must be compared to a bulk concentration of roughly 10^{17} electrons based on a film volume of 10^{-5} cm^3 and a metal bulk carrier concentration of 10^{22} carriers/cm^3. That is, the resistivity change in a planar film should be of the order of 1 percent. Given that a nanorod-structured film has roughly ten times the surface area of a planar film, the resistivity change would be in the 10 percent range. Thus, it seems to be theoretically possible that the hysteresis loops of the nanorod films can be explained by charge carrier generation due to redox alone. However, it seems likely that surfaces played a role by increasing electron scattering and hence resistivity, because hysteresis loops were also observed in planar films with lower surface areas.

In contrast to the hysteresis loops, the initial irreversible resistivity response seen in some films (see Figures 7.4 and 7.7), cannot be explained by redox charge generation because the resistivity in CO was higher than that in O_2. That is, liberating additional conduction electrons by surface oxygen removal cannot raise resistivity. As mentioned above, the irreversible resistivity response may be explained by the release of CO_2 from grain boundaries and possibly surfaces, which is a dynamic process that would change the electron scattering coefficients as a function of time.

7.13.7. Hall Coefficient Sign Changes

Sample 090910-RuO2-2 was subjected to a vacuum anneal for one hour at 500 °C prior to transport tests. As evidenced by the x-ray diffraction data in Figure 7.17, annealing caused a structural change resulting in a two-phase system of RuO_2 and Ru. The Ru phase likely consisted of islands, primarily on surfaces, as shown in Figure 7.22. It is conjectured that these islands, when exposed to O_2 at 523 K for roughly 12 hours, reverted either fully or partly back to RuO_2 and changed the mix of the two-phase system back to one where RuO_2 was the controlling phase as shown by point H2 in Figure 7.20. (Note that temperatures above 500 K allow RuO_2 formation.[5]) Subsequent exposure to CO reduced the islands back to Ru, and furthermore, continued the reduction of the remaining RuO_2 film.

The tie line between points labeled $RuO_{1.72}$ and RuO_2 in Figure 7.20 allows for a very rough estimate of the oxygen gained by the film during its 12 hour anneal in O_2. The tie line has been magnified in Figure 7.26, where it is seen that the atomic oxygen level increased from approximately 64 to 65 %, about a one percent increase.

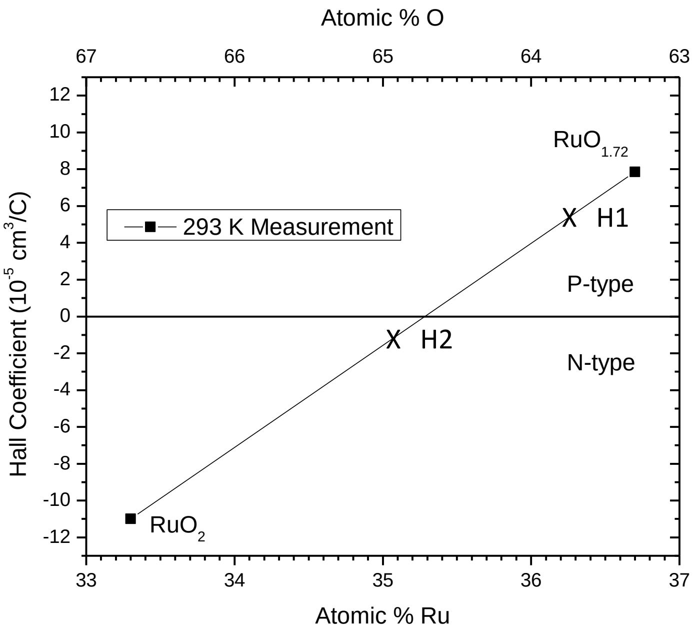

FIGURE 7.26. Hall coefficient phase diagram used to estimate the increase in atomic oxygen in sample 090910-RuO2-2 due to O_2 exposure at 523 K.

The increase in atomic oxygen was sufficient to change the dominant charge carrier type from holes to electrons (points H1 to H2). A possible explanation for the dominant carrier change is simply the alteration in the makeup of the two-phase mixture of RuO_2 and Ru, so that more of the electron-dominant RuO_2 was present. The dominant carrier in a two-phase system like the one considered here may be governed by a rule of mixtures of some type. Another possibility is that oxygen changes in sub-stoichiometric RuO_2 influence the curvature of the Fermi surfaces in such a way that the effective mass of electrons becomes less than that of holes.

7.14. Chapter Summary

For either RuO_2 or Ru thin films grown under the conditions outlined in Table 7.1, charge transport experiments have demonstrated that a first exposure to CO can yield a significant increase in thin-film resistivity that appears to follow an exponential behavior in time. Follow-on heat cycles with gas switching between CO and O_2 were shown to give rise to resistivity hysteresis loops that are driven by catalytic reactions on Ru surfaces. Changes in resistivity may be explained by changes in surface reflection and scattering coefficients, although changes in charge concentration may also play a role. It was shown that chemisorbed O_2 and CO can change the sign of the Hall coefficient and hence switch the dominant carriers from electrons to holes and vice-versa. In the range of temperatures and pressures considered, it was found that polycrystalline RuO_2 films are unstable under long term exposure to CO and can undergo a phase change to Ru.

---

[1] C.H.F. Peden and D.W. Goodman, J. Phys. Chem. 90, 1360 (1986).

[2] H. Over, Y.D. Kim, A.P. Seitsonen, S. Wendt, E. Lundgren, M. Schmid, P. Varga, A. Morgante and G. Ertl, Science 287, 1474 (2000).

[3] H. Madhavaram, H. Idriss, S. Wendt, Y.D. Kim, M. Knapp, H. Over, J. Assmann, E. Loffler and M. Muhler, J. Catalysis 202, 296 (2001).

[4] D.W. Goodman, C.H.F. Peden and M.S. Chen, Surf. Sci. Let. 601, L124 (2007).

[5] H. Over, M. Muhler and A.P. Seitsonen, Surf. Sci. 601, 5659 (2007).

[6] D.W. Goodman, C.H.F. Peden and M.S. Chen, Surf. Sci. 601, 5663 (2007).

[7] J. Assmann, V. Narkhede, N.A. Breuer, M. Muhler, A.P. Seitsonen, M. Knapp, D. Crihan, A. Farkas, G. Mellau and H. Over, J. Phys.: Condens. Matt. 20, 184017 (2008).

[8] A.P. Seitsonen and H. Over, Surf. Sci. 603, 1717 (2009).

[9] F. Gao, Y. Wang, Y. Cai and D.W. Goodman, Surf. Sci. 603, 1126 (2009).

[10] Z. Sljivancanin and B. Hammer, Phys. Rev. B 81, 121413(R) (2010).

[11] M.M. Steeves, D. Deniz and R.J. Lad, Appl. Phys. Let. 96, 142103 (2010).

[12] L.J. van der Pauw, Philips Res. Repts 13, 1 (1958).

[13] American Society for Testing and Materials, ASTM F 76-86 (1996).

[14] W.E. Bell and M. Tagami, J. Phys. Chem. 67, No. 11, 2432 (1963).

[15] B. Brunetti, P. Scardala and V. Piacente, Matls. Chem. Phys. 83, 145 (2004).

[16] T.J. Coutts, *Electrical Conduction in Thin Metal Films* (Elsevier, Amsterdam, 1974).

[17] V. Vand, Proc. Phys. Soc. 55, 222 (1942).

[18] W.D. Ryden, A.W. Lawson and C. C. Sartain, Phys. Rev. B, 1,1494 (1970).

[19] M. Hiratani, Y. Matsui, K. Imagawa and S. Kimura, Jpn. J. Appl. Phys. 38, L1275 (1999).

[20] H. Mehrer, *Diffusion in Solids* (Springer, Berlin, 2007).

[21] A. A. Deckert, J.L. Brand, M.V. Arena and S.M. George, Surf. Sci. 208, 441 (1989).

[22] G. Rickers and G. Sorensen, Physica Status Solidi, 32, 597 (1969).

[23] M. Watanabe and A. Hiratuka, Jap. J. Appl. Phys. 18, 31 (1979).

[24] T. Sun, B. Yao, A.P. Warren, K. Barmak, M.F. Toney, R.E. Peale and K.R. Coffey, Phys. Rev. B 81,155454 (2010).

[25] A.F. Mayadas and M. Shatzkes, Phys. Rev. B 1, 1383 (1970).

[26] K. Fuchs, Proc. Camb. Phil. Soc. 34, 100 (1938).

[27] E.H. Sondheimer, Adv. Phys. 1, 1 (1952).

[28] S.M. Rossnagel and T.S. Kuan, J. Vac. Sci. Technol. B 22(1), 240 (2004).

[29] M. Rossler, S. Gunther and J. Wintterlin, J. Phys. Chem. C, 111, 2242 (2007).

[30] V.E. Henrich and P.A. Cox, *The Surface Science of Metal Oxides* (Cambridge, 1994).

[31] G.A. Somorjai, *Introduction to Surface Chemistry and Catalysis* (Wiley, New York, 1994).

Chapter 8

CONCLUSIONS

The resistivities and Hall coefficients of ruthenium and ruthenium dioxide thin films having a variety of structures and morphologies have been measured in specific ranges of temperature, pressure, and gas atmosphere. Findings are summarized below along with recommendations for future work.

8.1. Summary

In Chapter 4, the Hall coefficient data for Ru obtained from flat and nanorod-structured films were found to match literature values for bulk samples when an effective thickness correction was made for films with nanorod geometry. The Hall coefficient was shown to be nearly independent of temperature over the range tested in accordance with most metals. Non-impurity defects were inferred to have no significant effect on the Hall coefficients at temperatures from 300 to 600 K. It should be noted that the work presented here constitutes the first published Hall measurements of Ru thin films. A decrease in resistivity upon first heating was found to be caused by defect annealing. In addition to defect content, uncertainty in thickness with non-slab geometries was shown to have a major influence on the calculation of resistivity from measured film resistance. If the spacing between adjacent nanorods is large enough, the height of an ultra-thin polycrystalline layer at the film-substrate interface was inferred to be the dominant factor in the determination of resistivity using a slab model of resistance for nanorod-structured metallic thin films.

In Chapter 5, the resistivity and temperature-coefficient-of-resistance (TCR) of RuO_2 thin films were shown to be strongly dependent on film defect density, whereas the Hall coefficient was found to be less sensitive to defect structure. A decrease in resistivity upon first heating was concluded to be due to defect annealing as was the case with Ru thin films. The TCR of polycrystalline films of RuO_2 was measured to be extremely small, having a value similar to other low-TCR materials such as nichrome. Mixed electron-hole conduction was found to take place in RuO_2, and it was conjectured that electron and hole concentrations are nearly equal, and that RuO_2 is likely to be a compensated metal. It was concluded that changes in film structure and strain can lead to changes from n-type to p-type conduction.

In Chapter 6, certain RuO_2 films were observed to lose oxygen and to be unstable in high vacuum at temperatures slightly above room temperature. The observations of oxygen loss in high vacuum are believed to be novel findings. An energy-related mechanism, such as lattice strain, was hypothesized to drive the subsequent phase change. It was stated that a Hall coefficient phase diagram with respect to composition must exist for RuO_2, and that it should be possible to map the Hall coefficient as a function of composition when moving from pure Ru to stoichiometric RuO_2.

In Chapter 7, measurements of transport properties of RuO_2 and Ru films during surface redox reactions constitute completely new findings. The exposure of certain polycrystalline RuO_2 thin films to pure CO was shown to irreversibly increase the (apparent) resistivity. After heat cycles with gas switching from O_2 to CO, resistivity hysteresis loops were observed and it was conjectured that changes in resistivities were controlled by redox reactions on Ru rather than RuO_2 surfaces. Chemisorbed oxygen and adsorbed CO were both shown to be capable of changing the sign of the Hall coefficient and therefore the dominant carrier type. It was demonstrated that under the conditions of temperature and pressure investigated (e.g., 400 K and 4 torr), polycrystalline RuO_2 films can be unstable and can break up into mixed Ru/RuO_2 phases under CO exposure for tens of hours. The results provide evidence that the angle of incidence during film deposition played a significant role in the formation of nanostructures that were capable of effects such as the resistivity response on first exposure to CO, the hysteresis loops due to gas switching, or the changing of dominant carriers.

8.2. Recommendations for Future Work

Ru and RuO_2 are important industrial catalysts and further studies of charge transport parameters during catalytic reactions may provide fundamental insights into the underlying mechanisms. The following are recommendations that should prove helpful to future studies:

1) More work is needed on the models of resistivity and Hall coefficient in non-slab geometries including nanorod-structured films. A key question is what is the exact expression for the Hall coefficient of a thin film of non-uniform thickness?

2) Further studies are needed to probe the relationship between the Hall coefficient in RuO_2 and the accompanying thin-film structure and stoichiometry. The full mapping of a Hall coefficient phase diagram for a metal oxide that changes dominant carrier type as a function of stoichiometry and structure has yet to be done.

3) Theoretical work on the phase stability of binary oxides that gradually lose oxygen should be carried out using tools such as density functional theory. Predictions of instabilities could be tested experimentally.

4) Further work at higher magnetic fields and lower temperatures is desirable and may determine, for example, whether RuO_2 is truly a compensated metal.

5) Transport measurements taken in real time during surface catalytic reactions of CO and other gases are needed over a wider range of pressures, temperatures, and gas mixtures.

6) Transport measurements in thin-film samples with well defined grain boundaries, such as in RuO_2 bi-crystal samples with specific twist or tilt boundaries, would clarify the importance of grain boundary scattering relative to surface scattering of electrons.

7) Since the angle of incidence played a significant role in the formation of nanostructures capable of the effects described here, additional transport studies of RuO_2 and Ru thin films grown with different angles of incidence would prove useful.

8) Mass spectrometer measurements during redox transport tests would allow a correlation of CO_2 desorption to transport properties.

9) X-ray diffraction of RuO_2 in vacuum or CO atmospheres using a diffractometer “hot stage” would allow direct real-time observations of structural changes associated with oxygen loss.

BIBLIOGRAPHY

N. E. Alekseevskii, K.-H. Bertel, A. V. Dubrovin, V. I. Nizhankovskii and L. Urai, “Magnetoresistance of Ruthenium in Strong Magnetic Fields,” JETP Lett. 18, 5, 163 (1973).

J. K. Alstad, R. V. Colvin and S. Legvold, “Single-Crystal and Polycrystal Resistivity Relationships for Yttrium,” Phys. Rev. 123, 2, 418 (1961).

S. W. Angrist, “Galvanomagnetic and Thermomagnetic Effects,” Scientific American, 205, 6, 124 (1961).

N. W. Ashcroft and N. D. Mermin, *Solid State Physics*, (Brooks/Cole, 1976).

J. Asmussen, R. Fritz, and L. Mahoney, “ECR ion and free radical sources for MBE applications,” Rev. Sci. Instrum. 61, 282 (1990).

J. Asmussen, T. A. Grotjohn, P. Mak, and M. A. Perrin, “The Design and Application of Electron Cyclotron Resonance Discharges,” IEEE Trans. Plas. Sci. 25, 6, 1196 (1997).

J. Assmann, V. Narkhede, N.A. Breuer, M.Muhler, A.P. Seitsonen, M. Knapp, D. Crihan, A. Farkas, G. Mellau and H. Over, “Heterogeneous oxidation catalysis on ruthenium: bridging the pressure and materials gaps and beyond,” J. Phys.: Condens. Matter 20, 184017 (2008).

ASTM F76-86 (Reapproved 1996), Standard Test Methods for Measuring Resistivity and Hall Coefficient and Determining Hall Mobility in Single-Crystal Semiconductors.

J. C. Bailar, H. J. Emeleus, R. Nyholm and A. F. Trotman-Dickenson, *Comprehensive Inorganic Chemistry* (Pergamon, Oxford, 1973).

W. E. Bell and M. Tagami, “High-Temperature Chemistry of the Ruthenium-Oxygen System,” J. Phys. Chem. 67, No. 11, 2432 (1963).

M. B. Bever, ed., *Encyclopedia of Materials Science and Engineering*, (Pergamon, Oxford, 1986).

M. Birkholz, *Thin Film Analysis by X-Ray Scattering* (Wiley-VCH, Weinheim, 2006).

W. Boas and J. K. Mackenzie, *Progress in Metal Physics*, 2 (Interscience, New York, 1950).

B. Brunetti, P. Scardala and V. Piacente, “Dissociation pressure and standard dissociation enthalpy of RuO_2,” Matls. Chem. Phys. 83, 145 (2004).

R. W. Cahn, P. Haasen and E. J. Kramer, eds., *Materials Science and Technology,* (Wiley, New York, 2005).

H. B. Callen, *Thermodynamics* (Wiley, New York, 1960).

J. W. Christian, *The Theory of Transformations in Metals and Alloys* (Pergamon, Oxford, 1965).

K. L. Chopra and S. K. Bahl, "Hall Effect in Thin Metal Films," J. Appl. Phys. 38, 3607 (1967).

E. H. P. Cordfunke, R. J. M. Konings, E. F. Westrum, Jr. and R. Shaviv, "The Thermophysical and Thermochemical Properties of RuO_2 from 0 to 1000 K,“ J. Phys. Chem. Solids 50, 4, 429 (1989).

T. J. Coutts, *Electrical Conduction in Thin Metal Films* (Elsevier, Amsterdam, 1974).

P. A. Cox, *Transition Metal Oxides*, (Clarendon, Oxford, 1992).

A. A. Deckert, J.L. Brand, M.V. Arena and S.M. George, "Surface Diffusion of Carbon Monoxide on Ru(001) Studied Using Laser-Induced Thermal Desorption," Surf. Sci. 208, 441 (1989).

D. Deniz, D. J. Frankel and R. J. Lad, "Nanostructured tungsten and tungsten trioxide films prepared by glancing angle deposition," Thin Solid Films 518, 15, 4095 (2010).

U. Diebold, "The surface science of titanium dioxide," Surface Science Reports 48, 53 (2003).

M. W. Finnis, *Interatomic Forces in Condensed Matter*, (Oxford, 2003).

F. Frohlich, D. Machajdik, V. Cambel, J. Fedor, A. Pisch and J. Lindner, "Growth of Ru and RuO_2 films by metal-organic chemical vapor deposition," J. Phys. IV France 11, 325 (2001).

K. Fuchs, "The conductivity of thin metallic films according to the electron theory of metals," Proc. Camb. Phil. Soc. 34, 100 (1938).

F. Gao, Y. Wang, Y. Cai, D.W. Goodman, "CO oxidation over Ru(0001) at near-atmospheric pressures: From chemisorbed oxygen to RuO_2," Surf. Sci. 603, 1126 (2009).

S. C. Gausepohl, M. Lee, R. A. Rao and C. B. Eom, "Hall-effect sign reversal in $CaRuO_3$ and $SrRuO_3$ thin films," Phys. Rev. B, 54, 8996 (1996).

K. M. Glassford and J. R. Chelikowsky, "Electronic and structural properties of RuO_2," Phys. Rev. B 47, 1732 (1993).

K. M. Glassford and J. R. Chelikowsky, "Electron transport properties in RuO_2 rutile," Phys. Rev. B 49, 7107 (1994).

D.W. Goodman, C.H.F. Peden and M.S. Chen, "CO oxidation on ruthenium: The nature of the active surface," Surf. Sci. Let. 601, L124 (2007).

D.W. Goodman, C.H.F. Peden and M.S. Chen, “Reply to Comment on CO oxidation on ruthenium: The nature of the active catalytic surface” by H. Over, M. Muhler, A.P. Seitsonen,” Surf. Sci. 601, 5663 (2007).

J. E. Graebner, E. S. Greiner and W. D. Ryden, “Magnetothermal oscillations in RuO_2, OsO_2, and IrO_2,” Phys. Rev. B 13, 2426 (1976).

V. G. Grebenkina, D. E. Dyshel, M. D. Smolin and V. N. Fedorov, “Electrical Properties and Mechanism of Electrical Conductivity of Ruthenium Dioxide-Base Thick Films,” Soviet Powder Metallurgy and Metal Ceramics 29, 396 (1990).

I. S. Grigoriev and E. Z. Meilikhov, eds., *Handbook of Physical Quantities* (CRC Press, Boca Raton, 1997).

M. E. Grillo, “Stability of corundum-versus rutile-type structures of ruthenium and rhodium oxides,” Phys. Rev. B 70, 184115 (2004).

Y. Hayakawa, S. Kohiki, M. Arai, H. Yoshikawa, S. Fukushima, K. Wagatsuma, M. Oku and F. Shoji, “Electronic structure and electrical properties of amorphous OsO_2,” Phys. Rev. B 59, 11125 (1999).

V.E. Henrich and P.A. Cox, *The Surface Science of Metal Oxides* (Cambridge, 1994).

M. Hiratani, Y. Matsui, K. Imagawa and S. Kimura, “Hydrogen Reduction Properties of RuO_2 Electrodes,” Jpn. J. Appl. Phys. 38, L1275 (1999).

C. M. Hurd, *The Hall Effect in Metals and Alloys* (Plenum, New York, 1972).

International Centre for Diffraction Data, pdf file 00-006-0663, (2007).

International Centre for Diffraction Data, pdf file 04-003-2008, (2008).

J.-P. Jan, *Solid State Physics,* Vol. 5 (Academic Press, New York, 1957).

Q. X. Jia, Z. Q. Shi, K. L. Jiao, W. A. Anderson and F. M. Collins, “Reactively Sputtered RuO_2 Thin Film Resistor with Near Zero Temperature Coefficient of Resistance,” Thin Solid Films 196, 29 (1991).

K. L. Jiao, Q. X. Jia and W. A. Anderson, “Stability of RuO_2 thin film resistors,” Thin Solid Films 227, 59 (1993).

E. V. Jelenkovic, K. Y. Tong, W. Y. Cheung and S. P. Wong, “RuO_2-SiO_2 composite thin films with wide resistivity range,” Microelectronic Engineering 71, 237 (2004).

E. Justi, “Elektrische Eigenschaften von Ruthenium,” Zeitschrift fur Natufurschung 4a, 472 (1949).

T. Karabacak, G.-C. Wang and T.-M. Lu, “Quasi-periodic nanostructures grown by oblique angle deposition,” J. Appl. Phys. 94, 12, 7723 (2003).

S. Kim, N. Koratkar, T. Karabacak and T.-M. Lu, "Water electrolysis activated by Ru nanorod array electrodes," Appl. Phys. Lett. 88, 263106 (2006).

Y. T. Kim, "Achievement of zero temperature coefficient of resistance with RuO_x thin film resistors," Appl. Phys. Lett. 70 (2), 209 (1997).

C. Kittel, *Introduction to Solid State Physics* (Wiley, 2005).

P. Kofstad, *Nonstoichiometry, Diffusion, and Electrical Conductivity in Binary Metal Oxides* (Wiley, New York, 1972).

E. Kreyszig, *Advanced Engineering Mathematics* (Wiley, New York, 1967).

L. Krusin-Elbaum, "Effect of Oxygen on the Electrical Transport in RuO_2," Thin Solid Films 169, 17 (1989).

J. M. Leger, P. Djemia, F. Ganot, J. Haines, A. S. Pereira and J. A. H. da Jornada, "Hardness and elasticity in cubic ruthenium dioxide," Appl. Phys. Lett. 79, 2169 (2001).

J. J. Lin, S. M. Huang, Y. H. Lin, T. C. Lee, H. Liu, X. X. Zhang, R. S. Chen and Y. S. Huang, "Low temperature electrical transport properties of RuO_2 and IrO_2 single crystals," J. Phys.: Condens. Matter 16, 8035 (2004).

H. Madhavaram, H. Idriss, S. Wendt, Y.D. Kim, M. Knapp, H. Over, J. Assmann, E. Loffler and M. Muhler, "Oxidation Reactions over RuO_2: A Comparative Study of the Reactivity of the (110) Single Crystal and Polycrystalline Surfaces," J. Catalysis 202, 296 (2001).

A. P. Mackenzie, N. E. Hussey, A. J. Diver, S. R. Julian, Y. Maeno, S. Nishizaki and T. Fujita, "Hall effect in the two-dimensional metal Sr_2RuO_4," Phys. Rev. B 54, 7425 (1996).

D. Mandrus, V. Keppens, B. C. Sales and J. L. Sarrao, "Unusual transport and large diamagnetism in the intermetallic semiconductor $RuAl_2$," Phys. Rev. B 58, 3712 (1998).

J. I. Martinez, H. A. Hansen, J. Rossmeisl and J. K. Norskov, "Formation energies of rutile metal dioxides using density functional theory," Phys. Rev. B 79, 045120 (2009).

Y. Matsui, M. Hiratani, T. Nabatame, Y. Shimamoto and S. Kimura, "Characteristics of Ruthenium Films Prepared by Chemical Vapor Deposition Using Bis(ethylcyclopentadienyl) Ruthenium Precursor," Electrochem. Solid-State Lett. 5 (1), C18 (2002).

L. F. Mattheiss, "Electronic structure of RuO_2, OsO_2, and IrO_2," Phys. Rev. B 13, 2433 (1976).

A.F. Mayadas and M. Shatzkes, "Electrical-Resistivity Model for Polycrystalline Films: the Case of Arbitrary Reflection at External Surfaces," Phys. Rev. B 1, 1383 (1970).

G. T. Meaden, *Electrical Resistance of Metals* (Plenum, New York, 1965).

H. Mehrer, *Diffusion in Solids* (Springer, Berlin, 2007).

S. C. Moulzolf, “Synthesis and Characterization of ZrO_2 Thin Films with Controlled Microstructure,” PhD Thesis, The University of Maine (1999).

S. C. Moulzolf, D. J. Frankel and R. J. Lad, “In situ four-point conductivity and Hall effect apparatus for vacuum and controlled atmosphere measurements of thin film materials,” Rev. Sci. Instrum. 73, 6 (2002).

K. Murai, Y. Akune, Y. Suzuki, T. Moriga and I. Nakabayashi, “Thermal Vibration Analysis of RuO_2 by EXAFS,” Int. J. Mod. Phys. B, 20, Nos. 25, 26 &27, 4111 (2006).

J. L. Nichols, “Orientation and Temperature Effects on the Electrical Resistivity of High-Purity Magnesium, J. Appl. Phys. 26, 470 (1955).

M. Ohring, *Materials Science of Thin Films* (Academic, San Diego, 2002).

M. A. Omar, *Elementary Solid State Physics* (Addison-Wesley, Reading, 1993).

L. Onsager, “Reciprocal Relations in Irreversible Processes,” Phys. Rev. 37, 405 (1931).

H. Over, Y.D. Kim, A.P. Seitsonen, S. Wendt, E. Lundgren, M. Schmid, P. Varga, A. Morgante and G. Ertl, “Atomic-Scale Structure and Catalytic Reactivity of the $RuO_2(110)$ Surface,” Science 287, 1474 (2000).

H. Over, M. Muhler and A.P. Seitsonen, “Comment on “CO oxidation on ruthenium: The nature of the active catalytic surface” by D.W. Goodman, C.H.F. Peden, M.S. Chen,” Surf. Sci. 601, 5659 (2007).

C.H.F. Peden and D.W. Goodman, “Kinetics of CO Oxidation over Ru(0001),” J. Phys. Chem. 90, 1360 (1986).

D. G. Pettifor, *Bonding and Structure of Molecules and Solids* (Clarendon, Oxford, 2002).

R. W. Powell, R. P. Tye and M. J. Woodman, “The Thermal Conductivity and Electrical Resistivity of Polycrystalline Metals of the Platinum Group and of Single Crystals of Ruthenium,” J. Less-Common Metals 12, 1 (1967).

C. N. R. Rao and B. Raveau, *Transition Metal Oxides* (VCH, New York, 1995).

K. Reuter and M. Scheffler, “Composition, structure, and stability of $RuO_2(110)$ as a function of oxygen pressure,” Phys. Rev. B 65, 035406 (2001).

G. Rickers and G. Sorensen, “Diffusion of Inert Gases in Copper,” Physica Status Solidi, 32, 597 (1969).

M. Rossler, S. Gunther and J. Wintterlin, “Scanning Tunneling Microscopy of the $RuO_2(110)$ Surface at Ambient Oxygen Pressure,” J. Phys. Chem. C, 111, 2242 (2007).

S.M. Rossnagel and T.S. Kuan, “Alteration of Cu conductivity in the size effect regime,” J. Vac. Sci. Technol. B 22(1), 240 (2004).

W. D. Ryden, A. W. Lawson and C. C. Sartain, “Electrical Transport Properties of IrO_2 and RuO_2,” Phys. Rev. B 1, 1494 (1970).

A.P. Seitsonen and H. Over, “Intimate interplay of theory and experiments in model catalysis,” Surf. Sci. 603, 1717 (2009).

Z. Sljivancanin and B. Hammer, “CO oxidation on fully oxygen covered Ru(0001): Role of step edges,” Phys. Rev. B 81, 121413(R) (2010).

E.H. Sondheimer, “The Mean Free Path of Electrons in Metals,” Adv. Phys. 1, 1 (1952).

G.A. Somorjai, *Introduction to Surface Chemistry and Catalysis* (Wiley, New York, 1994).

M.M. Steeves, “Calibration of a Four-Point Resistivity and Hall-Effect Apparatus for Vacuum and Controlled Atmosphere Measurements,” PHY 510 Graduate Laboratory Report, Dept. of Physics and Astronomy, The University of Maine (2007).

M. M. Steeves, D. Deniz and R. J. Lad, “Charge transport in flat and nanorod structured ruthenium thin films,” Appl. Phys. Let. 96, 142103 (2010).

M. M. Steeves and R. J. Lad, “Influence of nanostructure on charge transport in RuO_2 thin films,” J. Vac. Sci. Technol. A, 28, 4, 906 (2010).

T. Sun, B. Yao, A.P. Warren, K. Barmak, M.F. Toney, R.E. Peale and K.R. Coffey, “Surface and grain-boundary scattering in nanometric Cu films,” Phys. Rev. B 81,155454 (2010).

R. A. Swalin, *Thermodynamics of Solids* (Wiley, New York, 1972).

R. J. Tainsh and G. K. White, “Resistivity of Ruthenium,” Can. J. Phys. 42, 208 (1964).

F. Tang, T. Karabacak, L. Li, M. Pelliccione, G.-C. Wang and T.-M. Lu, “Power-law scaling during shadowing growth of nanocolumns by oblique angle deposition,” J. Vac. Sci. Technol. A 25, 1, 160 (2007).

K. Y. Tong, V. Jelenkovic, W. Y. Cheung and S. P. Wong, “Temperature dependence of resistance in reactively sputtered RuO_2 thin films,” J. Mat. Sci. Let. 20, 699 (2001).

V. Vand, “A theory of the irreversible electrical resistance changes of metallic films evaporated in vacuum,” Proc. Phys. Soc. 55, 222 (1943).

L. J. van der Pauw, “A method of measuring specific resistivity and Hall effect of discs of arbitrary shape,” Philips Res. Repts. 13, 1 (1958).

R. P. Vasil'yeva, A. V. Cheremushkina and N. N. Ivanova, "Hall and Nernst-Ettingshausen Effects in Rhodium and Ruthenium," Fiz. Metal. Metalloved. 35, 4, 872 (1973).

J. Volger, "Note on the Hall Potential Across an Inhomogeneous Conductor," Phys. Rev. 79, 1023 (1950).

N. V. Volkenshteyn, V. A. Novoselov, V. Y. Startsev and Y. P. Romanov, "Anisotropy of the Resistivity and Hall Coefficient of Ruthenium in the Low-Temperature Range," Fiz. Metal. Metalloved. 33, 6, 1233 (1972).

M. Watanabe and A. Hiratuka, "Optical Reflectance and Electrical Resistance of Gas Adsorbed Thin Metallic Films," Jap. J. Appl. Phys. 18, 31 (1979).

J. H. Xu, J. Jarlborg and A. J. Freeman, "Self-consistent band structure of the rutile dioxides NbO_2, RuO_2, and IrO_2," Phys. Rev. B 40, 7939 (1989).

Appendix A

DEPOSITION PARAMETERS FOR RUO_2 FILMS OF CHAPTER 5

Films for Chapter 5 were grown by confocal reactive magnetron sputtering on GE Type 124 fused quartz substrates at a rotation rate of 14 rpm unless otherwise stated. The center-to-center distance from the target to the substrate was 17 cm. Substrates for films 1 - 9 were given additional cleaning by acetone, methanol, isopropanol, and deionized water followed by N_2 blow drying. All others were used as received. All substrates were argon plasma cleaned at 100° C and 3 mtorr for 1 minute prior to deposition. System base pressures were approximately 1 microtorr. During sputtering, flow rates were 13 and 10 sccm of oxygen and argon respectively. Film thicknesses were measured by x-ray reflectivity and profilometry. Table A.1 lists parameters that were varied in the study.

TABLE A.1. Parameters of planar RuO_2 thin films considered in Chapter 5.

No	Sample	Film Growth				Anneal		Comment
		Pressure (torr)	Sub T (°C)	Time (min)	Power (W)	T/Time/Atm (C/min/gas)	Thks (Å)	
1	080821-RuO2-1	3.5×10^{-3}	100	7	500	500/30/vac	1405	anl dep chbr
2	080821-RuO2-2	3.5×10^{-3}	100	7	500	None	1413	
3	080825-RuO2	3.5×10^{-3}	100	7	500	None	1428	
4	080826-RuO2-1	3.5×10^{-3}	100	7	500	206/120/air	1356	air anl
5	080826-RuO2-2	3.5×10^{-3}	100	7	500	166/60/air	1414	anl after tsp tsts
6	080826-RuO2-3	3.5×10^{-3}	100	7	500	None	1492	
7	080826-RuO2-4	3.5×10^{-3}	100	7	500	350/30/air	1412	air anl
8	080923-RuO2	3.5×10^{-3}	100	56	186	None	779	
9	080930-RuO2	3.5×10^{-3}	100	56	186	350/30/vac	779	vac anl
10	081009-RuO2	3.5×10^{-3}	100	7	500	350/30/vac	1406	vac anl
11	081016-RuO2	3.5×10^{-3}	100	100	186	None	1390	profilometer
12	081022-RuO2-1	3.5×10^{-3}	300	7	500	None	1503	300-350°C sub
13	081022-RuO2-2	3.5×10^{-3}	300	7	500	None	1452	300-350°C sub
14	081027-RuO2	3.5×10^{-3}	16	7	500	None	1360	

TABLE A.1. (Continued)

No	Sample	Film Growth				Anneal		Comment
		Pressure	Sub T	Time	Power	T/Time/Atm	Thks	
		(torr)	(°C)	(min)	(W)	(C/min/gas)	(Å)	
15	081106-RuO2-1	3.5 x 10^{-3}	100	7	500	None	1260	24W RF bias
16	081106-RuO2-2	3.5 x 10^{-3}	100	7	500	None	1850	38.8° tilt
17	081111-RuO2-1	3.5 x 10^{-3}	100	7	500	None	1412	no rotation
18	081111-RuO2-2	3.5 x 10^{-3}	100	7	500	None	1519	no rot, bias
19	081118-RuO2-1	3.5 x 10^{-3}	100	7	500	None	1430	7 rpm
20	081118-RuO2-2	3.5 x 10^{-3}	100	7	500	None	1340	10 rpm
21	081125-RuO2-1	3.5 x 10^{-3}	100	7	500	None	1405	17 rpm
22	081125-RuO2-2	3.5 x 10^{-3}	100	7	500	None	1304	lower t-to-s d
23	081210-RuO2-1	4.1 x 10^{-3}	100	30	100	None	290	100W/100°C
24	081210-RuO2-2	3.5 x 10^{-3}	100	20	300	None	1350	300W/100°C
25	081217-RuO2-1	3.0 x 10^{-3}	100	15	400	None	2050	pwr PS; scratch
26	081217-RuO2-2	3.0 x 10^{-3}	100	15	400	None	2034	400W/100°C
27	081217-RuO2-3	2.8 x 10^{-3}	500	7	500	None	1285	500W/500°C
28	081218-RuO2-1	2.7 x 10^{-3}	400	7	500	None	1314	500W/400°C
29	081218-RuO2-2	2.7 x 10^{-3}	200	7	500	None	1320	500W/200°C
30	081229-RuO2-1	2.7 x 10^{-3}	300	7	500	None	1336	500W/300C/28°
31	081229-RuO2-2	2.7 x 10^{-3}	200	7	400	None	874	400W/200°C
32	081229-RuO2-3	3.0 x 10^{-3}	300	15	400	None	2068	400W/300°C
33	081230-RuO2-1	3.1 x 10^{-3}	400	15	400	None	1900	400W/400°C
34	081230-RuO2-2	3.5 x 10^{-3}	500	15	400	None	2068	400W/500°C
35	081230-RuO2-3	2.6 x 10^{-3}	100	4	532	None	750	max power
36	090102-RuO2-1	3.6 x 10^{-3}	200	20	300	None	1350	300W/200°C
37	090102-RuO2-2	3.6 x 10^{-3}	300	20	300	None	1350	300W/300°C
38	090102-RuO2-3	3.5 x 10^{-3}	400	20	300	None	1350	300W/400°C
39	090114-RuO2-1	3.6 x 10^{-3}	500	20	300	None	1350	300W/500°C
40	090114-RuO2-2	3.5 x 10^{-3}	200	30	200	None	446	200W/200C/P=?
41	090120-RuO2-1	4.0 x 10^{-3}	300	30	200	None	605	200W/300°C
42	090120-RuO2-2	4.0 x 10^{-3}	400	30	200	None	446	200W/400°C
43	090120-RuO2-3	4.0 x 10^{-3}	500	30	200	None	446	200W/500°C
44	090122-RuO2-1	4.1 x 10^{-3}	200	30	100	None	265	100W/200°C
45	090122-RuO2-2	4.1 x 10^{-3}	300	30	100	None	197	100W/300°C
46	090604-RuO2	4.0 x 10^{-3}	500	120	200	None	1784	200W/500°C
47	090910-RuO2-1	2.6 x 10^{-3}	16	7	500	None	1360	500W/16°C
48	090910-RuO2-2	2.6 x 10^{-3}	16	7	500	None	1360	500W/16°C

Appendix B

CALIBRATION OF RESISTIVITY AND HALL COEFFICIENT

System calibration, with an emphasis on the Hall coefficient as the more problematic measurement, was checked at room temperature using primarily an unannealed gold thin film designated 070126-Au1100, which was approximately 1100 Å thick. At 23 °C, the film consistently returned a resistivity near 4.5 μΩ cm and a Hall coefficient near -7.5 x 10^{-5} cm^3/C. These values can be compared to an average bulk resistivity of gold equal to 2.20 μΩ cm (residual resistivity subtracted) and a Hall coefficient of -7.15 x 10^{-5} cm^3/C averaged from bulk samples and thin films.[1, 2] A one-time check of the system was made using a certified commercial silicon standard from MMR Technologies. At 32 °C, the specified resistivity of the standard was 5.892 Ω cm and the Hall coefficient was +1803 cm^3/C. At 21 °C, the system returned a resistivity of 5.73 Ω cm and a Hall coefficient of +1782 cm^3/C. Calibration in vacuum at temperatures above room temperature was attempted using samples made from commercial silicon wafers. Based on a p-type wafer, resistivity measurements were accurate to within about ± 12 % at room temperature and within ± 6 % at temperatures up to 400 K. The Hall coefficient was within a factor of 2 of the value estimated for the p-type wafer in the range from room temperature to 400 K. An n-type wafer displayed a parabolic dependence of Hall coefficient with temperature, but in the range from room temperature to 450 K was within roughly 30 % of the estimate.

---

[1] G. T. Meaden, *Electrical Resistance of Metals* (Plenum, New York, 1965).

[2] C. M. Hurd, *The Hall Effect in Metals and Alloys* (Plenum, New York, 1972).

BIOGRAPHY OF THE AUTHOR

Michael M. Steeves was born on September 21, 1949, in Lebanon, New Hampshire. By the time he had graduated from high school in Oswego, New York, in 1967, he had lived in six states including several locations in Maine due to his father's employment in the construction industry. After obtaining degrees from the University of Maine and MIT he worked primarily in the area of magnetics on generators, electromagnets, and superconductors. He spent most of his employment working at the MIT Plasma Fusion Center on type-2 superconductor development, with the largest prototype conductor being rated at a capacity of 46,000 A at 4.2 K in a 12 T magnetic field. He has been privileged to work or collaborate with colleagues in many fine laboratories including the Francis Bitter National Magnet Laboratory, the Princeton Plasma Physics Laboratory, the Lawrence Livermore National Laboratory, the Kernforschungszentrum Karlsruhe, and the Japan Atomic Energy Research Institute (JAERI) at Tokai, Naka as well as smaller labs at MIT and General Electric. His work with JAERI received recognition from the US Department of Energy. One of his main technical interests, as reflected by this thesis, is in the area of electrical conduction. The discovery of high-critical-temperature superconductors in 1987 contributed to his curiosity about transition-metal oxides and their tremendous range of electrical properties. He is a candidate for the Doctor of Philosophy degree in Physics from the University of Maine in May, 2011.